Master thesis

Study on time-varying hydrodynamic coefficients for large-scale bottom-founded wind turbines and their impact on fatigue

Author: Thomas van Deursen

Student number:	TU Delft	5652189
Student number:	NTNU	103226

Thesis committee:

As. Prof. Dr. O.J. Colomés Gené	Chairman & TU Delft supervisor
Prof. Dr. M. Greco	Committee & NTNU supervisor
Ir. J.S. Hoving	TU Delft committee
Prof. Dr. Erin Bachyski-Polić	NTNU committee
Joseph Hilton	SLPE supervisor
Jaap Derks	Smulders supervisor

To obtain the degrees

Master of Science
in Offshore Engineering
at the Delft University of Technology

Master of Science
in Technology- Wind Energy
at the Norwegian University of Science and Technology

to be defended publicly on Tuesday 9th of July, 2024.

Preface

This thesis is written as part of the European Wind Energy Master program and serves as the final deliverable to obtain a degree in Offshore Engineering from Delft University of Technology (TU Delft) and a degree in Wind Energy Technology from the Norwegian University of Science and Technology (NTNU). The objective of this master thesis was to investigate a time-varying hydrodynamic coefficient method for large-scale bottom-founded wind turbines and its impact on fatigue. This research was proposed by and conducted in cooperation with Sea and Land Project Engineering (SLPE, n.d.).

Prior to this thesis, a project thesis was undertaken at the Institute for Marine Technology, NTNU. This preliminary work laid the groundwork for the present thesis, emphasizing a thorough literature review and initial analyses. Throughout this thesis, numerous references have been made to the aforementioned project thesis, denoted as Deursen (2023). It should be noted that this project thesis is not published.

I would like to thank all my supervisors for their guidance, help, and support throughout the entire project. Marilena Greco from NTNU, thank you for being highly critical of my work to maintain its quality while giving me the freedom to pursue my preferred direction. Joseph Hilton from SLPE, thank you for your countless valuable insights from an industry perspective and for making time to support me. Oriol Colomés Gené from TU Delft, thank you for your support throughout the thesis and for listening to my weekly updates. You allowed me to pursue my preferred direction while ensuring a logical sequence. Jaap Derks from Smulders, thank you for your practical guidance and for facilitating all necessities. Erin Bachyski-Polić from NTNU, thank you for helping me acquire, process, and understand the experimental data used in this thesis.

Thomas van Deursen
Wijchen, July 2024

Executive Summary

The exploration of bottom-founded offshore wind turbine development, focusing on monopiles, indicates that while the floating offshore wind sector is emerging to exploit deeper sites, there is a continued rationale for advancing XXL monopiles in the realm of bottom-founded offshore wind. Cost-effectiveness stands out as a pivotal factor among several compelling arguments.

In this thesis, an effort is made to advance XXL monopiles by calculating the wave loads more accurately with the aim of increasing the range for which these are economically viable. A specific emphasis was placed on trying to develop a more accurate wave-loading methodology for these XXL monopiles by the introduction of time-varying hydrodynamic coefficients. The exact objective was to determine whether the establishment of time-varying coefficients within the first and second-order irregular wave theory increased the accuracy of the wave loads and investigate the influence of this newly established calculation technique on the fatigue life of an XXL monopile.

A comprehensive literature review on theoretical models for wave theories and wave loading was conducted and summarized, providing foundational knowledge for this investigation. Building on the literature review, a time-varying coefficient method was proposed. Despite previous attempts, critical differences in methodology emphasize the legitimacy of this method. Fundamental to this newly proposed method was the accounting for the subperiodic fluctuations in wave force coefficients by introducing both a Keulegan-Carpenter and Reynolds dependency, established by the use of zero-crossing periods.

The newly developed method was created in a MATLAB environment and is available for implementation using both first and second-order wave theory, as well as the Morison and Rainey load models.

In order to say anything about the accuracy of the newly developed method, an attempt to replicate the results from the experiment by M. Thys, F. H. Dadmarzi, and E. Bachynski for the project WAS-XL was made. Both regular and irregular waves were reproduced. Especially the least steep regular waves were accurately reproduced by the model. For the steeper waves, second-order wave theory was insufficient in terms of capturing all characteristics which led to a less accurate reproduction.

Reproducing the irregular waves from the experiments brought some difficulties since the report of the experiment did not include enough detail about the random phases and wave components. By bypassing this issue via a Fast Fourier Transform (FFT) of the surface elevation the model was able to reproduce the surface elevation of the experiment. This was however limited to first-order wave theory due to the linearization of the free surface elevation which is induced by the FFT. In this context, linearization means that decomposing the surface elevation using FFT masks the nonlinear interaction effects present in the surface elevation. Even though the first-order wave theory model was able to reproduce the surface elevation accurately, both the forces and moments were not reproduced accurately. Spectral analysis showed that nonlinearities in the forces and moments were present which were not present in the surface elevation. Further analysis of these nonlinearities was halted due to time and objective limitations. A sensitivity study was set out for the structural response calculation to see the influence of nonlinearities in the forces on the fatigue assessment.

A comprehensive literature review on fatigue assessment by recommended practice was conducted and summarized, providing foundational knowledge for the simplified fatigue assessment to evaluate various coefficient methods.

The simplified fatigue assessment which predominantly reduced the number of load cases was prepared and executed with the use of MonoPoly, an in-house software package developed by Sea and Land Project Engineering (SLPE). For site characterization and structural configuration the North Sea Wind Farm, a reference project by SLPE, was used (SLPE, n.d.).

The assessment was done for different test cases whose aim was to scrutinize the impact of different analysis approaches in the time-varying coefficient method model. Overall the results showed that the time-varying coefficient method decreases the maximum Damage Equivalent Moment (DEM)

values by 0.2 to 0.7 percent depending on the analysis approach adopted. The mean DEM values decrease by a range of 0.2 to 0.5 percent. It is however noted that these results apply to a more advanced constant coefficient method used by industry relative to the one recommended by ISO. A side study showed that the decrease in DEM values would be even bigger for a comparison between this newly established method and the one recommended by ISO.

For thin-walled cylinders like monopiles, the relationship between the moment and thickness is essentially linear. Therefore, with a 0.5 percent reduction in mean DEM, the thickness of the monopile can be reduced by 0.5 percent to maintain stress levels. This reduction in material thickness has the potential to save several million euros for wind farms.

Since the trend of the results was that the newly established method reduces the DEM, checking its accuracy in greater detail is the primary task for future work. If its accuracy can be validated to a better extent for irregular waves it could possibly increase the cost-effectiveness of monopiles. Leading to an increase in the range for which bottom-founded Offshore Wind Turbines are economically viable.

Since this methodology can be easily implemented for both deep-water and shallow-water sites, it would be interesting for future work to examine the influence of water depth on this newly established method. For the structural response initiated by wave loading, one of the important factors is the natural frequency of the monopile. This is greatly affected by water depth, not only because of the potentially taller or shorter monopile but also because of the nonlinear wave kinematics that occur specifically at intermediate and shallow water depths.

Table of Contents

List of Figures

List of Tables

Nomenclature

η Instantaneous wave elevation

λ Wave length

ν Kinematic viscosity of water

ω Wave frequency

ρ Material density

σ Standard deviation

$\boldsymbol{\Phi}$ Velocity potential

A Area

API American Petroleum Institute

C_d Hydrodynamic drag coefficient

C_m Hydrodynamic inertia coefficient

C_{ds} Hydrodynamic drag coefficient for steady flow

$CAPEX$ Capital Expenditure

CMS Component Mode Synthesis

D Diameter of a cylindrical element

d Water depth

DEM Damage Equivalent Moment

DNV Det Norske Veritas

e Relative surface roughness

FEA Finite Element Analysis

FFT Fast Fourier Transform

FLS Fatigue Limit State

FNV Faltinsen Newman Vinje

$FOWT$ Floating Offshore Wind Turbine

g Gravitational acceleration

H Wave height

H_s Significant wave height

IEA International Energy Agency

IEC International Electrotechnical Commission

$IIRS$ Iterated Improved Reduction System

ISO International Organization for Standardization

k Wave number

K_c Keulegan Carpenter number

L	Wave length
MWL	Mean Water Level
NSS	Normal Sea State
$NTNU$	Norwegian University of Science and Technology
NZE	Net Zero Emissions
OWT	Offshore Wind Turbine
PSD	Power Spectrum Density
R	Radius of cylindrical element
r	Current / wave velocity ratio
R_e	Reynolds number
$S(\omega)$	Wave spectrum
s	s-coordinate
SCF	Stress Concentration Factor
SDF	Spectral Density Function
$SLPE$	Sea and Land Project Engineering
SWL	Still Water Level
T	Wave period
T_p	Peak period
TP	Transition Piece
U_c	Current speed
U_m	Maximum speed (including current) normal to cylinder axis in wave cycle
U_{mo}	Maximum wave-induced orbital velocity
ULS	Ultimate Limit State
WP	Wave Probe
WTG	Wind Turbine Generator
x	x-coordinate
y	y-coordinate
z	z-coordinate

1   Introduction

In 2021, the International Energy Agency (IEA) published its report, 'Net Zero by 2050: A Roadmap for the Global Energy Sector,' which includes a detailed pathway named the Net Zero Emissions by 2050 (NZE) scenario. This scenario describes how energy demand and the energy mix will need to evolve if the world is to achieve net-zero emissions by 2050. Besides this, it also assessed the corresponding investment needs and explored key uncertainties surrounding technology and consumer behavior.

The NZE scenario identified renewables as the key technology to reduce emissions from electricity supply at a global level. It describes that the share of renewables in total electricity generation globally will increase from 29% in 2020 to over 60% in 2030 and to nearly 90% in 2050. To achieve this, annual capacity additions of offshore wind between 2020 and 2050 should be almost five times higher than the average over the previous three years (International Energy Agency, 2021).

Recent developments such as the Hywind Tampen project confirm the NZE scenario about the increasing contribution of floating offshore wind. Floating wind solely helps to unlock the enormous potential that exists around the world according to the IEA (International Energy Agency, 2021). What is being referred to here is the decreasing financial viability of bottom-founded offshore wind for larger water depths. However, even though floating offshore wind technology is slowly but surely emerging, as evidenced by current projects, it is worth exploring the limitations of bottom-founded offshore wind.

Exploring limits in this case includes the introduction of XXL monopiles. XXL monopiles are defined in this thesis as monopiles with Diameter, $D > 10$ [m]. This foundation type is much bigger than traditional monopiles and therefore enables bottom-founded wind projects to move to deeper waters. However, the characteristics such as responses to irregular waves change compared to traditional monopiles. It is of utmost importance to validate and critically assess the currently used analysis and its applicability to XXL monopiles. This all links back to the cost reduction compared to floating wind. As of now, bottom-founded is cheaper but many predict that there will be a point in time when floating wind will overtake bottom-founded structures for intermediate water depths in terms of costs. Intermediate water depth here should be interpreted as water depths ranging roughly from 50 [m] to 70 [m].

One of the methods to increase the range for which the bottom-founded offshore wind turbines are economically viable is to analyze the structures more accurately. By doing this, material usage can be reduced and therefore costs can be compressed. In this thesis, increasing accuracy in terms of the hydrodynamic analysis is considered.

1.1   Development of bottom-founded Offshore Wind Turbines

The inception of bottom-founded Offshore Wind Turbines (OWT) can be traced back to the groundbreaking achievements of the Vindeby offshore wind farm. The historic Vindeby wind farm, established in 1991 off the coast of Denmark, marked a pivotal milestone as the world's first offshore wind farm (Orsted, 2019). Comprising 11 turbines, Vindeby showcased the potential of harnessing wind energy in marine environments, paving the way for further developments. Shortly after, the innovation of monopile-supported offshore wind turbines emerged. This pioneering design set the foundation for a new era of offshore wind energy, demonstrating the feasibility and scalability of bottom-founded structures. These early achievements laid the groundwork for the continued evolution and rapid expansion of offshore wind energy worldwide.

A hot topic nowadays is Floating Offshore Wind Turbines (FOWT). This innovative technology is gaining more and more investment and public policy support due to its ability to tap into the substantial 80% of offshore generation potential found in water depths exceeding 60 [m], according to the IEA. In Figure 1, a visual indication is given of this potential specifically for the North Sea. These deeper waters are usually located further offshore, where the wind tends to be more consistent. Traditional bottom-founded offshore wind support structures face technical, logistical, and economic challenges in such locations. In recent years, there has been rapid development

in floating offshore wind technologies, with numerous concepts emerging. With the successful deployment of prototypes and demonstration projects, the industry is now swiftly transitioning to commercial ventures.
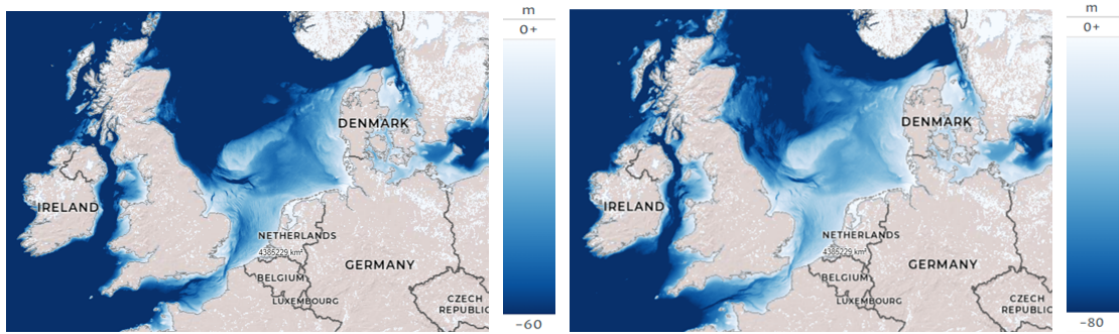
Figure 1: Comparison availability offshore wind area with different water depths, created using Global Wind Atlas

Nonetheless, this transition should not be interpreted as a complete cessation of the development of bottom-founded OWTs. In fact, one could assert that continuing the development of bottom-founded OWTs is equally crucial as the advancement of FOWTs. This viewpoint is supported by several compelling arguments, with the most significant ones presented below.

The first of which is cost-effectiveness. The persistent prediction of the decline of monopiles as the primary foundation type for offshore wind farms has arisen repeatedly, particularly as offshore sites ventured into deeper waters. Initially, there were anticipations that jackets would supplant monopiles, and now there is increasing support for floating foundations as their successors. Nonetheless, in the present day, monopiles continue to dominate as the predominant and cost-effective choice for offshore wind foundations. In 2023, approximately 80% of offshore wind turbine foundations rely on monopiles. Their durability and adaptability, bolstered by innovative design enhancements, have upheld their competitive advantage, even as water depths continue to increase (Empire Engineering, 2023).

Notably, wind turbines are currently being erected on monopile foundations in locations with water depths that, not long ago, would have been designated for jackets. Until recently, for example, the prerequisites for monopiles included a seabed that was both soft enough for pile-driving and firm enough to ensure stability. However, this criterion is now being circumvented, with the inaugural deployment of drilled and grouted monopiles, which is done in the offshore wind industry off the coast of France currently.

Furthermore, Wind Europe, an organization representing the wind energy value chain, underscores that bottom-founded wind remains one of the most economical sources of electricity, thanks to its rapid cost reduction trend over the past decade (Wind Europe, 2021). The assertion that floating wind can emulate this trajectory, however, is underpinned by the fact that floating wind is presently more costly. Thus, while many predict that floating wind will eventually outperform bottom-founded wind, there is no compelling reason to halt the advancement of bottom-founded wind until this tipping point is achieved.

The second aspect to consider is the decommissioning process. Many existing bottom-founded wind farms are nearing the end of their originally intended design lifespans. As the Capital Expenditure (CAPEX) for these assets should have been fully amortized, there is a natural inclination to maximize their operational life and extract every possible unit of energy. However, even after considering strategies for repowering or extending their lifespan, a point of decommissioning will eventually arrive when the wind farm must be replaced with something new. Assuming that the replacement also involves a wind farm, a new challenge emerges, namely, the growing size of wind turbines aimed at enhancing capacity and power efficiency.

In 2021, the largest turbine slated for installation was the 14 [MW] Siemens Gamesa model, featuring a massive 222 [m] rotor diameter and 108 [m] long blades. Just two years later, in

January 2023, the world witnessed the inauguration of the most powerful wind turbine to date, the Vestas V236-15.0 [MW], sporting a colossal 236 [m] rotor diameter, and CSSC Haizhuang Wind Power in China unveiled the nacelle of the H260-18 [MW] offshore wind turbine prototype, boasting a staggering 260 [m] rotor diameter. It is highly probable that we will soon witness even larger 20 [MW] and 24 [MW] turbines. These ever-increasing turbine sizes necessitate innovative foundation design updates to accommodate the added weight and height. This could lead to the necessity of XXL monopiles in terms of the diameter even if the water is considered shallow, as it is for most existing wind farms that are nearing their end of life.

And a little further fetched but still relevant is the intermittency problem that comes with sustainable energy, in particular wind energy. It describes the concept of harvesting all available energy, which is variable for wind energy since windy conditions are not constant. Additionally, it could be windy in one place but calm in another place. And therefore you create the problem of generating energy independent of where it is needed. This results in the well-known problem of energy transport and storage. By developing both bottom-founded and floating OWTs you naturally cover more diverse areas and reduce the intermittency problem. Another possibility is to combine it in the form of hybrid sites (Noonan, 2021).

Lastly is the scarcity of available data for floating wind technology. As floating turbines are still in the early prototype phase of development, there is a dearth of data for verifying computer models (Stewart and Muskulus, 2016). This lack of validation introduces heightened uncertainty and risk for future installations, a challenge that bottom-founded wind technology faces to a lesser extent. So this once again accentuates the importance of the development of bottom-founded OWTs, at least until floating wind technology attains a more mature stage of development.

The development of OWTs encompasses various intricate aspects. Notable areas of significance include addressing environmental impacts such as noise, enhancing efficiency, and shaping regulatory and policy frameworks. This thesis, however, concentrates on advancing bottom-founded OWTs in response to the hydrodynamic challenges associated with greater water depths. This is a strategic effort aimed at increasing the range for which the bottom-founded OWTs are economically viable. The exclusion of further advantages for offshore support structure designs is intentional, prioritizing the delivery of a clear and focused message. The hydrodynamic challenges are further elaborated in Section 1.2.

1.2 Hydrodynamic challenges

The need for larger substructures is mainly driven by both greater water depths and the increasing size of turbines. A substructure is the part of an OWT which connects the turbine with the seabed. This thesis delves into the examination of substructures, with a particular focus on those falling within the monopile category. Larger substructures therefore entail large-diameter monopiles, also referred to as XXL monopiles or more generally large-diameter water-piercing cylindrical structures.

Large-diameter monopile support structures for OWTs typically exhibit their lowest resonance period in the range of 3 to 5 [s]. These periods can align with the second, third, and fourth-order excitation frequencies of ocean waves during stormy conditions (Bachynski et al., 2017). As a result, the nonlinear, high-frequency wave loads can induce springing- and ringing-type responses in the structure which have also been observed in recent model tests of bottom-founded OWTs (Bachynski et al., 2017, De Ridder et al., 2011, Suja-Thauvin, Krokstad and Frimann-Dahl, 2016, Bredmose et al., 2013). Here, we apply Faltinsen's definition of ringing: "transient structural deflections at frequencies substantially higher than the incident wave frequencies" (Faltinsen et al., 1995). Ringing is typically described as a transient event, possibly but not necessarily occurring in the aftermath of a high, steep wave, whereas "springing" is recognized as a steady-state resonance, for example, but not necessarily due to sum-frequency wave effects.

Furthermore, significant responses around the second mode of the structure have been observed during slamming events in specific cases, as evidenced by both full-scale measurements (Hallowell et al., 2016) and experimental studies (De Ridder et al., 2011, Suja-Thauvin, Krokstad and Frimann-

Dahl, 2016, Bredmose et al., 2013). Suja-Thauvin and co-authors demonstrated that the dynamic amplification of the second mode of the structure can account for up to 20% of the maximum total response, thus showing that models that do not include slamming are likely to underestimate the response (Suja-Thauvin, Krokstad, Bachynski et al., 2017).

Lastly, wave run-up has been a common research topic, especially significant for large-diameter monopiles. Numerous methods have been developed to calculate the pressure due to wave run-up, but no universally accepted solution exists. At the point where the horizontal velocity of the wave-particle becomes zero, a vertical velocity is generated. This no longer follows the potential flow solution which results in an accelerated flow around the cylinder. Now a large pressure difference around the cylindrical structure is induced. Wave run-up has been observed for much longer than the previously mentioned phenomena. However, its nonlinear nature makes it challenging to fully integrate into load calculations. Recent studies have aimed to address wave run-up more accurately by considering various perspectives and their accompanying assumptions (Jeong et al., 2020, Wang et al., 2022, De Vos et al., 2007).

These observations underscore the significance of having models for external forces that can induce dynamic responses, particularly for the first and second modes, when designing a bottom-founded offshore wind turbine. In the North Sea, the assessment of structural response under extreme environmental conditions, often referred to as Ultimate Limit State (ULS) analysis (for elaboration reference is made to Deursen, 2023), adheres to established standards such as DNV-ST-0126, DNV-RP-C205, and IEC-61400-3 (DNV, 2021a, DNV, 2021c, IEC, 2019b). These standards recommend the use of the Morison equation (Morison et al., 1950) in conjunction with stream function theory wave kinematics (Rienecker and Fenton, 1981) for calculating hydrodynamic loads generated by extreme waves. When waves are breaking, a slamming model becomes necessary. For plunging breaking waves, the approach proposed by Wienke and Oumeraci in 2005 is typically applied, while for spilling breakers, the method developed in 2004 by Nestegard and coauthors is commonly employed. For an overview of the various types of breaking waves see the work done by Galvin and Figure 2 (Galvin, 1968).
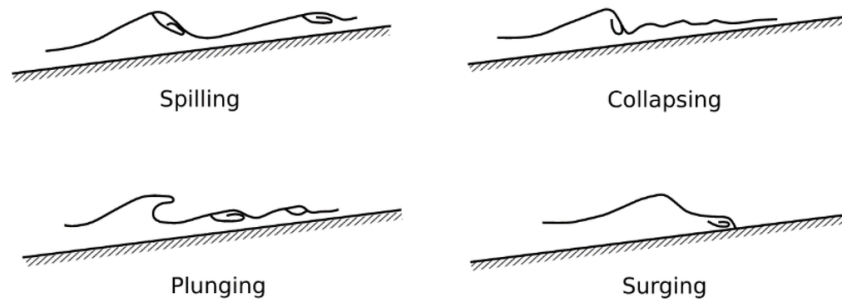
Figure 2: Breaking wave types (Federal Highway Administration, 2020).

1.3 Problem statement

All standardization organizations recommend the use of the Morison equation (Deursen, 2023). Which is shown in Equation 1, taken from the standard IEC-61400-3 (IEC, 2019b). Two coefficients are present in this equation, the drag coefficient (C_d) and the inertia coefficient (C_m).

$$F = \frac{1}{2}C_d\rho D|U_r|U_r + C_m\rho A\dot{U}_w - C_a\rho A\dot{U}_s \tag{1}$$

Where:

F	force per unit length of member
C_a	added mass coefficient ($C_a = C_m - 1$ for slender, cylindrical members of fixed structures)
U_r	relative velocity of the flow normal to the member
$\dot{U}_s$	acceleration of the structure resolved normal to the member
$\dot{U}_w$	acceleration of the flow resolved normal to the member
A	cross-sectional area of the member
ρ	the density of water

In section 9.5.2.3 of ISO 19902 guidance is provided for typical design situations regarding global hydrodynamic action for unshielded circular cylinders (See Table 1). Nevertheless, they foresee that this might be an oversimplification and therefore give extra guidance in section A.9.5.2.3 in a variety of circumstances. It should be noted that all standards agree on this particular matter (Deursen, 2023).

Table 1: Typical values of hydrodynamic coefficients, appropriate for situations of a steady current with negligible waves and for large waves with $U_{mo}T_i/D > 30$ (ISO, 2020).

Surface of component	C_d	C_m
smooth	0.65	1.6
rough	1.05	1.2

In the caption of Table 1, the subsequent variables are designated as:

U_{mo}	maximum horizontal water particle velocity at storm still water level under the wave crest from two-dimensional wave kinematics theory
T_i	intrinsic wave period
D	diameter of the structures legs at storm still water level

In section 9.5.2.3 of ISO 19902, it is explicitly mentioned that for situations where waves are dominant, but $U_{mo}T_i/D < 30$, C_m and C_d for nearly vertical members (within 15° of vertical) are modified by wake encounter and shall be specially determined (ISO, 2020). These circumstances refer to the fact that the coefficients in section 9.5.2.3 match measurements reasonably well in any particular half-wave cycle. However, the best-fit values vary from one half-wave cycle to another therefore accounting for subperiodic fluctuations. Most of the variation in C_d and C_m can be taken into account by expressing C_d and C_m as functions of the following 4 parameters:

- relative surface roughness $e = k/D$

- Reynolds number $R_e = U_m D/\nu$

- Keulegan-Carpenter number $K_c = U_m T/D$

- current/wave velocity ratio $r = U_c/U_{mo}$

Where:

k	average roughness height
D	effective diameter (including marine growth)
U_m	maximum speed (including current) normal to cylinder axis in a wave cycle
ν	kinematic viscosity of water
T	wave period
U_c	current speed measured in-line with the waves
U_{mo}	maximum wave-induced orbital velocity

In the work by Dummer, an initial endeavour was undertaken to introduce a set of instantaneous wave force coefficients aimed at accommodating subperiodic fluctuations (Dummer, 1988). This initiative was grounded in the hypothesis that employing traditional period-averaged, time-invariant drag and inertia coefficients in the Morison equation wave force prediction model is inaccurate. However, the outcomes proved inconclusive, primarily attributed to the computation of certain instantaneous negative drag coefficients, which lack physical relevance. This thesis documents a subsequent attempt which is further elaborated on in Section 1.4.

1.4   Research objective and questions

Within this section, the primary goal of the inquiry is articulated in the form of the research objective. Derived from this objective, the research questions were formulated, laying the foundation for the study. Lastly, the methodology for the specific objectives is outlined.

1.4.1   Research objective

The issue of employing traditional period-averaged, time-invariant drag and inertia coefficients in the Morison equation wave force prediction model, due to their inaccuracies, is examined in this thesis by introducing instantaneous wave force coefficients, as outlined in Section 1.3. To address this concern, the following primary research objective was formulated:

Determine whether the establishment of time-varying coefficients within the first and second-order irregular wave theory increases the accuracy of the wave loads, and investigate what the influence is of this newly established calculation technique on the fatigue life of an XXL monopile.

To contribute to achieving this goal, the following sub-objectives were established. It should be noted that Poseidon, Athena, and Titan are applications of MonoPoly, the software package by SLPE utilized in this thesis, and are discussed extensively in Section 2.4.

- Develop a time-varying hydrodynamic coefficient method that accounts for subperiodic fluctuations to accurately analyze irregular waves.

- Validate the newly developed method through experimental verification.

- Adapt the model to incorporate project-specific inputs, ensuring alignment with the hydrodynamic force generation in Poseidon.

- Modify the model to produce outputs compatible with structural response calculations in Athena.

- Conduct structural response calculations for a fatigue analysis representative of one defined in the standard IEC-61400-3 in Athena.

- Post-process the structural response calculation outputs from Athena in Titan.

- Collect and analyze output data from Titan, performing a comparative analysis between the newly developed method and the current industry-standard method.

- Investigate the sensitivity of the results by evaluating various parameters and configurations in defining the new method.

1.4.2 Research questions

The inquiries essential for achieving the objectives of the thesis were:

- How can a time-varying hydrodynamic coefficient method be developed to account for sub-periodic fluctuations in order to accurately analyze irregular waves?

- How can the newly developed time-varying hydrodynamic coefficient method be experimentally validated to ensure its accuracy and reliability?

- What modifications are necessary to adapt the time-varying hydrodynamic coefficient model to incorporate project-specific inputs, ensuring alignment with Poseidon's hydrodynamic force generation?

- How can the time-varying hydrodynamic coefficient model be modified to produce outputs that are compatible with structural response calculations in Athena?

- What representative fatigue analysis, as defined by the IEC-61400-3 standard, can be executed in Athena using the new method within the time frame of this thesis?

- How does the performance of the newly developed time-varying hydrodynamic coefficient method compare to the current industry-standard method based on output data from Titan?

- What is the sensitivity of the results to different parameters and configurations in the definition of the new time-varying hydrodynamic coefficient method?

1.4.3 Methodology

To attain the goals outlined in Subsection 1.4.1, the following methodology was employed:

- Develop a MATLAB-based script capable of calculating the hydrodynamic loading on a monopile by generating irregular waves and determining time-varying hydrodynamic coefficients using zero-crossings, the Keulegan-Carpenter number, and the Reynolds number.

- Reproduce regular and irregular wave experiments in terms of surface elevation, hydrodynamic force, and overturning moment using the MATLAB-based script.

- Convert the MonoPoly text input files to MATLAB structures and use these as input for the script that calculates the hydrodynamic loading.

- Output the hydrodynamic loading as member end forces in a binary-serialized array of single-precision floating-point values using the same serialization method as Poseidon.

- Establish different test cases using various parameters and configurations of the time-varying coefficient method in conjunction with the constant coefficient method.

- Reduce the number of load cases necessary for a fatigue analysis as defined by the IEC-61400-3 standard while maintaining representative outcomes.

- Generate hydrodynamic loading time series for all defined test and load cases using the MATLAB-based script.

- Run Athena and Titan for all considered load and test cases with the generated hydrodynamic loading time series from the script.

- Compare Titan's output configuration with standard fatigue assessment outcomes and post-process the data to present the results in a comparable format.

- Visualize results for all test cases, illustrating both the constant and time-varying coefficient methods, as well as the different parameters and configurations used.

1.5   Thesis outline

In Chapter 1, a brief introduction to bottom-founded offshore wind turbines is provided, along with the problem investigated in this thesis. The research objectives and corresponding research questions are also stated. Chapter 2 explores the theoretical framework essential for addressing the issue outlined in this thesis, covering hydrodynamics, wind profiles and spectra, and standard practices in fatigue analysis. It also includes an overview of the software used for calculating structural responses. Chapter 3 comprehensively describes the time-varying and constant-coefficient methods, facilitating replication for future research. Chapter 4 validates both methods by replicating experimental results to confirm their accuracy. Structural response calculations and fatigue assessments for the different methods are described, discussed, and evaluated in Chapter 5. The conclusions and recommendations are presented in Chapter 6.

2 Theoretical background

This chapter delves into the theoretical framework essential for tackling the issue outlined in Section 1.3, as well as for achieving the research objectives outlined in Section 1.4. Starting with examining hydrodynamics theory, encompassing both linear and second-order wave theory alongside irregular waves, Wheeler stretching, the Keulegan-Carpenter number, and the Morison and Rainey load models. Foundational hydrodynamic principles can be found in the book Water Waves, within this thesis they serve as the basis for writing the hydrodynamic theory part (Stoker, 1957). Additionally, the theory concerning wind profiles and spectra is explored. Furthermore, the theory about common practices in fatigue analysis is introduced. In Section 2.4, an overview of the software utilised for calculating structural responses is provided (SLPE, n.d.).

In this thesis, the coordinate system is defined with the origin at the still water level, located at the center of the monopile. The positive y-direction points upwards, and the positive x-direction points downstream, as illustrated in Figure 3.
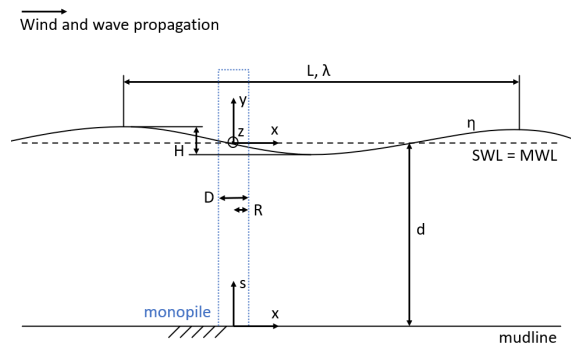
Figure 3: Coordinate system

2.1 Hydrodynamics

This section delves into the realm of hydrodynamics theory, encompassing the fundamental assumptions, applicability, and principal features/solutions of both linear and second-order wave theories, including their relevance to irregular seas. Additionally, the critical aspects of hydrodynamics such as Wheeler stretching and the Keulegan-Carpenter number are explored. Finally, the theoretical framework of the load models utilised within this thesis is presented.

2.1.1 Airy wave theory

Airy or linear wave theory finds application in analyzing propagating waves within both finite and infinite water depths, assuming a horizontal sea bottom and an infinite free surface. The foundational condition for this theory requires the wave height to be significantly smaller than the wavelength or water depth. This critical assumption facilitates the linearization of free surface boundary conditions by neglecting wave height terms beyond the first order. Consequently, these conditions can be satisfied at the mean water level rather than at the oscillating free surface.

Linear wave theory also rests on additional fundamental assumptions. It posits that the flow can be effectively described by a velocity potential, indirectly assuming an incompressible and irrotational flow. Moreover, the flow is presumed to be inviscid, in a steady state, and the waves are assumed to be long-crested and non-breaking.

Understanding the relationship between wavelength and water depth is crucial for distinguishing between shallow, intermediate, or deep waters. Figure 4 illustrates this connection for both deep water and intermediate water scenarios. In shallow and intermediate waters, where the water depth is small compared to the wavelength, the seafloor significantly influences wave characteristics.

Conversely, in deep water, the seabed has no impact on the waves. Submerged structures at depths exceeding half the wavelength of incoming waves are unaffected by wave kinematics. This condition is expressed by the relation $d/\lambda > 0.5$, where d represents the water depth at the structure's base, and λ is the wavelength.
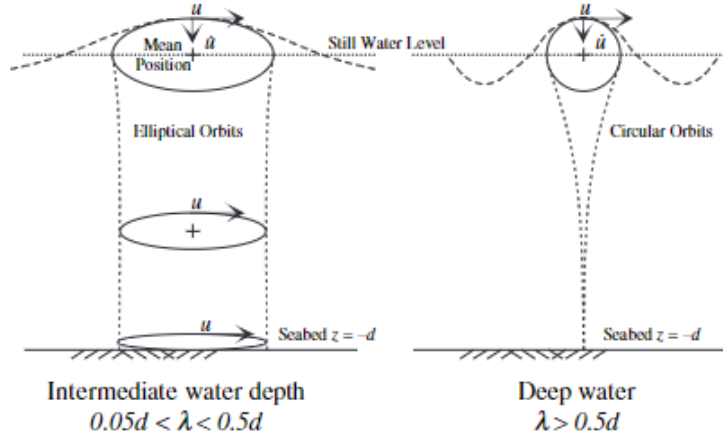
Figure 4: Water particle motion according to Airy linear wave theory (Veldkamp and Tempel, 2005).

Particle kinematics involve horizontal and vertical velocity as well as acceleration, derived from the surface elevation equation. In deep water, particles trace a circular path, whereas, in intermediate and shallow water, the trajectory transforms into an elliptical shape. Obtaining horizontal and vertical velocities involves the velocity potential in waves and the dispersion relation. Velocities and accelerations exhibit variations in shallow, intermediate, and deep waters. For detailed derivations, reference is made to the book Water Waves and the project thesis (Stoker, 1957). The general expressions for water-particle velocities in the x and y directions are typically given by Equation 2, where $\Theta = kx - \omega t$.

$$
\begin{aligned}
u &= \frac{\partial \Phi}{\partial x} = \frac{\pi H}{T} \frac{\cosh ks}{\sinh kd} \cos \Theta \\
v &= \frac{\partial \Phi}{\partial y} = \frac{\pi H}{T} \frac{\sinh ks}{\sinh kd} \sin \Theta
\end{aligned}
\tag{2}
$$

The water-particle accelerations in the x and y direction are given by

$$
\begin{aligned}
\frac{\partial u}{\partial t} &= \frac{2\pi^2 H}{T^2} \frac{\cosh ks}{\sinh kd} \sin \Theta \\
\frac{\partial v}{\partial t} &= -\frac{2\pi^2 H}{T^2} \frac{\sinh ks}{\sinh kd} \cos \Theta
\end{aligned}
\tag{3}
$$

In the context of linear theory, which primarily seeks a first-order solution, only the initial term of the series in Φ and η is retained during substitution into the free surface boundary conditions. Here Φ represents the velocity potential and η represents the free surface elevation. In Figure 5 a visualisation of the applicability of linear theory is given.
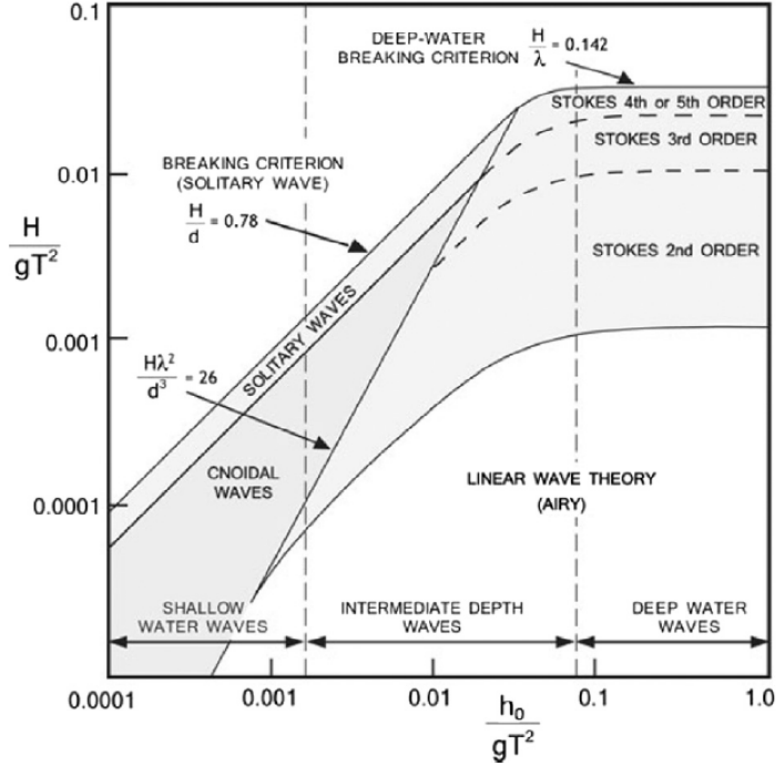
Figure 5: Applicability ranges of various waves (LeMéhauté, 1976).

Upon examining the expressions for horizontal and vertical velocities, it becomes apparent that the horizontal velocity of a water particle reaches its maximum (or minimum) when the vertical velocity is zero, and vice versa. Due to the typical amplitude disparity between these velocities, one can deduce that a water particle follows an elliptical path around its mean position throughout a complete wave cycle.

2.1.2   Linear irregular sea

Generating irregular sea conditions for wind turbine calculations commonly involves the utilization of linear airy waves. These waves are formed by combining regular waves, with the amplitudes of the components determined by the wave spectrum. Mathematically, this process corresponds to conducting an inverse Fourier transform of the wave spectrum. In the context of a two-dimensional long-crested sea, this can be expressed as follows

$$\eta(x,t) = \sum_{i=1}^{N} A_i \sin\left(\omega_i t - k_i x + \epsilon_i\right) \tag{4}$$

In the given expression, A_i represents the amplitude of component i, ω_i stands for the angular frequency of component i, x denotes the spatial coordinate, and ϵ_i represents a random phase angle. To ensure a statistically accurate representation, the amplitude must be determined based on the wave spectrum. The amplitude can mathematically be expressed as (Faltinsen, 1990):

$$A_i = \sqrt{2S(\omega_i)\Delta\omega} \tag{5}$$

In this context, $\Delta\omega$ signifies the integral width of a given frequency.

This approach yields a linear irregular wave, which can be rendered directional by incorporating a directional spectrum when necessary. However, it is important to note that the wave characteristics employed for computing the loads on the structure are fundamentally known only up to the mean free surface. To acquire the wave characteristics all the way up to the free surface, multiple techniques are available. One frequently employed technique is Wheeler stretching, which is discussed in detail in Subsection 2.1.3. Additionally, stretching is used due to high-frequency contamination, also referred to as bound waves (Forristall, 1985).

2.1.3 Wheeler stretching

Given the widespread adoption of stretching in linear wave kinematics, it is valuable to provide an overview of one of the most commonly used techniques. It is important to note that neither of these techniques appears to have a robust physical rationale; instead, they are employed as "engineering approximations". Among these techniques, Wheeler stretching is the most prevalent. This method involves stretching the wave kinematics in such a way that the velocity, as per linear theory, is applicable at $y = 0$, extending all the way to the free surface. In Figure 6 a visualisation is given which indicates the linear theory kinematics and the Wheeler stretched kinematics. Essentially, the stretching entails a shift in the coordinate system, where the stretched vertical coordinate, denoted as y_s, is expressed as presented in Equation 6 (Stansberg and Gudmestad, 1996).

$$y_s = \frac{y - \eta}{1 + \frac{\eta}{d}} \tag{6}$$
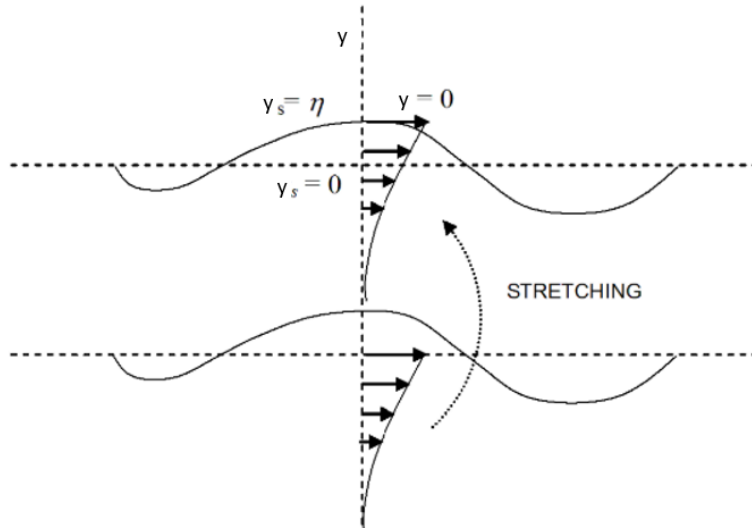
Figure 6: Stretching of the velocity profile (DNV, 2021c).

The method was originally introduced by Wheeler and has become a common practice for calculating wave forces arising from irregular seas (Wheeler, 1970). Nevertheless, this technique lacks a robust physical foundation and is primarily rooted in the observation that real-world fluid velocity at the still water level is lower than the predictions from linear theory (DNV, 2021c).

In the original paper, the author acknowledges that when the coordinate shift is introduced in the decay function, it no longer adheres to Laplace's equation. As a result, it should be considered an empirical method and, ideally, replaced with a more accurate model.

According to Stansberg, who compared various methods for predicting kinematics with results obtained via laser Doppler velocimetry, including Wheeler stretching, it was found that the Wheeler method significantly underestimates velocities at all depth levels when applied in combination

with wave elevation calculated as a sum of linear waves, particularly in steep waves (Stansberg, Gudmestad and Haver, 2008). The magnitude of the error falls within the range of $0.5k_0A_0$ to $0.75k_0A_0$, where k_0A_0 represents the local wave steepness.

The same paper indicates that if Wheeler stretching is based on a measured time series or a second-order wave kinematics model, the accuracy improves at the free surface. However, these errors still persist below $y = 0$.

As mentioned, the method has become a common practice for calculating wave forces arising from irregular seas. The normal technique for calculating these forces involves integrating the sectional force, which is calculated using kinematics, up to the instantaneous free surface. This means that within linear theory assumptions are made for the kinematics following the instantaneous free surface to account for the difference between the Still Water Level (SWL) and this free surface. In the integration that incorporates Wheeler stretching, the modified coordinate, y_s, is used in the decay function for the wave kinematics. As a result, the integration over the wetted surface is carried out up to the time-varying free surface elevation, resulting in a force that is proportional to η^2. Here, one order of magnitude arises from the wave kinematics, and the second order arises from the integration to a dynamic free surface.

This approach leads to the generation of sum-frequency forces in the case of finite water depths. Had consistent linear theory been employed, the integration would have extended to the mean free surface, resulting in an expression devoid of the factor $1 + \frac{\eta}{d}$ and the exclusion of the second term.

2.1.4   Stokes wave theory

The linear small amplitude wave theory, formerly referred to as Airy wave theory, represents the initial and simplest approximation for the water wave boundary value problem. It encompasses a single frequency component characterized by a sinusoidal wave with the frequency denoted as ω. It is worth noting that successive approximations to this theory can be achieved using the perturbation technique.

Stokes employed this approach with the intention that higher-order solutions are roughly an order of magnitude smaller than the immediate lower-order ones. This method is considered valid when certain conditions are met, specifically when $H/d << (kd)^2$, for $(kd) < 1$, and $H/L << 1$. For detailed derivations, reference is made to the book Water Waves and the project thesis (Stoker, 1957). These conditions impose significant limitations on the wave heights, particularly in shallow water, which is why Stokes' theory is generally not applicable to shallow water. A visualisation of the applicability of Stokes' second-order wave theory is given in Figure 5.

Stokes wave theory, similar to linear theory, assumes small wave amplitudes, long-crested waves, potential flow, and an inviscid fluid.

The second-order water-particle velocities are

$$
\begin{aligned}
u =& \frac{\pi H}{T}\frac{\cosh ks}{\sinh kd}\cos\Theta + \frac{3}{4}\Big(\frac{\pi H}{L}\Big)\frac{\pi H}{T}\frac{\cosh 2ks}{\sinh^4 kd}\cos 2\Theta \\
v =& \frac{\pi H}{T}\frac{\sinh ks}{\sinh kd}\sin\Theta + \frac{3}{4}\Big(\frac{\pi H}{L}\Big)\frac{\pi H}{T}\frac{\sinh 2ks}{\sinh^4 kd}\sin 2\Theta
\end{aligned}
\tag{7}
$$

The water-particle accelerations can be readily determined from these expressions through differentiation.

$$
\begin{aligned}
\frac{\partial u}{\partial t} =& \frac{2\pi^2 H}{T^2}\frac{\cosh ks}{\sinh kd}\sin\Theta + \frac{3\pi^2 H}{T^2}\Big(\frac{\pi H}{L}\Big)\frac{\cosh 2ks}{\sinh^4 kd}\sin 2\Theta \\
\frac{\partial v}{\partial t} =& -\frac{2\pi^2 H}{T^2}\frac{\sinh ks}{\sinh kd}\cos\Theta - \frac{3\pi^2 H}{T^2}\Big(\frac{\pi H}{L}\Big)\frac{\sinh 2ks}{\sinh^4 kd}\cos 2\Theta
\end{aligned}
\tag{8}
$$

2.1.5 Second-order irregular sea

In the work presented by Marthinsen and Winterstein, a second-order irregular wave model is introduced, designed to accommodate arbitrary water depths (Marthinsen and Winterstein, 1992). This model is based on the assumption of long-crested Stokes waves up to the second order, with the first-order solution aligning with what was previously discussed in the preceding section. For the precise expressions of the second-order potential and wave elevation, interested readers are directed to the original paper, as these expressions involve intricate mathematical complexities.

The surface elevation is defined as $\eta = \eta^{(1)} + \Delta\eta^{(2)}$, where the latter term constitutes a second-order correction to the linear surface elevation. The statistical characteristics of this model have been explored in the original paper. The skewness and kurtosis exhibit strong agreement with observations obtained from radar measurements conducted in the Ekofisk field of the North Sea. However, comparisons with buoy measurements yield less favorable results, likely due to the methodology used by the wave rider buoy for calculating wave heights.

In Stansberg's research in 1995, this model was subjected to further investigation and compared with results from a laboratory-generated wave field. It was found that for moderately steep waves, both the dispersion and elevation of the model align well with the measurements. However, for the steepest waves, there is an under-prediction of crest height by 5% to 10%, and the dispersion exhibits some deviations from the measurements.

The kinematics of the wave particles are modeled as a composite of three contributions: first-order velocity potential up to the mean water level, linear extrapolation of the first-order potential to the linear free surface, and second-order potential up to the mean water level, followed by vertical extrapolation to the linear free surface.

The formulations for horizontal velocity are (Stansberg, Gudmestad and Haver, 2008)

$$
\begin{aligned}
u^{tot}(y) &= u^1(y) + u^{(2,sum)}(y) + u^{(2,diff)}(y) \quad \text{for} \quad y \leq 0 \\
u^{tot}(y) &= u^1(0) + \frac{\partial u^1}{\partial y}\big|_{y=0}y + u^{(2,sum)}(0) + u^{(2,diff)}(0) \quad \text{for} \quad y > 0
\end{aligned}
\tag{9}
$$

The characteristics of wave motion have been examined in various studies and have been compared against measurements obtained through a laser Doppler velocimetry system (Stansberg, Gudmestad and Haver, 2008). The results indicate a favorable agreement with experimental data, although some discrepancies are observed, particularly in the case of the steepest waves.

It is important to note that this method relies on the assumption of a narrow-banded process. Consequently, if the wave spectrum contains a wide range of frequencies, the applicability of this method is limited. It is advised to employ a low-pass filter with a cutoff frequency of (Stansberg, Gudmestad and Haver, 2008)

$$
\omega_{high} = \sqrt{k_{High}g}
\tag{10}
$$

Here, k_{High} is defined by the upper frequency by linear dispersion, and it is determined as $k_{High} = 2/H_s$.

The rationale behind this approach is to consistently represent the kinematics up to the linear free surface. When kinematic properties are reliably known up to the linear free surface of the incident wave to the first order, it becomes feasible to consistently calculate second-order forces. This capability is essential for capturing sum frequencies, enabling precise predictions of resonant oscillations in the support structure.

2.1.6 Keulegan Carpenter number

Based on the assumption of potential flow theory, the coefficient C_m is expected to be 2, and it is reasonable to expect that the value of C_d would be consistent with that seen in constant velocity scenarios. Morison and his collaborators determined specific values for C_d and C_m by analyzing observed forces during phases of the wave cycle where either the velocity U or its time derivative dU/dt becomes zero. These determinations revealed significant deviations of C_m from the theoretical value and of C_d from the steady-state value at the corresponding Reynolds number.

In field studies conducted at Caplen, Texas, Reid observed similar variations in C_m and C_d (Reid, 1956), demonstrating discrepancies from theoretical and steady-state values, respectively. Notably, these coefficient variations were not associated with any specific parameter until 1958.

In the work done by Keulegan and Carpenter, an investigation was undertaken with two objectives in mind (Keulegan and Carpenter, 1958). Firstly, it aimed to introduce a supplementary function ΔR into the Morison equation to provide a more accurate representation of force. This adjustment was made considering the coefficients C_m and C_d as constant throughout a given wave cycle. The inclusion of the term ΔR was deemed necessary to account for deviations in the point values of C_m and C_d from their average values.

The second objective was to explore the potential correlation between the average values of C_m and C_d and a parameter denoted as $U_m T/D$, where U_m represents the amplitude of the harmonically varying velocity, T is the period of oscillations, and D is either the diameter of a cylinder or the breadth of a rectangular plate. In the original paper, this parameter was referred to as the period parameter, now recognized as the K_c number, standing for the Keulegan Carpenter number.

By selecting the midsection of a rectangular basin experiencing standing waves as a representation of a field with harmonically varying currents, and positioning the cylinders horizontally beneath the water surface, the study revealed variations in the average values of inertia and drag coefficients throughout a wave cycle. These variations were observed when altering the intensity of the current and adjusting the size of the cylinders. Specifically, the inertia coefficient C_m deviates from the theoretical value of 2 as the cylinder diameter changes or, for a given cylinder, as the maximum current varies. Similar variations were noted in the drag coefficient C_d, with changes manifesting as additions to the values observed in a steady flow. Interestingly, no apparent correlation between these coefficients and Reynolds number was identified. Conversely, when these coefficients were examined in relation to the period parameter, distinct and systematic dependencies were observed.

As the period parameter transitions from smaller to larger values for the cylinders, the inertia coefficient initially decreases from its starting point at 2 to a minimum value of 1.00 when $U_m T/D = 15$. Subsequently, it gradually rises, reaching a value of 2.5 at $U_m T/D = 120$. Concerning the drag coefficient, there is an initial increase from 0.9 to a peak at 2.5 when $U_m T/D = 15$, followed by a gradual decrease to the steady flow value. It is noteworthy that, for the cylinders, the vicinity around $U_m T/D = 15$ appears to be a critical region.

When examining the data for cylinders, if the period parameter is either sufficiently small or sufficiently large, the forces can be calculated based on Equation 11, with the remainder function ΔR being negligible. However, for period parameters near the critical value of $U_m T/D = 15$, a more accurate representation of forces is achieved using Equation 12, where the remainder function becomes significant.

$$\frac{F}{\rho U_m^2 D} = \frac{\pi}{4} C_m \cdot \frac{D\sigma}{U_m} \sin\theta - \frac{C_d}{2} |\cos\theta| \cos\theta \tag{11}$$

$$\frac{F}{\rho U_m^2 D} = \frac{\pi}{4} C_m \cdot \frac{D\sigma}{U_m} \sin\theta - \frac{C_d}{2} |\cos\theta| \cos\theta + \Delta R \tag{12}$$

The investigation into flow patterns around the cylinders, with varying values of $U_m T/D$, was conducted due to the potential impact on the nature of forces throughout a cycle being influenced

by the period parameter. The examination of flow patterns involved visually observing the flow by introducing a jet of colored liquid on one side of the immersed object. The arrangement of the liquid in proximity to the object during cyclic motion was documented using both a still camera and a motion-picture camera. The results are shown in Figure 7.

The images presented in Figure 7, labeled as a and b, were captured using a 3-inch cylinder. The first image corresponds to $U_mT/D = 4$, while the second corresponds to a larger value, $U_mT/D = 10$. When the period parameter is small, there is no flow separation; the liquid near the cylinder adheres to it, and the division of flow from above and below is symmetrical. It is worth noting that at low period parameters, the inertia coefficient is approximately equal to the theoretical value of 2, and drag is negligible.

As U_mT/D increases, flow separation occurs at the top surface of the cylinder during the relatively longer duration when the flow persists in one direction. Although not visible in the image, shortly thereafter, before the current reverses, the liquid that has come around the cylinder from below moves upward and, while transforming into an eddy, remains in close proximity to the cylinder.

In Figure 7, c, the flow pattern is showcased for $U_mT/D = 17$ using the 2-inch cylinder. Notably, there is a distinct separation at the upper surface of the cylinder, followed by the flow around the lower surface directed upward, leading to the subsequent formation of an eddy. A markedly different scenario unfolds for a large period parameter, as depicted in Figure 7, d, captured with the 0.5-inch cylinder at $U_mT/D = 110$. In this case, one encounters the characteristic Karman vortices, where the eddies are alternately separated from above and below.

The observed characteristics of the eddies discussed above lead to a plausible interpretation of the physical significance of U_mT/D. If we define a length, denoted as l, as the distance that a fluid particle would traverse in one direction in the absence of the cylinder, then $l = U_mT/\pi$. Consequently, $U_mT/D = \pi l/D$, indicating that the period parameter is proportional to the ratio of the distance traveled by a particle during a half cycle to the diameter of the cylinder. When the period parameter equals 15, l/D is 4.8. It is conceivable that when U_mT/D is smaller than 15, the distance covered by a particle is insufficient to form complete eddies. When it equals 15, the distance becomes adequate to form a single eddy, and for values much larger than 15, the greater distances facilitate the formation of numerous vortices in the characteristic Karman vortex street.

The resemblance between the period parameter and the Strouhal number is notable, and the product of the Strouhal and period parameter numbers offers an alternative parameter that proves as useful as the period parameter itself (McNown and Keulegan, 1959). If T_s represents the duration for the shedding of a single eddy, then the Strouhal number $fD/U = S$ can be expressed as $D/(2T_sU) = S$, given that the number of alternate eddies shed during a second is $2f$ and $2fT_s$ equals 1 second. It is reasonable to assume that this relationship is approximately valid for sinusoidal motions as well, provided U is replaced by $U_m/2$. Hence, the Strouhal number for sinusoidal motion is given by $D/(U_mT_s) = S$.

Multiply the two sides by the wave parameter number U_mT/D and ignoring the dependence of S on the Reynolds number we get $T/T_s = 0.2U_mT/D$

As previously mentioned for the cylinders, the inertia coefficient C_m reaches its minimum value, slightly below unity, at approximately $U_mT/D = 12.5$. This condition corresponds to $T/T_s \approx 2$, indicating that during a half cycle, or a complete motion of a fluid particle in one direction, a single eddy is formed and subsequently separated (also seen in Figure 7, b). The process of eddy shedding significantly influences the fluctuations in the so-called coefficients of mass and drag. This aspect must be considered in the theoretical formulation of the fundamental process.
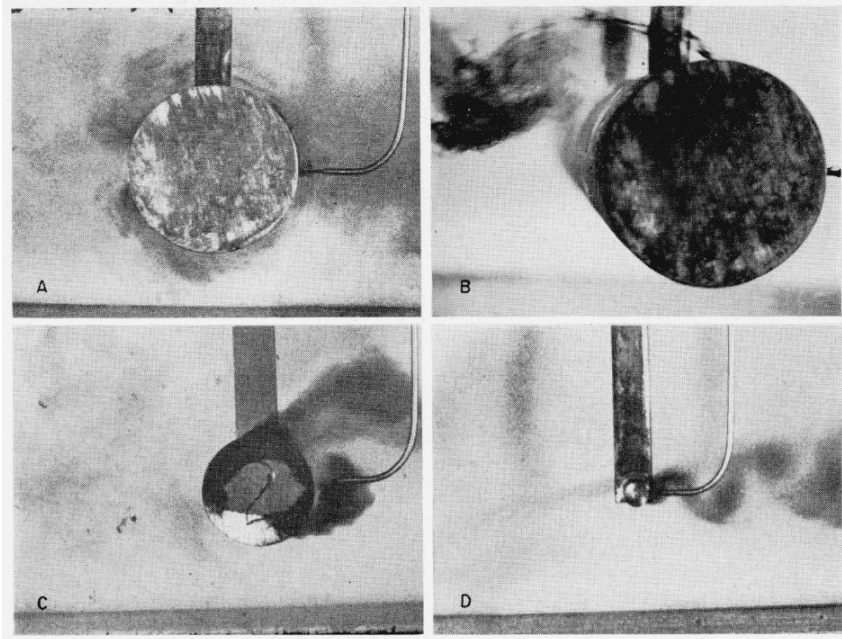
Figure 7: Flow patterns around cylinders. (**A**) $D = 3''$, $U_m T/D = 4$; (**B**) $D = 3''$, $U_m T/D = 10$; (**C**) $D = 2''$, $U_m T/D = 17$; (**D**) $D = 0.5''$, $U_m T/D = 110$;, taken from Keulegan and Carpenter, 1958.

In conclusion, the Keulegan-Carpenter number in physical terms, denoted as K_c, is directly proportional to the ratio of the horizontal distance covered by a water particle during a wave cycle to the diameter of the cylinder. This ratio serves as an indicator of whether inertial or viscous effects play a dominant role in fluid-structure interaction. Specifically, for small K_c values, water particles cover relatively short distances compared to the cylinder diameter. In such cases, both flow separation and wake generation effects are diminished, if not entirely eliminated. As a result, inertial effects take precedence for small K_c values. On the other hand, for large K_c, water particles travel considerable distances beyond the cylinder. This scenario approaches steady flow conditions, where viscous effects from flow separation and wake generation become predominant. Consequently, wave flows characterized by high K_c values are primarily influenced by drag.

The parameter K_c also serves as an indication of the significance of wake encounter for members nearly vertical (within 15° of vertical) in waves. As fluid moves across a member, it generates a wake. When oscillatory flow reverses, fluid particles in the wake return earlier and impact the member with higher velocity than undisturbed fluid particles. With larger K_c, the wake travels a greater distance, decays more before returning to the cylinder, and is less likely to impact the cylinder, especially if the waves are multidirectional or if there is a current component normal to the principal wave direction. For very large K_c, the impact of wake encounter may be negligible. Conversely, for smaller K_c, wake encounter amplifies the drag action for nearly vertical members above its quasi-steady value, estimated from undisturbed fluid velocities.

2.1.7 Morison load model

The Morison equation represents a semi-empirical model for quantifying hydrodynamic forces acting on an object in the direction of incoming waves (Morison et al., 1950). This equation comprises three distinct components. The first component arises from the pressure field generated by undisturbed waves, commonly referred to as the Froude-Krylov force (illustrated in the first part of the first term in Equation 13 since $C_m = 1 + C_a$). The second component is attributed to the inertia of the encompassing fluid, necessitating acceleration, known as the added mass (depicted as the second part of the first term in Equation 13 since $C_m = 1 + C_a$). The final component originates from viscous drag (depicted as the second term in Equation 13).

$$F_{Morison} = \int_{-h}^{\eta} [\frac{1}{2}\rho C_d D u|u| + C_m \rho \pi R^2 a]dy \tag{13}$$

Where:

u	$=$	$u(y,t) - \dot{X}(y,t)$
a	$=$	$a(y,t) - \ddot{X}(y,t)$
$u(y,t)$		horizontal particle velocity
$\dot{X}(y,t)$		horizontal structural velocity
$a(y,t)$	$=$	$\frac{du(y,t)}{dt}$
$a(y,t)$		horizontal particle acceleration
$\ddot{X}(y,t)$		horizontal structural acceleration

Within this equation, the coefficients representing added mass (C_m) and drag (C_d) must be ascertained through empirical relationships. It is important to note that the Morison equation is only applicable to slender objects, where the diffraction of waves can be greatly simplified. Specifically, for a vertical cylinder, this equation holds when the extension along the wave direction (in the case of a vertical cylinder, the diameter D) is notably smaller than the wavelength (λ), as expressed by the condition: $\lambda/D < 5$.

The application of Morison's equation near the free surface necessitates a precise estimation of the undisturbed velocity distribution under a wave crest. This precision is crucial because utilizing the linear solution introduces an error near the free surface, where nonlinear wave effects become significant. In principle, Morison's equation should not be employed at the free surface due to its prediction of the largest force per unit length at that location. In reality, the force per unit length should diminish to zero as we approach the free surface, as it must match the atmospheric pressure. Nevertheless, in practice, Morison's equation is still utilised.

Morison's equation can be adapted to account for the horizontal motion of the body in the x direction. According to the formula, the drag-force contribution is linked to the relative velocity between incident waves and the body, while the remaining force contribution does not rely solely on the relative acceleration. This can be grasped by considering that, in potential-flow theory, the Froude-Kriloff force depends exclusively on the incident-wave acceleration, rather than the rigid-body acceleration.

An additional modification to Morison's equation can be achieved by incorporating the findings of MacCamy and Fuchs. They developed an analytical method for computing wave loads on cylinders, which can be applied to derive an equivalent inertia coefficient across all values of λ/D (MacCamy and Fuchs, 1954). Through the utilization of the velocity potential of the incident wave, coupled with linear wave theory, MacCamy and Fuchs demonstrated that the force per unit length can be expressed as depicted in Equation 14 (Malik, 2016). Where kr was substituted for $\frac{\pi D}{\lambda}$ since r' no longer refers to the radial coordinate in the velocity potential as by MacCamy and Fuchs but the radius of the cylinder.

$$dF_{MacCamyFuchs} = \frac{2\rho g H}{k} \frac{\cosh(k(h+y))}{\cosh(kh)} A(\frac{\pi D}{\lambda}) \cos(\omega t - \alpha(\frac{\pi D}{\lambda})) \tag{14}$$

Where

$$A(\frac{\pi D}{\lambda}) = \frac{1}{\sqrt{(J_1'(\frac{\pi D}{\lambda}))^2 + (Y_1'(\frac{\pi D}{\lambda}))^2}}$$

$$\alpha(\frac{\pi D}{\lambda}) = \arctan\frac{J_1'(\frac{\pi D}{\lambda})}{Y_1'(\frac{\pi D}{\lambda})} \tag{15}$$

In this context, J_1' and Y_1' denote the derivatives of the Bessel functions of the first and second kind, respectively. The variables H and h correspond to the wave height and total depth, while y represents the vertical position. Additionally, k stands for the wave number, ω for the wave frequency, and D for the diameter of the cylinder.

The cumulative force on the cylinder, obtained by integrating across the length of the cylinder, is depicted as shown in Equation 16 (Malik, 2016).

$$F_{MacCamyFuchs} = \int_{-h}^{0} dF_{MacCamyFuchs} dy = \frac{2\rho H A(\frac{\pi D}{\lambda})}{k^2} \frac{\omega^2}{k} \cos\alpha \cos\omega t + Q \sin\omega t \qquad (16)$$

By comparing Equation 16 to Morison's equation, an equivalent inertia coefficient can be found.

$$C_m^{eq} = \frac{4A(\frac{\pi D}{\lambda})}{\pi^3} (\frac{\lambda}{D})^2 \cos\alpha \qquad (17)$$

As illustrated in Figure 8, diffraction becomes significant when $\lambda/D \leq 5$. A consistent value of $C_m = 2$ closely aligns with the analytical value from MacCamy-Fuchs for long waves ($\lambda/D > 5$). However, for shorter waves, this constant value will notably overestimate the forces.
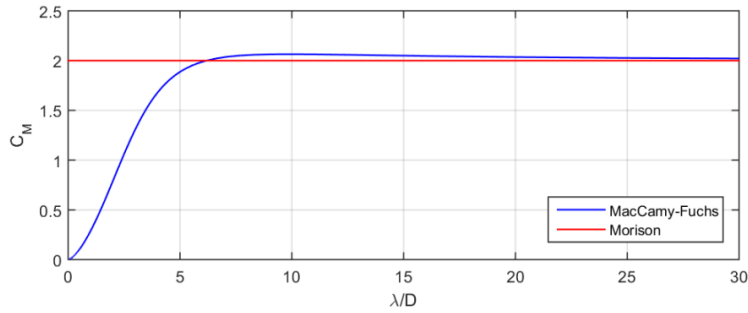
Figure 8: Inertia coefficients, C_m [1](Malik, 2015)

2.1.8 Rainey force model

Morison's equation (Morison et al., 1950), has been expanded upon in the works of Rainey (Rainey, 1989 and Rainey, 1995). This extension introduces two additional terms. The first term addresses the distributed horizontal force, acknowledging that while the cylinder maintains slenderness in the horizontal dimension, it departs from slenderness in the vertical dimension with respect to the wavelength. This component aligns with a more contemporary force model presented by Kristiansen and Faltinsen (Kristiansen and Faltinsen, 2017). The second term introduces a point force applied at the intersection of the cylinder's surface and the surrounding fluid to account for the alteration in fluid kinetic energy resulting from variations in the submerged length of the cylinder.

The Rainey load model, grounded solely on energy conservation principles, avoids specific assumptions about incoming wave characteristics, instead relying on the maintenance of cylinder slenderness and the preservation of the water surface, known as the "wavy lid assumption". However, it is noteworthy that the model's validity is challenged by Stokes's expansion, which diverges

---

[1]It should be noted that the figure shows C_M instead of C_m due to a difference in definition between this document and the originating document which is from Malik, 2015.

when the wave height is of comparable size to the structural diameter, rendering the theory invalid (Rainey, 1995). Additionally, the model assumes structural members are slender ($\lambda \geq 10D$), further constraining its applicability (Rainey, 1990).

Although the point force introduced in the Rainey model differs from the term denoted as F^ψ in Kristansen's and Faltinsen's work (Kristiansen and Faltinsen, 2017), a recent investigation conducted by Suja-Thauvin has determined that the third-harmonic components of these two terms exhibit agreement in the presence of large waves (Suja-Thauvin, Bachynski et al., 2020).

The key equations from Rainey's load model are presented below (Rainey, 1989 and Rainey, 1995).

$$F_{Rainey} = \int_{-h}^{\eta} [\underbrace{\frac{1}{2}\rho C_d D u|u| + C_m \rho \pi R^2 a}_{\text{Morison}} + \underbrace{\rho \pi R^2 C_a \frac{\partial w(y,t)}{\partial y}u}_{F_A}]dy - \underbrace{\frac{1}{2}\rho \pi R^2 C_a \frac{\partial \eta}{\partial x}u^2}_{F_I} \tag{18}$$

Where:

u	$=$	$u(y,t) - \dot{X}(y,t)$
a	$=$	$a(y,t) - \ddot{X}(y,t)$
$u(y,t)$		horizontal particle velocity
$\dot{X}(y,t)$		horizontal structural velocity
$a(y,t)$	$=$	$\frac{du(y,t)}{dt}$
$a(y,t)$		horizontal particle acceleration
$\ddot{X}(y,t)$		horizontal structural acceleration
$w(y,t)$		vertical particle velocity

2.2 Wind

The wind characteristics at a specific location can be determined by analyzing historical data on wind speed, direction, and spectrum. Wind speed and direction are crucial for assessing the aerodynamic load distribution, especially for the blades of a Wind Turbine Generator (WTG) and the overall system simulation. The wind loads on the blades, resulting from wind pressures, are proportional to the square of the wind velocity. For brevity, this text assumes the reader is familiar with basic relationships, as summarized and discussed by H. Söker (Söker, 2013).

In terms of load and safety considerations, the International Electrotechnical Commission (IEC) divides the wind regime into normal and extreme wind conditions. Normal wind conditions pertain to the frequently occurring conditions during typical wind turbine operation, while extreme wind conditions have a defined return period of either 1 year or 50 years.

Wind conditions encompass a constant mean flow, denoted as V, often accompanied by a deterministic gust profile or turbulence. Turbulence refers to random variations in wind velocity from 10-minute averages. The turbulence model incorporates the impacts of varying wind speed, shears, and direction, allowing for rotational sampling through changing shears. Depending on the wind turbine class, a classification established by the IEC to streamline turbine-specific standards, different turbulence models must be satisfied by the random wind velocity field.

The subsequent two subsections delve into the description of both wind profiles and wind spectrum.

2.2.1 Wind profile

In the wind industry, the power law and logarithmic law are commonly employed to establish the wind profile. This is essential because wind speed varies non-uniformly with height. Defining wind profiles requires specific atmospheric parameters and the wind speed at a defined height above

the mean water level. Utilizing these parameters, the wind speed at any selected height can be determined (Nybø et al., 2020). According to the standard IEC-61400-1, the normal wind speed profile is described by the power law, as illustrated in Equation 19.

$$V(y) = V_{hub}(y/y_{hub})^{\alpha} \tag{19}$$

In Equation 19, $V(y)$ represents the average wind speed as a function of height, denoted as y, above sea level. V_{hub} and z_{hub} signify the average wind speed at hub height and the height of the hub, respectively. The term hub refers to the fixture connecting the blades to the rotor shaft in a wind turbine. The power law exponent, α, can be reasonably assumed to be 0.2 (IEC, 2019a). This wind profile is also considered to characterize the average vertical wind shear across the rotor-swept area.

For the steady extreme wind profile, the extreme wind speed, V_{e50}, associated with a 50-year return period, and the extreme wind speed, V_{e1}, associated with a 1-year return period, as outlined in Equation 20, can be employed. In this equation, V_{ref} represents the reference wind speed, typically determined through project-specific measurements.

$$\begin{aligned} V_{e50}(y) &= 1.4 V_{ref}(y/y_{hub})^{0.2} \\ V_{e1}(y) &= 0.8 V_{e50}(y) \end{aligned} \tag{20}$$

Regarding the turbulent extreme wind speed model, the 10-minute average wind speeds, expressed as functions of y and associated with return periods of 50 years and 1 year, respectively, are specified in Equation 21.

$$\begin{aligned} V_{50}(y) &= V_{ref}(y/y_{hub})^{0.11} \\ V_{1}(y) &= 0.8 V_{50}(y) \end{aligned} \tag{21}$$

2.2.2 Wind spectrum

The incoming wind exhibits fluctuations around a mean value during its operation, rendering it irregular. To characterize this variability, a wind spectrum can be established based on various site-specific parameters. This spectrum elucidates how wind speed fluctuates around the mean wind speed with frequency. Several options are available for wind spectra, including the Kaimal spectrum, Von Karman spectrum, and the Frøya spectrum.

According to the IEC standards for standard wind turbine classes, the Kaimal model, in conjunction with a coherence model explicitly outlined in IEC-61400-1, is recommended. The Kaimal spectrum assumes turbulence that is both homogeneous and stationary over time and space, displaying isotropic behavior and adhering to a Gaussian distribution. Additionally, it presupposes that the vertical wind profile follows a logarithmic law. For a more in-depth understanding of the Kaimal spectrum and the coherence model, further details can be found in the standard IEC-61400-1 (IEC, 2019a).

2.3 Fatigue

The International Organisation for Standardization (ISO) defines fatigue as the cumulative damage done by repeated application of time-varying stresses at a specific location in the structure (ISO, 2020). This thesis adopts the same definition, attributing these time-varying stresses to variable actions. While wave action in the in-place situation during the design service life is a primary source of variable stresses causing fatigue in offshore structures, other contributors are acknowledged but not explored within this thesis.

In the design phase, it is common practice to evaluate fatigue by analyzing S-N data. In certain instances, fatigue life can be alternatively evaluated through fracture mechanics methods. However, these methods are deterministic and are not widely applicable in general design due to computational complexities. Fracture mechanics is primarily employed to assess the remaining fatigue life of components that already possess cracks.

Theoretical descriptions of crack growth induced by time-varying (tensile) stresses often rely on the Paris-Erdogan law of fracture mechanics. However, determining the endurance of a material or structural detail typically requires empirical testing of the specific detail. Test results are presented as pairs of values denoting the applied stress range, S, and the corresponding number of cycles to failure, N. Conducting tests for various S values and tallying the associated N values produces an S-N curve. This curve delineates the material or structural detail's resistance to constant amplitude variable stresses of different magnitudes, with the relationship between S and N following an exponential pattern. On double logarithmic scales, the S-N curve manifests as a straight line.

When tests are replicated under similar conditions (to the extent that test conditions can be precisely controlled), the outcomes for a given S value exhibit significant scatter rather than a unique N value. Consequently, experimental results are graphically presented as $\log(S)$ versus the mean of $\log(N)$. To address the uncertainty associated with this scatter, an S-N curve of $\log(S)$ versus the mean minus two standard deviations of $\log(N)$ is employed for design purposes. Numerous S–N curves, each tied to a specific definition of S and N as well as a particular structural detail, are available in the literature. In this thesis, S-N curves sourced from Det Norske Veritas (DNV), aligning with industry practice, will be utilised (DNV, 2021b).

All structural components, including welded connections, non-welded connections, attachments, structural discontinuities, and locations with stress concentrations, are potential sites for fatigue damage accumulation. Lower-bound screening assessments often precede detailed individual assessments of susceptible locations.

The discussed fatigue assessment pertains to the fatigue design of new structures, focusing on uncracked locations. The limitation arises because stress calculations do not capture the local stress situation at a crack, and S-N curves inadequately model fatigue crack growth. Assessing pre-existing cracks necessitates a fatigue crack growth evaluation using fracture mechanics methods.

In this context, uncracked refers to the absence of macroscopic cracks detectable by suitable inspection techniques. The proposed analysis assumes that structures at the end of their design service life do not harbor cracks of critical size.

Design service life is defined by ISO as the assumed period during which a structure is to be used for its intended purpose with anticipated maintenance, but without substantial repair being necessary (ISO, 2019). For a fixed offshore structure, such as monopiles, this is the period during which it is in place at its offshore location.

Fatigue damage is a phenomenon confined to specific areas; it originates at one or multiple adjacent locations within the structure and progresses from there. The method outlined in this section does not address the occurrence of progressive fatigue failures, which could ultimately result in the overall failure of the structure. Consequently, discussing the fatigue of a structure in a global context lacks meaning. As a result, the local conditions, including stress variations and the intricacies of construction and workmanship during fabrication, exert a profound influence on the extent of fatigue damage.

To ensure a dependable fatigue assessment, all these factors should be meticulously considered with utmost accuracy. Consequently, fatigue analysis typically necessitates more intricate models of both actions and the structure itself, along with significantly more refined analysis procedures compared to those employed in strength analysis.

2.3.1 Fatigue assessment

A fatigue assessment consists of four steps: stochastic environmental modeling, structural response calculation, establishing stress range distribution, and damage accumulation (Kühn, 2001). Various methods exist for each step, but two fundamental approaches are commonly employed:

- Time domain approach: This involves generating random time series from wind and wave spectra, conducting an unsteady system simulation through time step integration techniques, and rainflow counting of stress ranges.

- Frequency domain approach: This approach directly applies environmental spectra, utilizes linear spectral analysis, and determines stress range distribution from spectral moments.

While detailed insights into both approaches are omitted here, Kühn extensively discussed their pros and cons in 2001 as part of his doctoral thesis (Kühn, 2001). The present thesis predominantly adopts the time domain approach due to its straightforward setup, eliminating the need for linearisation of wave heights/drag loading, which inherently involves uncertainties and conservatism. The frequency domain analysis demands greater expertise for correct execution (frequency selection and wave linearisation) and requires thorough checking and validation.

Although this thesis primarily adopts a simplified fatigue assessment to evaluate various coefficient methods, a non-simplified fatigue assessment, compliant with the IEC-61400-3 standard at the time of writing, is expounded here in four steps. The purpose of elucidating this non-simplified fatigue assessment is to distinguish between the two methods: the one prescribed by the IEC and the one applied within this thesis, detailed in Chapter 5.

2.3.2 Stochastic environmental modelling

The initial step involves modeling environmental conditions, encompassing stochastic factors such as waves and wind. Focusing on the wave environment, a distinction is made between short-term and long-term conditions.

Short-term conditions denote a stationary state where the sea remains statistically constant, typically lasting for a standard period of 1 to 3 hours. This stationary state is referred to as a sea state, and it can be realistically described by a theoretical wave spectrum model.

Long-term conditions, by definition, characterize situations where the wave environment ceases to be stationary and undergoes changes. Consequently, long-term wave conditions are invariably composed of a series of successive sea states. Given the absence of theoretical models to depict the long-term wave climate, the characterization of long-term conditions at a specific location relies on empirical data. Typically, long-term conditions span the duration of a season, a year, or the design service life of a structure. In the context of a fatigue assessment for the in-place scenario, the long-term conditions during the design service life, or those representative of a typical year, are considered.

The wave scatter diagram emerges as the most fitting representation of the long-term wave environment at a specific location. Ideally, this diagram delineates the probability density function, $p(H_S, T_R, \theta_m)$, capturing the joint occurrence of the three principal parameters defining a sea state: significant wave height H_S, representative period T_R, and mean wave direction θ_m. A simplified wave scatter diagram excludes the mean wave direction by assuming omnidirectional values. An example can be found in the project thesis (Deursen, 2023). This omission can be driven by the desire to expedite wave calculations, as incorporating mean wave direction would entail a substantial computational burden. While this approach sacrifices directional wave scatter data, which offers a more precise representation of the environment, it enables a more efficient like-for-like comparison.

Following the characterization of the wave environment, other environmental conditions, specifically wind, are examined. Similar to waves, wind exhibits directional dependence, but for simplicity, omnidirectional wind speed values are utilised, as reasoned for waves. Explicit example values can

be found in the project thesis (Deursen, 2023). Wind speed typically spans from 0 [m/s] to above cut-out, where the cut-out represents the reference wind speed at which the wind turbine blades are pitched to regulate lift force, ensuring structural safety.

Combining omnidirectional values with the full range of wind speeds involves considering probabilities for both operation and idling. Notably, the consideration of operational modes in OWTs is crucial. Operational modes determine whether aerodynamic damping needs accounting for in the calculation of hydrodynamic response associated with winds between the cut-in and cut-out wind speed. Cut-in denotes the lowest 10-minute average wind speed at hub height, at which the wind turbine commences power production.

In principle, two scatter diagrams are required for the production wind speed range: one reflecting load case probabilities during actual production and another for failure and repair states (Kühn, 2001). Establishing such load case probabilities is a complex undertaking and is not addressed within this thesis.

Even when utilizing omnidirectional values for both wind and waves, a significant number of simulations are necessary to calculate fatigue loads. By employing simplified formulas derived from the frequency domain approach, additional methods for consolidating scatter diagrams and interpolating fatigue loads can be devised (Seidel, 2014). The consolidation of scatter diagrams yields a comprehensive set of representative Normal Sea States (NSS) for fatigue load scenarios. This consolidation involves a thorough examination to establish correlations between the probabilities of wind and wave conditions. This evaluation may be conducted on available metocean data through the following three distinct operations:

1. Establish a correlation between wind speed at hub height, U_w, and significant wave height, H_s.

2. Establish a correlation between significant wave height, H_s, and wave spectral peak period, T_p.

3. Assign probabilities to each wind speed, U_w, significant wave height, H_s, and wave spectral peak period, T_p, scenario.

2.3.3 Structural response calculation

After establishing stochastic environmental models, the subsequent step involves calculating the structural response of the system to these varying environmental conditions. Since the actions on the structure are inherently time-varying, the stress responses exhibit a corresponding time-varying nature. Monopiles, considered dynamically responding structures due to the significance of dynamic behavior, necessitates a dynamic analysis, as a quasi-static linear structural analysis proves insufficient. This dynamic analysis is typically carried out using simulation tools such as FAST or Bladed.

The analyses are conducted across a broad spectrum of wave heights and periods, with many of these values significantly lower and shorter than those considered in the design wave height and period for strength analysis. In fatigue analyses, the viscous drag force becomes less crucial than in strength analysis during extreme storm conditions. For fatigue analysis, the inertia term will always dominate over the drag term. Therefore, meticulous attention is given to the cross-sectional area and the associated choice of inertia coefficients.

For fatigue analyses of tubular members, an inertia coefficient of $C_m = 2.0$ is mandated by standard ISO19902 (ISO, 2020). The drag coefficient (C_d) remains applicable, as discussed in the project thesis (Deursen, 2023), aligning with standard ISO19902 section A.9.5.2.3.

In global structural analyses to determine member nominal stresses, a dynamic linear or non-linear analysis incorporating the steady-state dynamic response to periodic waves is essential. The impact of dynamic response on the long-term local stress range history is assessed through spectral analysis and a frequency domain dynamic solution.

The position of the platform's natural frequencies relative to the frequency of hydrodynamic forcing significantly influences the level of dynamic response. Given the potential variation in natural frequencies based on design assumptions, a careful review of theoretical natural frequencies is imperative.

2.3.4 Establishment of stress range distribution

Following the computation of structural responses to various environmental conditions, the third step involves establishing the stress range distribution. This phase revolves around extracting stress range values from the stress time history data generated by each simulation. Numerous methods can be employed for this purpose, but the most commonly used and standardized procedure is rainflow counting, introduced by Matsuishi and Endo in 1968. This method involves breaking down a cyclic stress-strain curve into individual stress cycles, each representing a complete stress reversal from maximum to minimum values. The procedure then counts or half-counts the number of cycles in each stress range bin to generate a histogram.

2.3.5 Damage accumulation

The long-term stress range history and the fatigue resistance both pertain to a specific location in the structure. In the final step, these two components are integrated using Palmgren-Miner's rule which is shown in Equation 22 (ISO, 2020). Palmgren-Miner's rule is a linear damage accumulation model employed to predict the fatigue life of a component based on the cumulative damage inflicted by cyclic loading (Kauzlarich, 1989). The rule operates on the assumption that the damage induced by each stress cycle is directly proportional to its magnitude and duration, and the cumulative damage can be calculated as a linear sum of the damage caused by individual cycles.

$$D_R = k_{LE} \cdot \gamma_{FD} \cdot \sum_i \frac{n_i}{N_i} \tag{22}$$

Where:

D_R is a non-dimensional number, the Palmgren-Miner's sum or damage ratio for a time T
k_{LE} is a local experience factor
γ_{FD} is a design fatigue factor
n_i is the number of cycles of stress range, S_i, occurring during time period, T
N_i is the number of cycles to failure under constant amplitude stress range, S_i, taken from the relevant S-N curve.

In the fatigue assessment procedure, fatigue failure is assumed to occur when $D_R = 1, 0$.

Equation 22 may be used to estimate fatigue life. If all damage is due to the same circumstances (e.g. in the in-place situation), the calculated fatigue life L may be calculated using Equation 23 (ISO, 2020).

$$L = T/D_R \tag{23}$$

Where:

L is the calculated fatigue life based on the calculated fatigue damage
T is the time period ($T \geq 1$ year) over which Palmgren-Miner's sum was determined
D_R is the calculated fatigue damage during time, T, according to Palmgren-Miner's sum.

2.4 Software

The design of an XXL monopile incorporates numerous analyses, including hydrodynamic and structural assessments. This thesis specifically focuses on the coefficients utilised in wave load calculations, as detailed in both Section 1.3 and Section 1.4. However, the research objective states the need to evaluate the influence of these coefficients on the fatigue life of an XXL monopile. This necessitates conducting all necessary analyses from site characterization to design assessment. To address this within the confines of a master's thesis, a decision was made to develop a Matlab script for the time-varying coefficient methodology, which could be integrated into MonoPoly. More on this implementation can be found in Section 3.6. MonoPoly, an in-house software package developed by Sea and Land Project Engineering (SLPE), is briefly introduced here. It is important to credit SLPE for the information regarding MonoPoly (SLPE, n.d.).

MonoPoly is crafted using .NET MAUI 8.0, showcasing a cross-platform architecture, enabling its utilization across diverse operating systems like Windows, macOS, and Android. It is finely tuned for parallel processing, integrating an Application Programming Interface (API) for programmatic manipulation and batch running, along with automated error-checking capabilities. Additionally, it offers separate applications for:

- Meshing

- Hydrodynamic analysis (Poseidon)

- Structural analysis (Athena)

- Superelement reduction (Damastes)

- Post-processing (Titan)

- Design (Proteus)

The meshing application is exclusively designed for optimizing monopiles within a Finite-Element-Analysis-based (FEA) design framework. It includes a proprietary in-house finite element mesher, numerical integration using Gauss quadrature, iterative eigenfrequency optimization employing root-finding algorithms, and convergence towards an optimal monopile solution for a specified WTG location.

Poseidon represents the cutting-edge wave analysis solver, boasting a speed exceeding 100 times that of Sesam Wajac, a software package provided by DNV (SLPE, n.d.). It excels in performing spectral analysis across various wave spectra types, including JONSWAP, Pierson-Moskowitz, Torsethaugen, and Ochi-Hubble. Furthermore, it integrates Airy wave theory and non-linear Stream wave theory, along with accommodating constrained non-linear waves. Additionally, Poseidon incorporates Morison wave loads from the evaluation of Reynold and Keulegan Carpenter numbers and incorporates the MacCamy-Fuchs modification for diffraction inclusion. Notably, it operates in a single-threaded mode, optimizing performance even on modest computing resources.

Athena stands as a meticulously optimized structural analysis solver, surpassing Sesam, an offshore structural engineering software, by over 100 times in speed (SLPE, n.d.). It proficiently conducts both static and dynamic analyses, accommodating linear as well as nonlinear analysis requirements. Furthermore, Athena is equipped to execute superelement structural analyses through static, dynamic, Component Mode Synthesis (CMS), and Iterated Improved Reduction System (IIRS) condensation techniques. Similar to Poseidon, Athena also operates in a single-threaded mode, ensuring efficient performance.

Titan, the post-processing application, incorporates ULS code checking according to the recommended practice DNV-RP-C202. This includes yield and stability checks, shell buckling assessment, and interaction checks for shell and column buckling. Additionally, it performs Fatigue Limit State (FLS) code checking as per the recommended practice DNV-RP-C203, involving a rainflow counting algorithm, S-N library utilization, automated Stress Concentration Factor (SCF) calculation, damage assessment for each load case, and accumulation of lifetime damage.

Proteus encompasses the post-processing of results produced by Titan, offering automated sizing for structural cans and cone sections. Furthermore, it incorporates a frequency softening/stiffening algorithm and facilitates the generation of production drawings alongside automated reporting capabilities.

3 Time-varying coefficient method

This chapter explores the time-varying coefficient method in depth, with the goal of providing a comprehensive description enabling replication for future research. In Figure 9, a flowchart illustrating the sequential steps of the method is presented. These steps are elaborated upon in the subsequent sections of this chapter. Additionally, the final section, Section 3.7, outlines the constant coefficient method, commonly employed in industry practice, for comparison purposes in the ensuing chapters.

The primary assumption made within this approach includes treating the body as rigid. Furthermore, the analysis made within this thesis neglects current effects and time-varying surface roughness. It employs a JONSWAP spectrum to characterize the wave spectrum. JONSWAP is suitable for both fully developed and evolving sea conditions. Despite the fact that the North Sea Wind Farm operates in an environment with high sea states, as indicated in Figure 20, the analysis assumes that second-order wave theory is adequate, omitting higher-order wave theories. This decision is justified by testing the method against a fatigue analysis focused on operational sea states rather than extreme conditions.

The decision was made to utilize the Keulegan-Carpenter number and the Reynolds number, hereafter referred to as K_c and R_e, aiming to encompass the majority of the variability in both the drag coefficient, C_d, and the inertia coefficient, C_m. A comprehensive definition and theoretical background regarding the Keulegan-Carpenter number can be found in Subsection 2.1.6.

The rationale behind selecting K_c and R_e over the other alternatives mentioned in Section 1.3 stems from the assumption of a non-time-varying surface roughness and a zero current velocity. Nonetheless, this does not preclude investigation into the other options in the future. It is acknowledged that surface roughness may vary with time, and there may be nonzero current velocities. However, to maintain focus and allow for in-depth exploration, these factors are presently excluded from consideration.
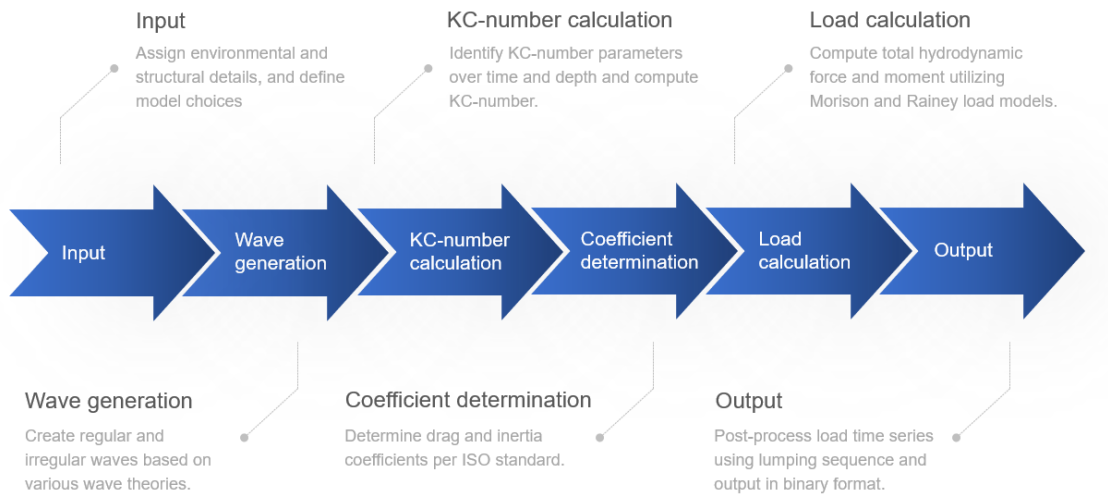

Figure 9: Flowchart time-varying coefficient method

3.1 Input time-varying model

As outlined in Section 2.4, the methodology involving time-varying coefficients will be integrated into MonoPoly. This implies that MonoPoly will handle the entire structural analysis sequence, except for the hydrodynamic analysis. Instead of utilizing Poseidon, the Matlab script for the time-varying coefficient methodology will be incorporated into this sequence. This necessitates a seamless exchange of information between the various applications.

To perform structural analysis in MonoPoly, the input consists of a text file containing crucial data like initial geometry, wave spectrum, water depth, and simulation parameters like time step size and total duration. This text file is also used within the hydrodynamic analysis to make sure identical input is used throughout the whole analysis. A straightforward Matlab code is employed to extract this input from the text file, parsing the information into structures usable within Matlab. This Matlab code was developed and provided by SLPE.

Furthermore, the code has been adapted to allow for specific model selections through the incorporation of toggles that can be activated or deactivated. This feature is particularly valuable for comparative studies aimed at evaluating the impact of various model choices. The toggles included are summed up below.

- Marine Growth: Toggle to incorporate or exclude marine growth in the monopile's geometry.

- Wave Type: Toggle between regular or irregular wave analysis.

- Wave Theory: Toggle to select between first-order wave theory or second-order Stokes' theory.

- Zero-Crossing Period: Toggle between zero-down or zero-up-crossing period calculation.

- Wave cycle Type: Toggle between full wave cycle or half wave cycle K_c number calculation.

- Wheeler Stretching: Toggle to enable or disable Wheeler stretching.

- Load Model: Toggle between Morison or Rainey load model.

- Debug Mode: Toggle to enable or disable run in debug mode.

3.2 Wave generation

To develop a versatile approach, both regular and irregular waves can be simulated using either first-order or second-order Stokes' wave theory. For a more in-depth description of these four different waves, reference is made to Section 2.1. It should be noted that the implementation of these waves within the method is per this section.

While the wave kinematics for regular waves can be straightforwardly calculated using the equations from Subsection 2.1.1 and Subsection 2.1.4, the determination of wave kinematics and free surface elevation for irregular waves relies on a code developed by Fuhrman. This code implements up to third-order, directionally-spread, irregular wave theory (Madsen and Fuhrman, 2012), incorporating corrections proposed by Fuhrman and co-authors, as detailed in the appendix of their work (Fuhrman et al., 2023). The methodology aligns with Subsection 2.1.2 and Subsection 2.1.5. Notably, the provided code can compute both free surface elevations and kinematics for irregular waves up to a desired order (1, 2, or 3), aiming to demonstrate the implementation of theory into a computational framework and to present associated results. This code has been adapted and integrated into the MATLAB script for the time-varying coefficients method.

In Figure 10 and Figure 11 the free surface elevation, η, is shown using linear wave theory and Stokes' second-order wave theory. The higher-order waves indicate typical behavior such as increased steepness, higher peaks, and shallower troughs.
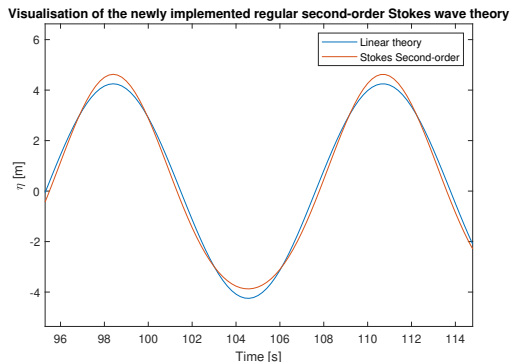
Figure 10: Generation of linear and second-order regular wave with $H = 8.5$ [m], $T = 12.3$ [s]
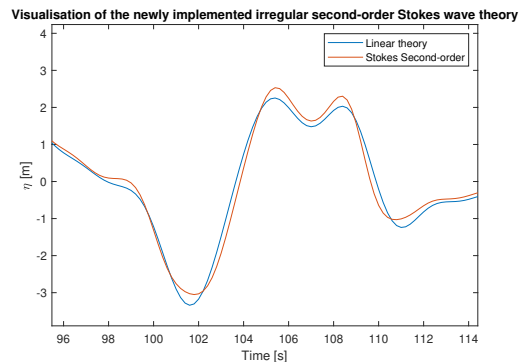
Figure 11: Generation of linear and second-order irregular wave with $H_s = 8.5$ [m], $T_p = 12.3$ [s]

The generation of the numerous wave components for irregular waves is mostly done via the equal-width approach. The method here utilizes the equal-area approach, also referred to as the equal-energy approach. This approach ensures that the energy content within each frequency band is equal. This means that the total energy across the spectrum is distributed evenly among the discrete frequency bins, resulting in a representation where each frequency interval carries the same amount of energy. For a more detailed description reference is made to Goda's work or more recently the work done by Baekkedal (Goda, 2010 and Baekkedal, 2014). A visualisation of the approach applied to the wave spectrum defined in the project thesis, is shown in Figure 12. The reason for using this approach over the equal-width one is to reduce the required number of wave components and therefore the computational effort whilst maintaining the total energy across the spectrum and ensuring that the frequency components with the highest energy contribution to the wave force are well represented. To ensure accuracy, a validation step is included to verify that the output of the sea state maintains a resemblance to the input parameters: significant wave height (H_s) and peak period (T_p). Additionally a cut-off frequency, $\omega_{max} = \sqrt{2g/H_s}$, is defined following recommended practise (DNV, 2021c).
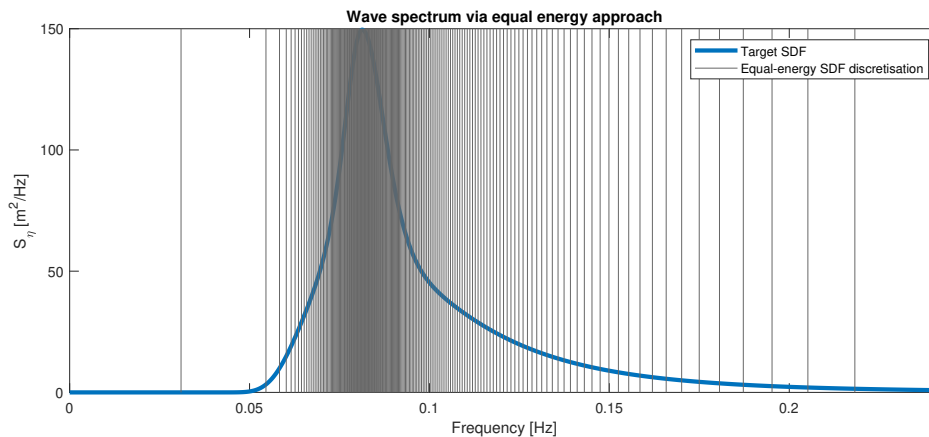
Figure 12: Equal-energy approach for discretization of JONSWAP wave spectrum with 200 wave components, $H_s = 8.5$ [m], $T_p = 12.3$ [s], Spectral Density Function (SDF)

3.3 KC-number calculation

Given that the K_c number is selected to accommodate the temporal variations in C_d and C_m, its calculation must consider changes over time. In the context of irregular waves, only two of the three terms in the K_c number definition exhibit time dependency. It is worth noting that for regular waves, none of the terms display temporal variation, rendering the time-varying coefficient

method identical to the constant one. Except for the case where second-order wave theory with half-wave cycle analysis is used due to the asymmetry around SWL. The first term pertains to the wave period, which can be determined through various approaches. However, in this thesis, it is specifically confined to the zero-up and zero-down-crossing periods. The zero-up-crossing period refers to the duration for a wave crest to traverse the mean water level (MWL) twice, oscillating from trough to crest and back to trough without intersecting the MWL line in an upward direction. Similarly but opposite, the zero-down-crossing period signifies the time taken for a wave trough to cross the MWL line twice, moving from trough to crest and back to trough without breaching the MWL line downward.

Although it is anticipated that no discrete differences should arise between the utilization of zero-up or zero-down crossings, especially with sufficiently long time series, a sensitivity analysis comparing the outcomes obtained from both methods is presented in Section 5.5.

The time-varying period is established through a function designed to detect zero-crossings within a given dataset. This function provides details about these crossings, such as the count of crossings and the positions of the zero-up or zero-down crossings. An example of a sea state, featuring indications of zero-up crossings identified through the function, is depicted in Figure 13. Between two consecutive zero-up or zero-down crossings, depending on the toggle, the period is computed as the time difference between these two instances. However, it is important to note that the initial and final segments of the time series are excluded from this calculation. This exclusion is due to the uncertainty regarding whether the surface elevation commences precisely at the MWL. As a result, it is assumed that the periods of the first and last segments of the time series are equivalent to those calculated for the subsequent segments. The first segment here is defined by the time from the start of the simulation till the first zero-up or zero-down crossing, depending on the toggle setting. The last is defined as the time between the last zero-up or zero-down crossing before the end of the simulation.

The second time-dependent factor encompasses the maximum horizontal velocity, commonly referred to as the extreme velocity resulting from the orbital motion of waves, encompassing both minimum and maximum values. When the wave cycle type toggle is set to full wave cycles, the extreme velocity is determined and recorded between two zero-up or zero-down crossings, as depicted in Figure 13. Conversely, if the wave toggle is set to half wave cycles, the extreme velocity is determined and recorded between two zero-crossings, irrespective of whether they are up or down-crossings, as illustrated in Figure 14. Although the period remains constant across the depth of the monopile, the extreme velocity exhibits variation. Consequently, the extreme velocity is stored across the depth, facilitating a two-dimensional ($2D$) K_c number, where $2D$ denotes the temporal and depth dimensions. Notably, since K_c is defined positively, the extreme velocity is considered in its absolute value, disregarding its direction. Similar to the assumption regarding the initial and final periods, the extreme horizontal velocity at the beginning and end is assumed to remain consistent with the first and last computed values.

Now that the period, T, the maximum velocity, U_m, and the diameter, D, are known, the K_c number can be calculated in time and along the depth.
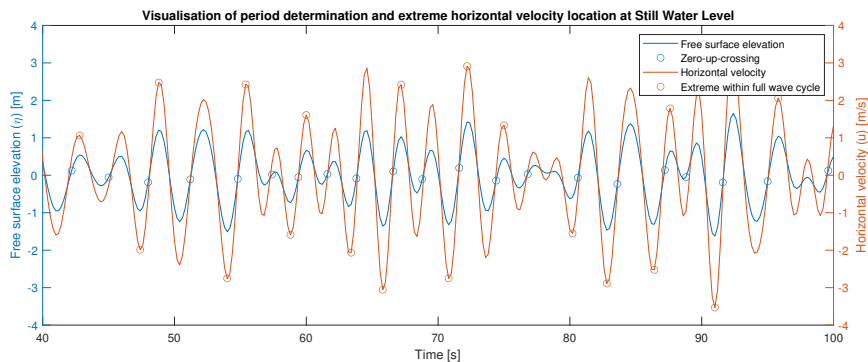
Figure 13: Interval taken from irregular sea state with $H_s = 2.9$ [m] and $T_p = 3.7$ [s] with identification of zero-up crossings and extreme horizontal velocity locations within full wave cycle
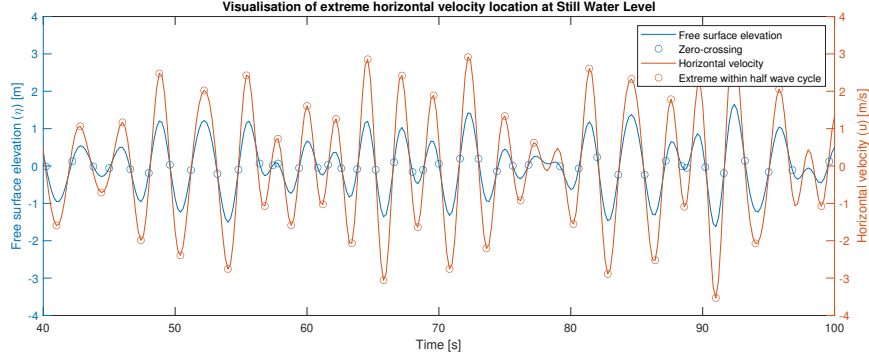
Figure 14: Interval taken from irregular sea state with $H_s = 2.9$ [m] and $T_p = 3.7$ [s] with identification of zero-crossings and extreme horizontal velocity locations within half wave cycle

3.4 Coefficient determination

Now that the K_c value is determined over time and across the depth, the computation of C_d and C_m is achieved using Figure 15 and Figure 16, resulting in two-dimensional C_d and C_m coefficients. Here, "two-dimensional" refers to the same dimensions utilised for the 2D K_c values.

It should be noted that here C_d has a Reynolds dependency since there exist different curves for different hydrodynamic drag coefficients for a steady flow, C_{ds}. To determine C_{ds}, Equation 24 and Figure 17 are utilised where $k/D = 450 \times 10^{-5}$ was taken due to the surface roughness of marine growth (SLPE, n.d.).

Additionally, given that it is not feasible for the load resulting from these coefficients to precisely mirror the abrupt variations of the K_c number, a moving average smoothing method was implemented. This method entails computing the mean value within a specified window size along the time series, effectively attenuating sudden changes and presenting a smoother representation of the data.

$$R_e = U_\infty D / \nu \tag{24}$$

Where:

U_∞	is the incident flow velocity, here taken as U_m which is calculated per wave period previously
D	is the diameter
ν	is the kinematic viscosity of water (1.2×10^{-6} [m^2/s])
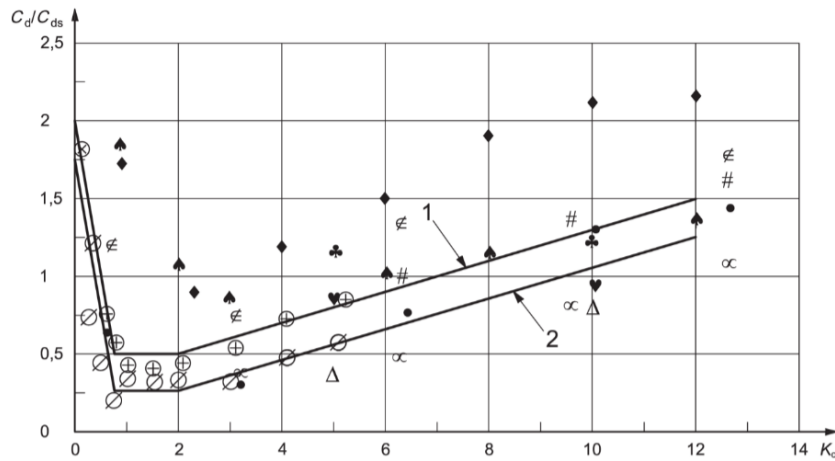
Figure 15: Wake amplification factor for drag coefficients as a function of K_c, curve 1 corresponds to $C_{ds} = 1.2$ and curve 2 corresponds to $C_{ds} = 0.6$, where C_{ds} is the hydrodynamic drag coefficient for a steady flow (ISO, 2020)
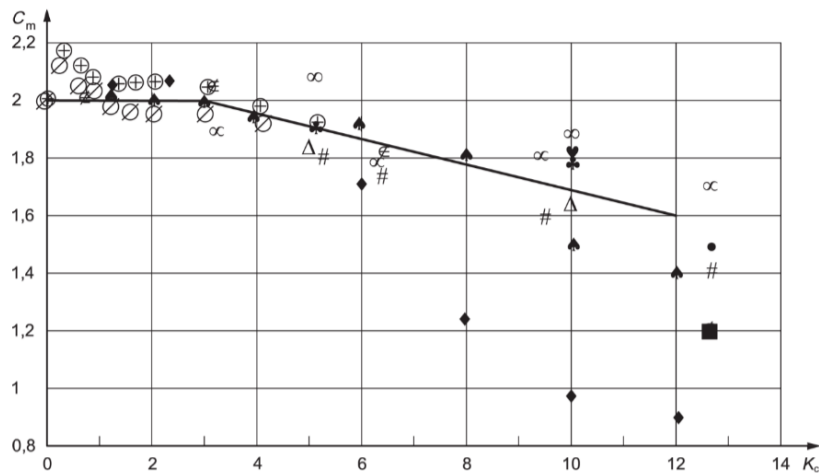
Figure 16: Inertia coefficient as function of K_c (ISO, 2020)
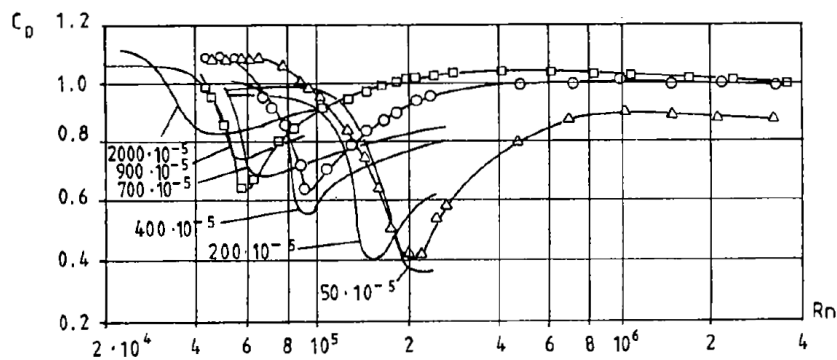
Figure 17: Drag coefficient, $C_D = C_{ds}$, of rough circular cylinders in steady incident flow for different surface roughness values k/D (k = average height of surface roughness, D = cylinder diameter, $Rn = R_e$.) Δ, $k/D = 110 \times 10^{-5}$, $\circ$, $k/D = 450 \times 10^{-5}$, $\square$, $k/D = 900 \times 10^{-5}$, ——, Fage and Warsap, 1929.

3.5 Load calculation

For the load calculation, three models have been identified: Morison, Rainey, and the Faltinsen, Newman, and Vinje (FNV) method. However, this thesis only considers the Morison and Rainey models. For a comprehensive understanding of these models, readers are directed to Subsection 2.1.7 and Subsection 2.1.8. This decision is based on the shared utilization of coefficients, specifically, the inertia and drag coefficients denoted as C_m and C_d respectively. Focusing on these two models allows for assessing whether the time-varying methodology has a more pronounced effect when using the Rainey load model compared to the Morison load model. Since the FNV method does not incorporate these coefficients, incorporating it would not contribute to this objective.

In fatigue analysis, it is common to generate low sea states to simulate typical wave conditions. These low sea states are characterized by short wave periods and consequently short wavelengths. This characteristic ensures that MacCamy and Fuchs diffraction theory, which becomes significant when the ratio of wavelength to diameter (λ/D) is less than or equal to 5, remains relevant.

Since the aim of this thesis is to investigate the effect of time-varying methods on Fatigue Limit State (FLS) analysis, MacCamy and Fuchs diffraction theory was integrated into the load calculation process. This integration involved creating an amplitude function, which is essentially half of the one indicated in Figure 8. The amplitude function utilizes the wavelength of the individual wave components to generate an amplitude factor. This factor is then multiplied by the acceleration of the specific wave component. The reason for this way of implementation is that it allows the C_m coefficient to be dependent on the wavelength and the K_c number. So this means that the original C_m value, which was determined using either the constant or time-varying coefficient method is not affected by the MacCamy and Fuchs correction. It should be noted that only the linear wave components are adjusted using this amplitude factor to stay consistent with MacCamy and Fuchs diffraction theory.

By employing MacCamy and Fuchs diffraction theory, it becomes evident that the nonlinear terms, denoted as F_A and F_I in the Rainy load model, remain unaffected, thus maintaining a long-wave approximation. To maintain consistency with Rainey's theory, the zero-crossing period was opted to serve as the criterion for assessing the validity of the long-wave approximation. Should this criterion not be met (i.e., $\lambda \leq 10D$), both terms are then rendered inactive.

Given that linear wave theory necessitates the integration of hydrodynamic force up to the SWL to stay consistent with the theory, the incorporation of Wheeler stretching, as detailed in Subsection 2.1.3, is facilitated through a toggle. This enables the use of wave kinematics in such a way that the velocity and acceleration, as per linear theory, are applicable at $y = 0$, extending all the way to the free surface and therefore the integration is no longer limited to SWL. Furthermore, this stretching technique facilitates the inclusion of higher-order responses, a pivotal consideration underscored in Section 1.2.

Finally, considering that assuming a uniform diameter is unrealistic for XXL monopiles, the introduction of a variable diameter along the depth is achieved by discretizing the monopile. This approach also allows for the incorporation of marine growth, albeit within the hydrodynamic model, wherein it is assumed to solely impact the geometry and roughness of the monopile, although in practice it can also affect the structure's weight. This assumption is not made in the structural response calculation in Athena however. Incorporating a variable diameter along the depth poses a challenge.

By employing Wheeler stretching, the discretization of the monopile along its depth undergoes temporal variations. Consequently, within a single period delineated by a zero-crossing, the calculation of the K_c number is required for all time steps. This necessity arises because the diameter, which directly influences the K_c number calculation, may vary along the depth. Assuming a reduction in monopile diameter towards the SWL, the K_c number could be underestimated when the free surface elevation is below the SWL and overestimated when it is above the SWL. To mitigate this issue, it was assumed that this effect is balanced out over the duration of a sea state. Consequently, the K_c number is computed only once or twice per period, depending on half or full wave cycle analysis, thereby reducing the computational time for the overall calculation.

3.6 Output time-varying model

The script for the time-varying coefficient methodology generates a time series for the total force and overturning moment. This configuration of the result is chosen to facilitate the validation process. The validation process is detailed further in Section 4.2. The experimental measurements, as described in Section 4.1, also provide time series data for the total force and overturning moment.

However, Monopoly requires a time series of member end forces. To address this, a lumping sequence is added as a post-processing feature to convert the total output to member end forces. This sequence ensures that distributed forces and point loads are appropriately allocated to corresponding members, enabling further analysis within MonoPoly while maintaining a total load virtually identical to the original.

Furthermore, Monopoly utilizes a binary-serialized array of single-precision floating-point values for input. Consequently, the previously mentioned post-processing feature also produces this file format. Using binary files for data transfer offers advantages in terms of efficiency and speed due to their compact representation and direct serialization of data, facilitating faster reading and writing operations compared to text-based formats. Additionally, binary files ensure data integrity and compatibility across different platforms and programming languages, providing a reliable and versatile solution for exchanging complex data structures between disparate systems.

Given that binary files are not easily interpreted through methods like inspection via a text file, a debug toggle was incorporated. When the debug mode is activated, alongside the binary file, a CSV file is generated. This CSV file facilitates straightforward examination of the executed run, proving particularly useful for subsequent analyses, as exemplified in Section 5.5.

3.7 Constant coefficient method

To facilitate a comparison between the time-varying coefficient method and the constant method, the latter has also been integrated. Ensuring a like-for-like comparison between the two approaches, all procedures outlined in the preceding sections have been replicated for the constant method. The sole discrepancy lies in the treatment of the period and extreme horizontal velocity. In the constant method, these parameters are no longer represented as time series. Instead, the period is determined as the mean zero-up or zero-down-crossing period, while the extreme horizontal velocity is calculated as the root mean square along the depth. Consequently, the period is now a scalar and the extreme velocity is now one-dimensional, aligning with industry practice. It is important to note that this constant method can be regarded as an advanced version of the constant method outlined by ISO and summarized in Section 1.3.

4 Experimental validation

This chapter presents the experimental validation of both the time-varying and constant-coefficient methods. Validation here entails confirming the accuracy of these models by attempting to replicate experimental results. The aim is to determine whether the validity of these models can be established. The chapter is structured into four sections. The first section outlines the experiment utilised. The second section details the extraction and processing of measurement data. The third section elucidates the alignment of experimental data with model data to reproduce outcomes. Lastly, the fourth section provides the results and discussion.

4.1 Experiment description

Many experiments have been conducted in the past to validate both theoretical and numerical methodologies. These experiments can be categorized into two groups: the first includes experiments suitable for the linear implementation of varying coefficients, and the second comprises those applicable to the higher-order implementation of such coefficients. Given the easier accessibility of experiments for higher-order implementation and the necessity to explore more extreme sea states, the choice was made to proceed with the higher-order implementation experiments (Deursen, 2023).

Initially, the experiment conducted by E. Bachynski and colleagues seemed the most promising. However, upon requesting the experiment data, it was discovered to be classified. In collaboration with E. Bachynski, the decision is made to utilize the experiments done by M. Thys, F. H. Dadmarzi, and E. Bachynski for the project WAS-XL for validating the time-varying coefficient methodology (Thys et al., 2019b). WAS XL (Wave loads and soil support for extra large monopiles) is a KPN project funded by the Research Council of Norway. This experiment is summarized in this section.

The WAS-XL project included three distinct phases of model testing. This thesis focuses on the second phase model tests, of which the aim was to measure wave load and wave response on a monopile.

In June 2019, the model tests took place at NTNU's small towing tank. Scaled at 1:50, with a water depth of 27 meters, three distinct models were constructed, all adhering to the WAS-XL base case parameters, featuring a 9-meter monopile diameter. For all base case parameters, reference is made to Subsection 4.2.1. The first model, a single-pipe structure, was rigid and employed solely for global wave load measurements. The second model, also rigid but segmented, served to gauge both global and local wave loads. Finally, the third model was flexible, designed specifically to assess the monopile's response to wave-loading.

Wave loads were previously assessed in phase 1 of the WAS-XL model tests; however, in this phase, they were re-evaluated without surface roughness on the model and with enhanced instrumentation for local wave load measurement. While a segmented model was utilised in the initial phase of the tests (Thys et al., 2019a), water intrusion affected the accuracy of measurements. To address this issue, a waterproof membrane was incorporated around the model for this phase, effectively mitigating water intrusion but introducing measurement uncertainties. Thus, further analysis of results obtained with the segmented model is considered imperative. At present, utilizing these outcomes is therefore not advised.

In Chapter 3, the assumption of a rigid body was adopted. Consequently, the first model is utilised in the validation process, which is further detailed in Section 4.2. Various regular and irregular waves were subjected to testing on the first model. Specifically, the regular waves spanned a wide spectrum of wave steepness and periods, with the incorporation of second-order correction to the wavemaker motion:

- 22 wave periods between 6 [s] and 16.5 [s] with a 0.5 [s] step size

- Steepness: 1/20, 1/22, 1/25, 1/30 and 1/40

The irregular waves for testing were sea states 2, 4, and 5, which were originally employed in phase 1 of the project. Second-order wavemaker correction was not implemented for irregular waves due to technical limitations.

- Sea state 2: $H_s = 8.6$, $T_p = 11$ and $\gamma = 4.2$

- Sea state 4: $H_s = 9.0$, $T_p = 12.5$ and $\gamma = 2.6$

- Sea state 5: $H_s = 6.8$, $T_p = 13.2$ and $\gamma = 1.0$

4.2   Extract and process measurement data

The aim of the validation is not to make an experimental analysis, there are simply too many variables such as the experimental setup that could affect the measurements. Unfortunately, this is also not covered by the report which presents the experiments. Going into all of these variables would overshoot the aim of this thesis. In this section, a description is given of what is done to extract and process measurement data for the validation of both the time-varying and constant methods using the experiments.

In Figure 18, a flowchart illustrating the sequential steps of extracting and processing measurement data from the experiments is presented. These steps are elaborated upon in the subsequent subsections of this section. It should be noted that both regular and irregular waves have been used for the validation, however, the steps for these two waves are different. There where explicit differences are present this will be explicitly mentioned.

Parameters

Establish parameters that define the experiment such as water depth and diameter.

Alignment

Align experiments with and without the model present in the wave tank.

Time series

Select a relevant interval for validation by time series.

Parameters → Scaling → Alignment → Uncertainty → Time series → Spectrum

Scaling

Scale measurement data for full-scale data.

Uncertainty

Determine uncertainty range for measurement data.

Spectrum

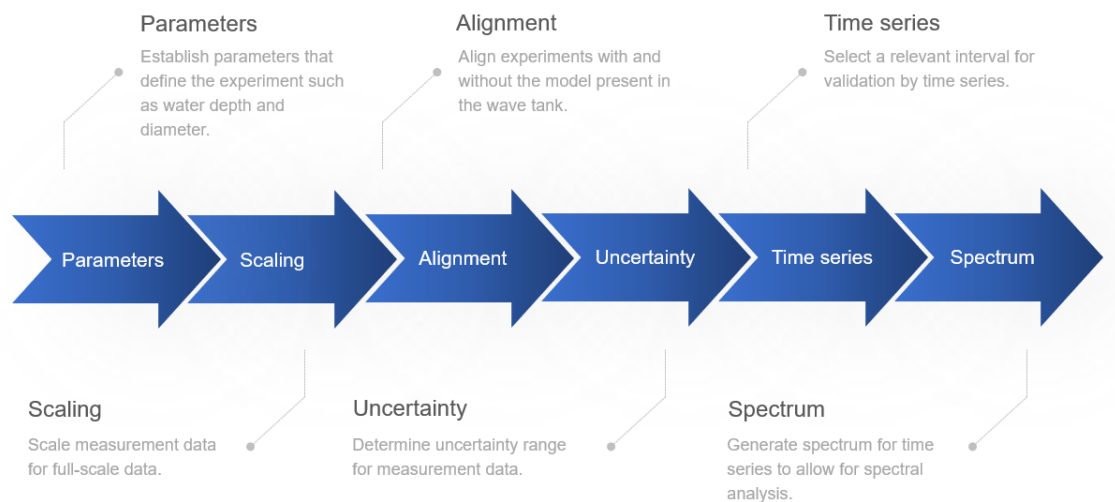Generate spectrum for time series to allow for spectral analysis.

Figure 18: Flowchart extracting and processing measurement data for validation

4.2.1 Parameters

The base parameters for the experiments are summarized in Table 2. The same parameters are used for input of the model such that a like-for-like comparison is possible.

Parameters	Value
Water depth (h) [m]	27
Water density (ρ) [kg/m^3]	1026.5
Diameter (D) [m]	9 (uniform)
Scale [-]	50
Sampling frequency [Hz]	$200/\sqrt{50}$

Table 2: Base parameter values given at full scale

4.2.2 Scaling

In the experiment, Froude scaling with a factor of 50 was selected. This ensures that the measurement data has to be scaled in order to interpret it at full scale. The scaling factors used for this are given in Table 3.

Parameter	Scaling factor	Model unit	Numerical factor	Full-scale unit
Length	λ	m	50.00	m
Velocity	$\sqrt{\lambda}$	m/s	7.07	m/s
Acceleration	1	m/s^2	1.00	m/s^2
Angles	1	deg	1.00	deg
Forces	1.025 λ^3	N	128.13	kN
Moments	1.025 λ^4	Nm	6406.25	kNm
Time	$\sqrt{\lambda}$	s	7.07	s

Table 3: Froude scaling factors from model to full-scale (Thys et al., 2019b)

4.2.3 Alignment

During the experiments, measurements were taken both with and without the model present in the wave tank. This refers to the 4 and 8 thousand test number series respectively. Since the model can disturb the surface elevation whereas if there is no model present this cannot occur, the measurements of the surface elevation were taken from the tests where there was no model present. The forces and moments were taken when there was a model present, obviously. This creates the necessity to align the two tests in time since the measurement data collection was not started at the same time. The alignment of the two tests was done by alignment of the flap position, which is the position of the wavemaker, which was possible since the input signals of both tests were identical. In Table 4 an overview is given of which tests were combined to extract all measurement data for an aligned time series.

	Test no. with model	Test no. without model
Sea state 2	4050	8051
Sea state 4	4150	8150
Sea state 5	4200	8200
Regular waves	4901	8900

Table 4: Test no. combination overview for alignment

4.2.4 Uncertainty

At the start of this section, it is already mentioned that it is not the aim of this thesis to do an experimental analysis. However, it is unfair to say that there is no uncertainty in the measurement data. Instead of analyzing the experimental setup, an uncertainty range was established by utilizing the fact that multiple tests were done for several runs. Basically repeating the tests for a number of runs. The number of runs differs for the different tests, however, all tests have been run at least five times. What was done to come up with the uncertainty range, which does not originate from the experiment report, is the following. It should be noted that this procedure was done for all different tests, referring to different sea states and the regular wave test. In addition, it is evident that an experimental setup analysis would provide more reliable results for establishing an uncertainty range. However, conducting such an analysis would require a significant amount of costly time, which could detract from other tasks. So the uncertainty established here should be interpreted as an indication that the experimental data is not 100% accurate.

1. Take out five time series for surface elevation, total hydrodynamic force, and overturning moment which all represent the same test but different runs.

2. Synchronize these time series in time such that they can be compared.

3. Establish all combinations of signals and store the difference as a separate time series [2].

4. Calculate the standard deviation of the difference signal.

5. This standard deviation is taken as the uncertainty of the test.

In Table 5, the uncertainties for all irregular wave tests are presented along with the uncertainty for the regular waves test. In addition to the full-scale quantities, the relative quantities are also presented. These should be interpreted as the portions of the mean amplitudes of the considered quantities.

Signal	Sea state 2		Sea state 3		Sea state 5		Regular waves	
	Full-scale	Relative [%]	Full-scale	Relative [%]	Full-scale	Relative [%]	Full-scale	Relative [%]
Surface elevation [m]	0.23	13.08	0.25	13.59	0.14	9.79	0.17	5.66
Total hydrodynamic force [N]	1.56×10^5	9.29	1.45×10^5	8.90	0.85×10^5	6.44	1.10×10^5	4.00
Overturning moment [Nm]	7.78×10^6	9.24	7.24×10^6	8.84	4.23×10^6	6.41	2.40×10^6	5.39

Table 5: Uncertainty for different tests regarding surface elevation, total hydrodynamic force, and overturning moment

4.2.5 Data extraction intervals

For generating regular waves, the wavemaker followed a sequence comprising 5 periods of ramp-up, followed by 50 periods, and then 5 periods of ramp-down, with an additional waiting period of 2121 seconds before the initiation of a new regular wave cycle. In the case of irregular waves, the wavemaker was controlled with a ramp-up spanning $10T_p$, followed by a 3-hour segment, and concluded with a sigmoidal ramp-down over $10T_p$.

The irregular tests ran for an effective duration of 9739 seconds in full scale, approximately equal to 2 hours and 42 minutes. In subsequent analyses of regular wave data, intervals during ramp-up or ramp-down periods are excluded. Conversely, for irregular wave data, all intervals are confined within the 9739-second period to mitigate any transient behaviors that could impact the results.

In Section 4.4, various time series are depicted from these intervals. To maintain clarity, a time interval of 200 seconds was selected for irregular waves and 2 periods for regular waves. However, it is acknowledged that a 200-second interval may be relatively short for characterizing a sea state. Consequently, spectral analysis, as described in the following subsection, is not based on the 200-second interval; instead, a minimum of 800 seconds of measured data is utilised.

---

[2]Note: The resulting uncertainty is sensitive to the synchronization used for this step. When small shifts are made in this process the uncertainty increases incorrectly. To mitigate this, the synchronization was done manually.

4.2.6 Spectrum

Since it can be difficult to assess an irregular wave in time, a spectral analysis was also incorporated. The spectrum coming from the time series signal is established using two different techniques. The first one is based on the Fast Fourier Transform (FFT) method, which transforms the signal into the frequency domain, providing insights into its frequency content, phase, and distribution. And the second one is established via Welch's power spectral density estimate with windowing built-in function in Matlab. In this function, the signal is divided into segments, each of which is multiplied by a Hann window function to reduce spectral leakage. The Fourier transform is then applied to each windowed segment, and the resulting spectra are averaged to estimate the power spectral density, providing a smoothed representation of the signal's frequency content. The reason for including these two techniques lies in the fact that the first one shows an accurate spectrum of the input signal which is needed for reproducing the experimental data for surface elevation which is further elaborated in Section 4.3 but it is rather difficult to interpret in terms of comparisons because of its great detail. This is where the second technique comes into play, because of the smoothing it is much easier to visually compare different spectra.

In order to check the reliability of the smooth power spectral density, a test was done. This test included the generation of a time series for the surface elevation using a theoretical spectrum. Since this ensures that the spectrum of the signal is known, it can be compared with the smooth power spectral density coming from the second function. Results of this test are presented in Figure 19. It is clear that the smooth power spectral density coming from the second function matches the theoretical spectrum which is used for input reasonably well and can therefore be used in subsequent sections for visual comparison.
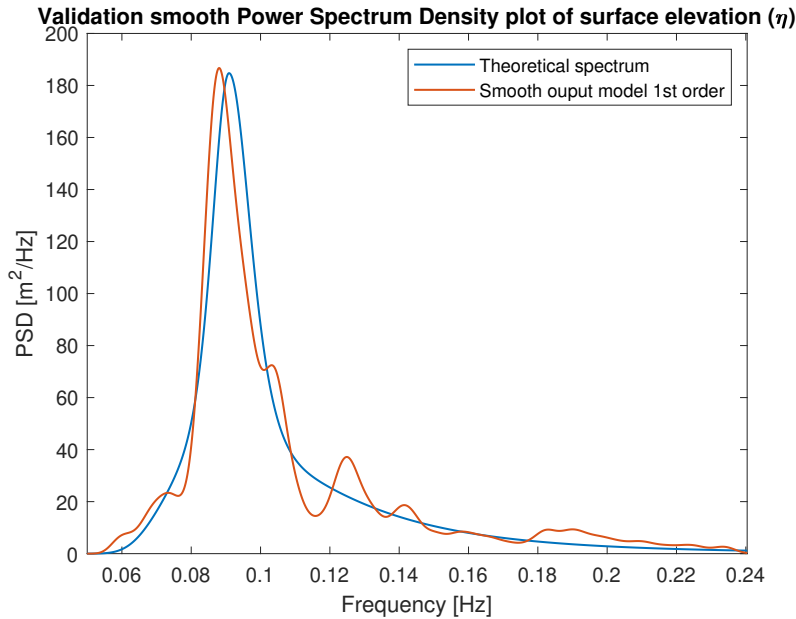

Figure 19: Theoretical and smooth Power Spectrum Density (PSD) plot for $H_s = 8.6$ [m], $T_p = 11.0$ [s] and $\gamma = 4.2$

4.3 Generation aligned model data

In order to validate the two methods the input of the model, which refers to the two methods, should match the experiments. However, since the model is not set up to mimic a wave tank the input parameters do not match. Even though both use a spectrum as input for the wave generation, the random parts of irregular waves, such as the phases and frequencies of the sea state were not shared in the report that describes the experiments. Therefore it was chosen to align the experiments with the model via an FFT of the surface elevation.

The FFT method that was used for this was the detailed one described in the previous subsection. The frequency content, phase distribution, and amplitude coming from the FFT of the experimental surface elevation signal were used as input for the model. In Figure 24 it can be seen that via this method the model generates a similar surface elevation. Now that the frequency content, phase distribution, and amplitudes are known the model is able to calculate forces and moments. It is now possible to validate the forces coming from the model with the experiments since the surface elevation is virtually the same. The results are shown in Section 4.4.

4.4 Results and discussion

In this section, the experimental data is presented together with the model data for a like-for-like comparison. It also includes a discussion of the results that are presented. Not all waves from the experiments are incorporated since this would take away the possibility to check details. The waves that have been incorporated are:

- Regular wave with $T = 6.5$ [s] and steepness 1/20, 1/25, 1/30 and 1/40.

- Regular wave with $T = 11.5$ [s] and steepness 1/20, 1/25, 1/30 and 1/40.

- Irregular wave with $H = 8.6$ [m], $T = 11.0$ [s] and $\gamma = 4.2$.

- Irregular wave with $H = 9.0$ [m], $T = 12.5$ [s] and $\gamma = 2.6$.

- Irregular wave with $H = 6.8$ [m], $T = 13.2$ [s] and $\gamma = 1.0$.

These tests are also illustrated in Figure 20, where the applicability ranges of various wave theories are indicated together with the reference project, the North Sea Wind Farm (Deursen, 2023). Notably, the conditions during the experiments match the one of the North Sea Wind Farm reasonably well. However, since this plot was originally devised for regular waves, directly fitting sea states with irregular waves poses a challenge. This challenge was overcome by utilizing the relationship between the peak period, T_p, significant wave height, H_s, and the zero-up-crossing period, T_z, for North Sea sites (DNV, 2021c). This relationship is given by Equation 25 and Equation 26. In summary, since H_s and T_p are known, T_z can be calculated. This zero-crossing period and the significant wave height are then used for the period and wave height in Figure 20. It should be noted that this is physically not substantiated and therefore only for indicative purposes.

Additionally, it should be noted that only relevant figures are shown in subsequent subsections. Due to the several different experimental waves that have been incorporated into the validation a lot of figures have been generated. However, only the ones that are relevant to support statements and conclusions are shown in this section. For all figures, reference is made to Appendix A.
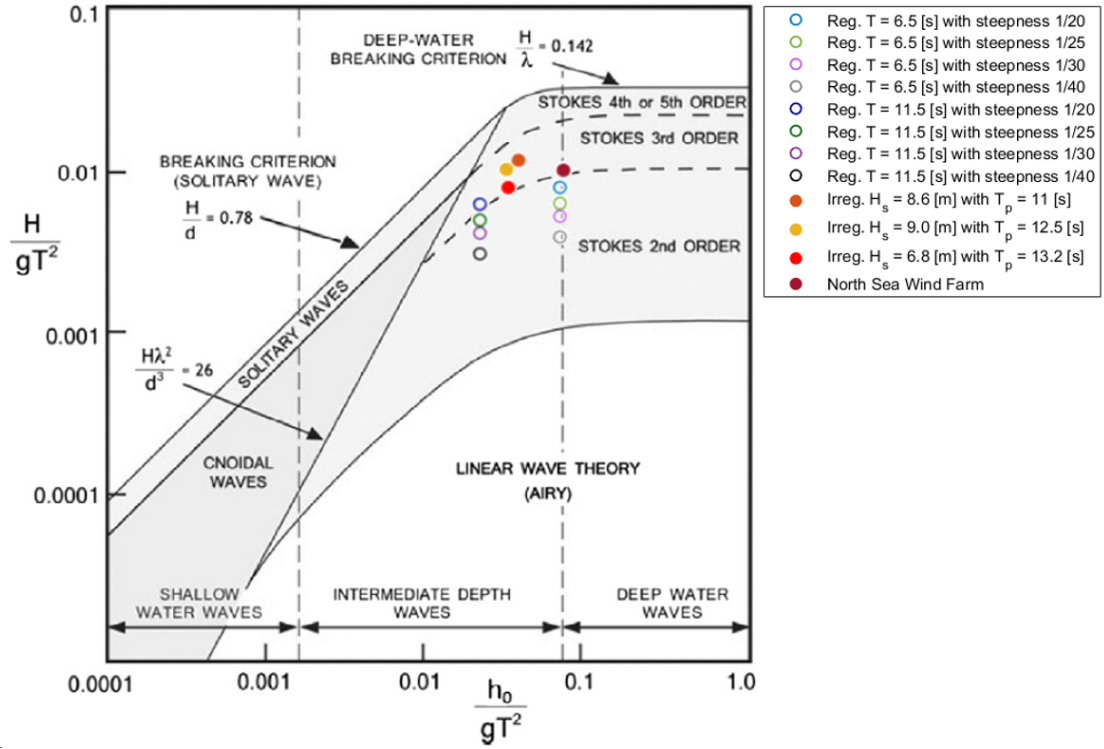
Figure 20: Regular and irregular experimental waves indicatively plotted on applicability ranges of various waves (LeMéhauté, 1976)

$$\frac{T_z}{T_p} = 0.6673 + 0.05037\gamma - 0.006230\gamma^2 + 0.0003341\gamma^3 \tag{25}$$

$$\gamma = \begin{cases} 5, & T_p/\sqrt{H_s} \leq 3.6 \\ \exp\left(5.75 - 1.15\frac{T_p}{\sqrt{H_s}}\right), & 3.6 < T_p/\sqrt{H_s} < 5 \\ 1, & 5 \leq T_p/\sqrt{H_s} \end{cases} \tag{26}$$

4.4.1 Regular wave

In Figure 21 the surface elevation, total hydrodynamic force, and overturning moment are shown for the time-varying coefficient method model and the regular wave experiment with $T = 11.5$ [s] and steepness = 1/40, which is equal to $H = 4.04$ [m].
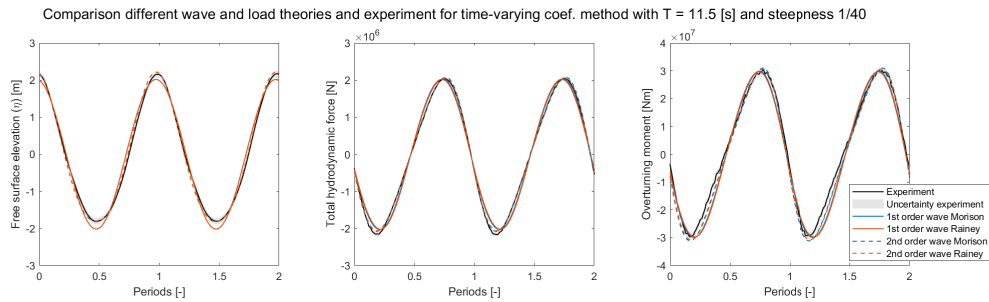

Figure 21: Experimental data and time-varying coefficient model data for $T = 11.5$ [s] and steepness = 1/40

What can be seen from this figure is that the model is able to reproduce the experimental data really closely. Where the first-order wave theory model misses the surface elevation slightly, the second-order wave theory model matches the experimental data almost perfectly, and similarly for the total hydrodynamic force and overturning moment.

One should note that the results shown here are for the least steep wave from testing. For the steeper waves, for example, the one shown in Figure 22, the results match less good which can be explained by Figure 20. Here it can be seen that the steeper the wave, the closer it gets to the end of the applicability range of second-order wave theory. Some of the cases are not even in the applicability range of second-order.
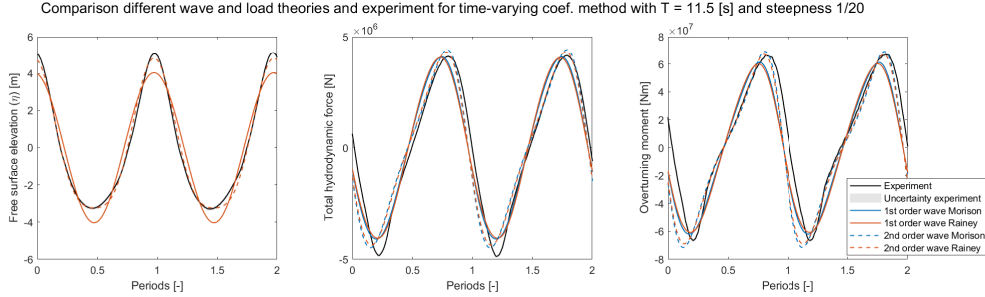

Figure 22: Experimental data and time-varying coefficient model data for $T = 11.5$ [s] and steepness $= 1/20$

A spectral analysis of all considered experimental waves was done to be able to support the statement about the decreasing accuracy of the model for steeper waves. In Figure 23 the spectra of the waves with different steepness and a period of 11.5 [s] are presented. It is evident that there is a clear trend: the steeper the wave, the more nonlinear spectral energy is present at two times and three times the wave frequency, which is not captured by second-order wave theory. It should be noted that this conclusion is not affected by the use of the 11.5 [s] wave compared to the 6.5 [s] wave. The spectral analysis for the 6.5 [s] can be found in Figure 69 in Appendix A.
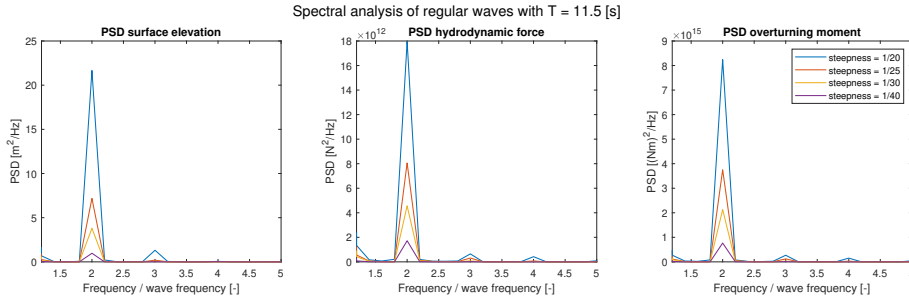

Figure 23: Spectral analysis experimental waves with $T = 11.5$ [s]

Until this point, the validation process has exclusively incorporated the time-varying coefficient method model. A parallel approach could be devised for the constant method. Yet, as clarified in Section 3.3, in the context of regular waves, both the time-varying and constant-coefficient methods yield identical results, owing to the absence of temporal variation in the terms defining the K_c number. Consequently, a decision was made to skip an extensive validation for the constant coefficient method.

4.4.2 Irregular wave

In Figure 24 the surface elevation, total hydrodynamic force, and overturning moment are shown for the time-varying coefficient method model and the experiment with test numbers 4050 and 8051.
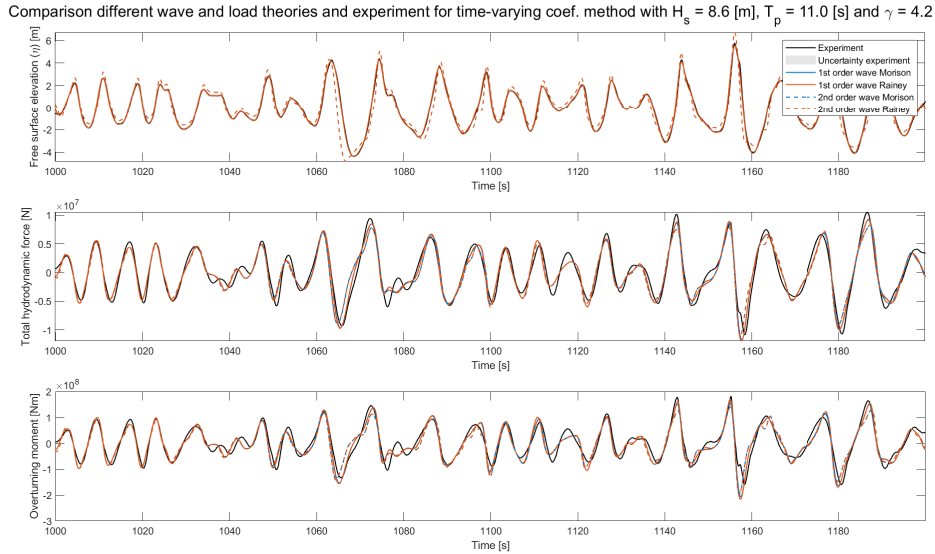

Figure 24: Experimental data and time-varying coefficient model data for $H_s = 8.6$ [m], $T_p = 11.0$ [s] and $\gamma = 4.2$

Starting with the surface elevation, it can be seen that there is no difference in the surface elevation for the Morison and Rainey load model for first-order wave theory. And similarly for second-order wave theory. This makes sense because the load models do not influence the surface elevation, they only affect the load calculation.

It can also be seen that the first-order wave theory model matches the experimental data better than the second-order wave theory model, which seems odd at first. One would expect that the second-order wave theory model should match the experimental data better due to the fact that it can model the surface elevation up to the second order.

After investigating this unexpected result, it was assumed that the explanation of this lies in the fact that the experimental signal was linearized by the FFT method used to reproduce the surface elevation. In this context, linearized means that decomposing the surface elevation using FFT masks the nonlinear interaction effects present in the surface elevation. The FFT process treats all wave components equally, making it impossible to distinguish between linear and nonlinear interaction effects. In order to check this hypothesis a test was run. This test included plotting the spectra of all three signals, the surface elevation of the first-order model, the second-order model, and the experiment. The resulting plots are shown in Figure 25 and Figure 26. These plots confirm the hypothesis because of the following. Using the FFT method, the experimental signal for surface elevation becomes linearized, as described earlier. This works well within the first-order model. However, the second-order model requires only the linear waves as input into the model, because from this, second-order waves and therefore energy is created. However, if all waves are given as input, as well as the non-linear waves, then the resulting signal and spectrum of this signal will have more energy than the original one. In Figure 26 and Table 6 it can be seen that the total power indeed increases with the second-order model, thus confirming the hypothesis. Additionally in Figure 26 it can be seen that sum and difference frequency effects create an overestimation of the spectral energy compared to the original and first-order model spectrum.

One way to solve this issue would be to only take out the linear waves from the experiment to use as input for the second-order model. This is however extremely difficult. One way to

work around it would be to introduce an iterative way of introducing a new cut-in and cut-out frequency for both the first-order and second-order model until the second-order model matches the experimental data better than the first-order one. In this way, an attempt is made to define a range of input frequencies that only cover the linear wave components. This will increase the accuracy of reproducing the surface elevation from the experiments with the second-order model and decrease the accuracy of the first-order model. It will however be impossible to only extract the linear wave components, so this iterative method can be seen as an error minimizer.

For the aim of this thesis, it seems unnecessary to establish such an iterative method. The reason for this is that it will increase the accuracy of the experimental validation however it will not affect the fatigue assessment due to the fact that this will depend on theoretical spectra instead of full-scale experiments. Using these theoretical spectra only the linear wave components are covered by definition and therefore this issue is bypassed.
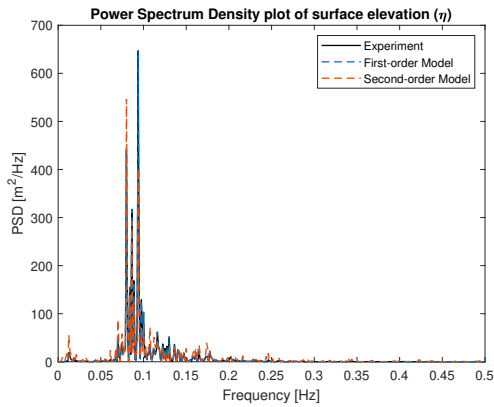

Figure 25: Power Spectrum Density plots for surface elevation (η) coming from first-order model, second-order model and experiment
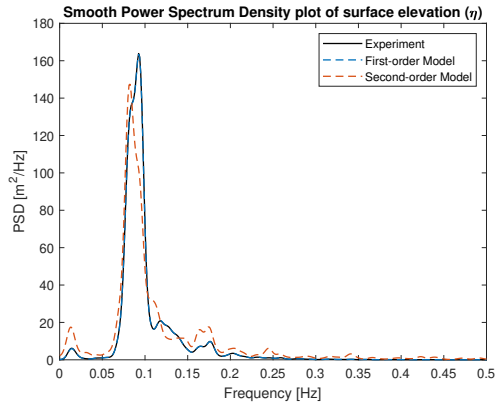

Figure 26: Smooth Power Spectrum Density plots for surface elevation (η) coming from first-order model, second-order model, and experiment

	Total power first-order $[m^2]$	Total power second-order $[m^2]$	Total power experiment $[m^2]$
Rough	4.4809	5.0510	4.4888
Smooth	4.8045	5.4523	4.8126

Table 6: Total power of first-order model, second-order model, and experiment corresponding to both detailed and smooth spectra

Moving on to the forces and moments, here we can see a bigger difference between the experiments and the models. Following the observation about the first-order model surface elevation also the forces and moments for the first-order model match visually reasonably well with the experiments, however not as close as the surface elevation. The second-order model shows quite some differences which can directly be related to the mismatch in the spectrum of the surface elevation. Especially the higher frequency wave components which are generated due to the second-order model cause bigger differences between the model and the experiment as can be seen by the high-frequency disturbances.

In the experiment data, there seems to be some nonlinear behavior, for example at 1157 seconds where a higher frequency component seems to affect the trough of the overturning moment signal. This led to the test whose aim was to see whether the spectral energy for the surface elevation, total hydrodynamic force, and overturning moment was equally distributed. The normalized results of this test are shown in Figure 27 and Figure 28. This clearly indicates a difference in spectral energy distribution between the surface elevation, forces, and moments. This conclusion questioned whether there were nonlinearities in the wave tank that were not captured by the FFT method used to reproduce the surface elevation. An additional test for this was conducted. This test

included plotting the spectrum of the surface elevation at different locations in the wave tank. If the spectrum was to change with respect to location in the wave tank then it could be concluded that nonlinearities were developing in the wave tank resulting in the nonlinear behavior of the forces and moments. The results of this test are presented in Figure 29, Figure 30, and Table 7. The results do not confirm the development of nonlinear behavior in the tank since the spectra are very similar for the 5 locations in the wave tank.
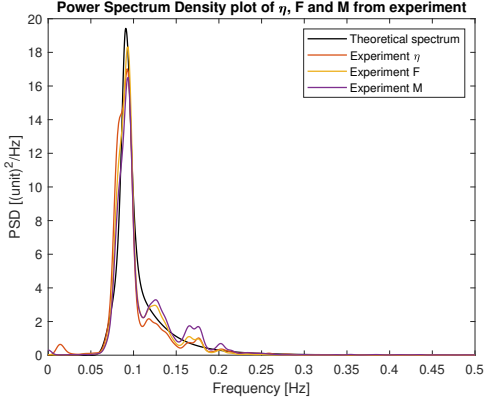

Figure 27: Normalized Power Spectrum Density plot for surface elevation (η) , total hydrodynamic force (F) , and overturning moment (M)
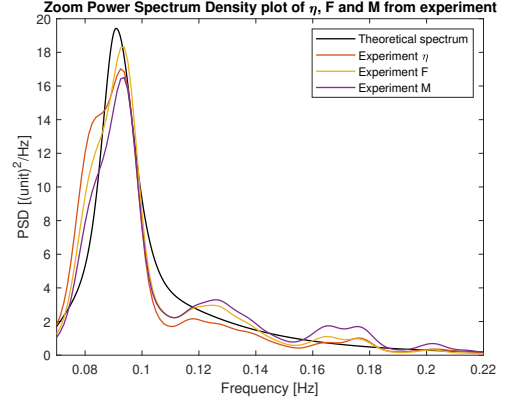

Figure 28: Zoom normalized Power Spectrum Density plot for surface elevation (η) , total hydrodynamic force (F) , and overturning moment (M)
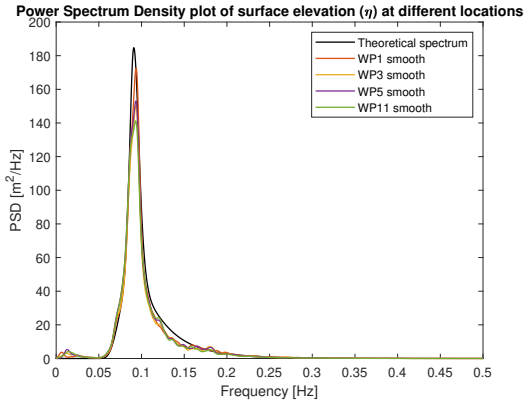

Figure 29: Power Spectrum Density plot of surface elevation (η) at different locations in the wave tank (WP = Wave Probe)
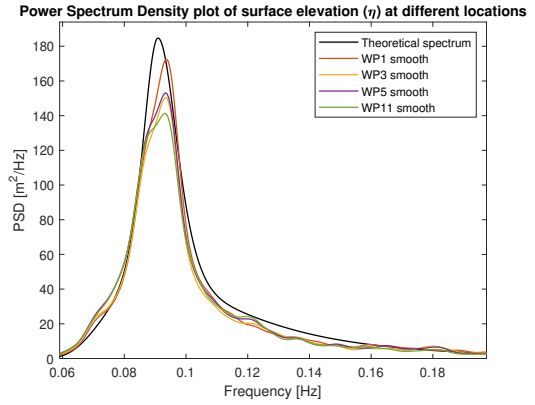

Figure 30: Zoom Power Spectrum Density plot of surface elevation (η) at different locations in the wave tank (WP = Wave Probe)

Location[3]	Rough total Power $[m^2]$	Smooth total Power $[m^2]$	Variance η $[m^2]$
Wave probe 1	4.4031	4.4111	4.4032
Wave probe 3	4.0985	4.1068	4.0986
Wave probe 5	4.3334	4.3411	4.3334
Wave probe 11	4.1646	4.1742	4.1646
Theoretical spectrum	4.6876		

Table 7: Total power of surface elevation (η) at different locations in the wave tank corresponding to both rough and smooth spectra and the total power of the theoretical spectrum

---

[3]Note: The wave probe locations match the experimental setup as indicated in figure 3 in the experiment (Thys et al., 2019b).

This is where the investigation into the potential nonlinear behavior of the forces and moments came to a halt. The reason for this was, as mentioned earlier, that this validation section is not aimed at doing an experimental analysis. However, halting this investigation raised an important question about the significance of nonlinear behavior in fatigue analysis. This is important since the aim of this thesis is to see the influence of the time-varying method on the fatigue assessment relative to the constant method. If nonlinear behavior in the forces and moments is not significant that would give a good reason to not incorporate a load model that includes nonlinear loading.

The initial test for this last point of experimental validation was to check the spectral energy distribution of the linear and nonlinear forces and moments. This is not possible to do with the experimental data due to the lack of details given in the experiment report. However, in the model, this can be checked since the Rainey load model is incorporated. In Figure 31 and Figure 32 the spectral energy distribution for both the force and moment components are shown for $H_s = 8.6$ [m], $T_p = 11.0$ [s] and $\gamma = 4.2$. The conclusion that can be taken from these plots is that the linear force and moment components dominate the spectral energy distribution. Contrary to observations, in severe sea states like the one in question, one would expect that nonlinear forces are not negligible compared to linear forces. However, it should be noted that the scale for the y-axis is not completely fair to the nonlinear force and moment components. Therefore in Figure 33 and Figure 34 only the nonlinear force and moment components spectral energy distributions are shown. What can be seen is that all nonlinear components do have some energy present, the Morison drag component mainly exhibits some energy in the same range as the incident waves whereas F_A coming from the Rainey load model only shows some energy beyond 0.15 [Hz]. The F_I component has almost zero influence on the force spectrum. This is relatively simply explainable since this is a point load and therefore falls away in the total hydrodynamic force that is evaluated here. In the moment plot F_I shows relatively more influence since it acts at the surface elevation and can therefore affect the moment plot more. It should be noted that this analysis is based on a rigid structure, as mentioned in the assumptions made in Chapter 3. What would be even more interesting to see is the structure response per force and moment component. The reason for this is that this would directly affect the fatigue assessment.

Since the actual fatigue assessment will be conducted using SLPE's software, it would be inefficient to perform a full fatigue assessment manually. Therefore, this check was incorporated into a sensitivity study, the results of which are presented in Section 5.5. There, the influence of the nonlinear loads, in this case, the Rainey load model is investigated relative to the Morison load model.
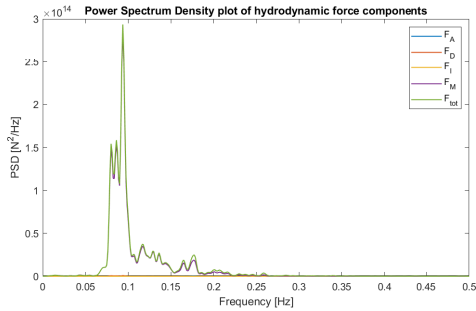

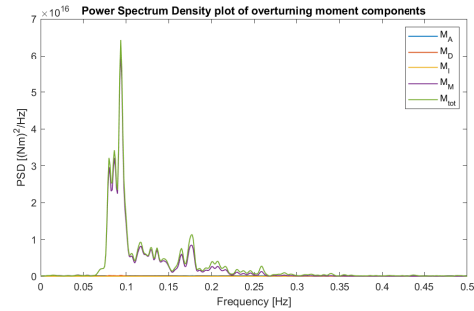Figure 31: Power Spectrum density for hydrodynamic force components [4]

Figure 32: Power Spectrum density for overturning moment components [5]

---

[4]Where F_A = as per Equation 18, F_D = Morison drag component, F_I = as per Equation 18, F_M = Morison inertia component and F_{tot} = total hydrodynamic force.

[5]Where M_A = as per Equation 18, M_D = Morison drag component, M_I = as per Equation 18, M_M = Morison inertia component and M_{tot} = total overturning moment.
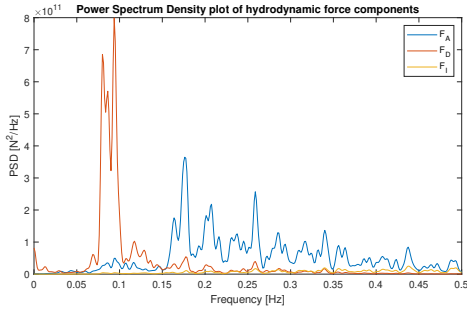
Figure 33: Power Spectrum density for nonlinear hydrodynamic force components
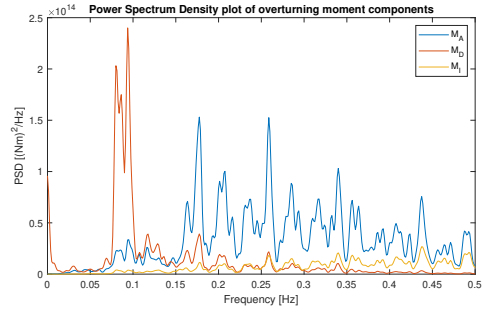

Figure 34: Power Spectrum density for nonlinear overturning moment components

Up until now, only the time-varying coefficient method model was included in the validation. A similar procedure could be established for the constant method. In Figure 35 the results, whilst using first-order wave theory and the Morison load model can be seen for both coefficient models. It can be seen that the two methods give very similar results for the experiment with $H_s = 8.6$ [m], $T_p = 11.0$ [s], and $\gamma = 4.2$.

Therefore it was chosen to not include an in-depth validation for the constant coefficient method. The differences between the two models are so small that the conclusions reached for the time-varying model would also suit the constant model. In Section 5.5 the difference between the two models will be discussed in detail.
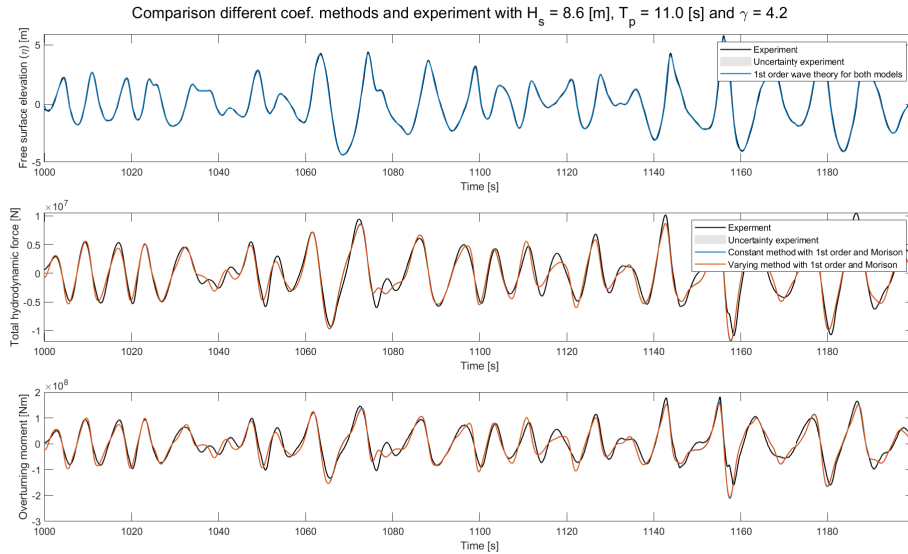

Figure 35: Experimental data, time-varying and constant coefficient model data for $H_s = 8.6$ [m], $T_p = 11.0$ [s] and $\gamma = 4.2$

Also, the fact that the two methods are very close can be confirmed by the time series of the coefficients, as the sea state lies in the mass-dominated regime, the importance of the drag part is reduced, which is shown in Figure 36. Additionally in Figure 37 and Figure 38 the hydrodynamic force and moment coming from the drag part of the Morison load model are shown. They are relatively small compared to the force coming from the inertia part, which is shown in Figure 39 and Figure 40.

Interestingly, the drag coefficient for the time-varying method consistently appears higher than the constant value, whereas the inertia coefficient tends to be lower. This can be understood by examining Figure 16, which shows a plateau for the inertia coefficient when $K_c > 3$. The constant

coefficient, based on the root mean square, corresponds to a K_c number on this plateau, resulting in the maximum value of 2. Similarly, for the drag coefficient, Figure 15 indicates a minimum plateau for $0.75 < K_c < 2$. Thus, the K_c number for the constant coefficient method falls on a plateau in both cases, explaining why the drag coefficient for this time series is always higher or equal and the inertia coefficient for this time series is always lower or equal for the time-varying coefficient method.
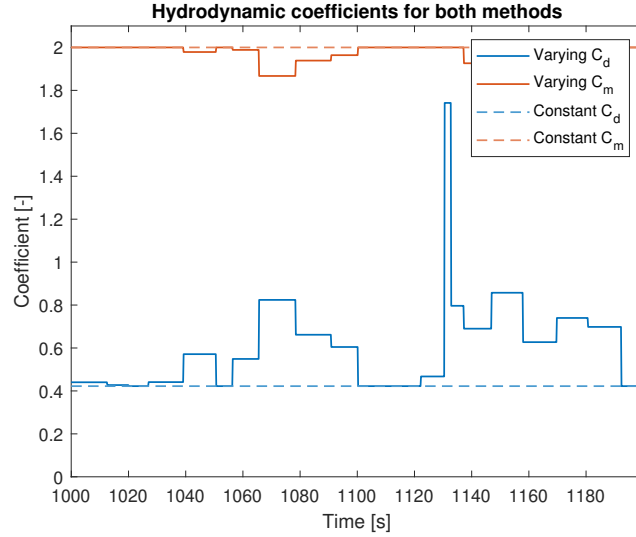
Figure 36: Hydrodynamic coefficients for both the constant and the time-varying model for $H_s = 8.6$ [m], $T_p = 11.0$ [s] and $\gamma = 4.2$

Figure 37: Hydrodynamic drag force for constant and time-varying coefficient method for $H_s = 8.6$ [m], $T_p = 11.0$ [s] and $\gamma = 4.2$

Figure 38: Overturning moment due to drag force for constant and time-varying coefficient method for $H_s = 8.6$ [m], $T_p = 11.0$ [s] and $\gamma = 4.2$
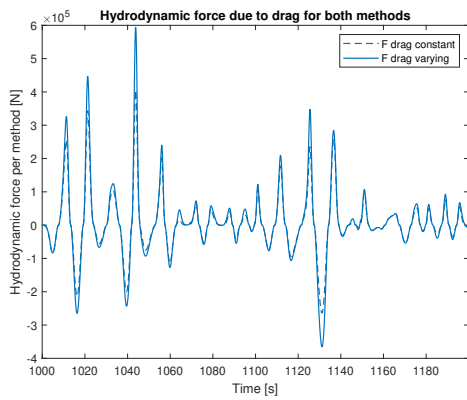
Figure 39: Hydrodynamic inertia force for constant and time-varying coefficient method for $H_s = 8.6$ [m], $T_p = 11.0$ [s] and $\gamma = 4.2$
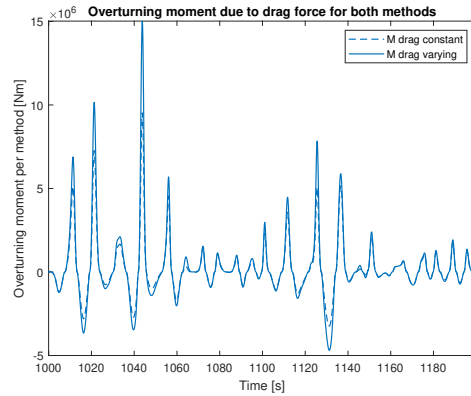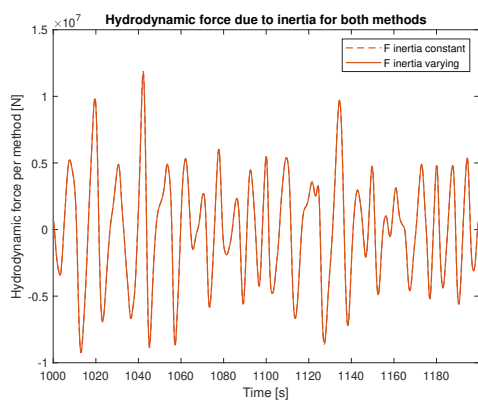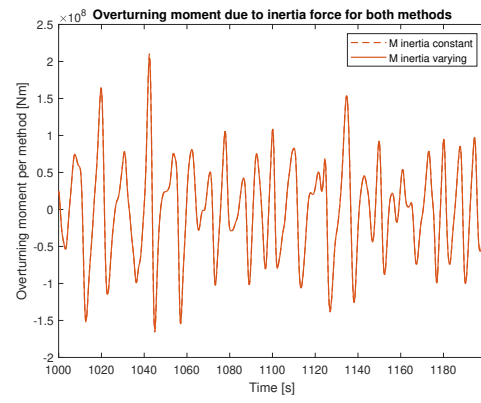

Figure 40: Overturning moment due to inertia force for constant and time-varying coefficient method for $H_s = 8.6$ [m], $T_p = 11.0$ [s] and $\gamma = 4.2$

5 Structural response calculation

This chapter outlines the calculation of structural response, enabling a comparison between two distinct coefficient methods. For clarity, it is divided into five sections. The first section describes the input required for the structural response calculation. The second section explains the execution of the structural calculation. The third section details the obtained output. The fourth section covers the post-processing of the output, leading to the final section, which discusses and evaluates the results.

5.1 Input structural response

In Section 3.6, it is clarified that the hydrodynamic model's output serves as the input for calculating the structural response. However, before this stage, the input for the hydrodynamic model needs to be described, as discussed in Section 3.1. The input file used includes general data, detailed in Table 8. Specifics about structural details are partially provided in the project thesis (Deursen, 2023), which remains unpublished due to it being a confidential property of SLPE (SLPE, n.d.).

Parameters	Value
Water depth (h) [m]	62.42
Water density (ρ) [kg/m^3]	1026.5
Time duration simulation [s]	800
Time step [s]	0.2
Transient time [s]	200
Type of wave spectrum [-]	JONSWAP
Youngs modulus [MPa]	210000
Shear modulus [MPa]	80000
Yield stress [MPa]	355
Monopile length [m]	110
Monopile diameter [6] [m]	11.5 - 8
Number of wave components [-]	400

Table 8: General input data for structural response calculation

Furthermore, as highlighted in Section 2.3, different sea states are necessary for a fatigue assessment. The sea states used here are summarized in Table 9, the reason for it looking relatively patchy compared to normal wave scatter diagrams is the computational time limit. Having fewer, but still representative sea states required less computational time. For more detailed descriptions of these sea states, referred to as different load cases, check Table 16 in Appendix B. It is worth noting that there was no wind applied across all sea states, due to computational constraints, although it is acknowledged that this may not be representative, especially for higher sea states. This means that continuing this study with different wind speeds is set aside for future work.

Table 9 (Occurrence / H(m) vs T(s)):

Occur. T(s)	0 - 0.5	0.5 -1	1 - 1.5	1.5 - 2	2 -2.5	2.5 - 3	3 - 3.5	3.5 - 4	4 - 4.5	4.5 - 5	5 - 5.5	5.5 - 6	6 - 6.5	6.5 - 7	7 - 7.5	7.5 - 8	8 - 8.5
24 - 25																	
23 - 24																	
22 - 23																	
21 - 22																	
20 - 21																	
19 - 20		x		x													
18 - 19		x		x		x											
17 - 18																	
16 - 17		x		x		x											
15 - 16																	
14 - 15		x		x		x		x		x		x					
13 - 14																	
12 - 13		x		x		x		x		x		x		x		x	
11 - 12		x		x		x		x		x		x		x		x	
10 - 11																	
9 - 10		x		x		x		x		x		x					
8 - 9																	
7 - 8		x		x		x		x		x							
6 - 7		x		x		x		x									
5 - 6																	
4 - 5		x		x													
3 - 4																	
2 - 3																	
1 - 2																	
0 - 1																	

Table 9: Overview different sea states with range of H_s and T_p values which are used in the fatigue assessment (for detailed description, reference is made to Table 16 in Appendix B)

Having established the general input and various sea states, the decision was made to construct multiple test cases. These cases aim to scrutinize the impact of toggles implemented in the model, as elaborated in Section 3.1. A comprehensive overview of toggle settings for each test case is presented in Table 10, with debug mode enabled across all cases.

Test cases	Wave theory		Wave cycle		zero-crossing-period		Load model		MacCamy & Fuchs	Coef. method	
	1st Order	2nd Order	Half	Full	Up	Down	Morison	Rainey	diffraction theory	Constant	Varying
1	x		x		x		x		x	x	
2	x		x		x		x		x		x
3	x			x	x		x		x	x	
4	x			x	x		x		x		x
5	x		x		x			x	x	x	
6	x		x		x			x	x		x
7	x			x	x			x	x	x	
8	x			x	x			x	x		x
9	x		x			x	x		x	x	
10	x		x			x	x		x		x
11		x	x		x		x		x	x	
12		x	x		x		x		x		x
13		x	x		x			x	x	x	
14		x	x		x			x	x		x

Table 10: Overview toggle settings for different test cases [7]

With the groundwork laid, the next step involves generating binary wave-loading files through the hydrodynamic model, tailored to each test case's specifications. Following these input procedures, the final input for the structural response calculations materializes into a structured folder arrangement, as depicted in Figure 41. This standardized folder structure is replicated across all test cases.

---

[7]Note: Wheeler stretching is enabled for all test cases even though this is not in accordance with linear wave theory. The reason for enabling it lies in the fact that it is a trade-off against the removal of bound waves which Wheeler stretching corrects (SLPE, n.d.). This statement is supported by the work done by Forristall in 1985 in which experiments were used to validate a new method that calculates the kinematics of random waves above the mean water line (Forristall, 1985).
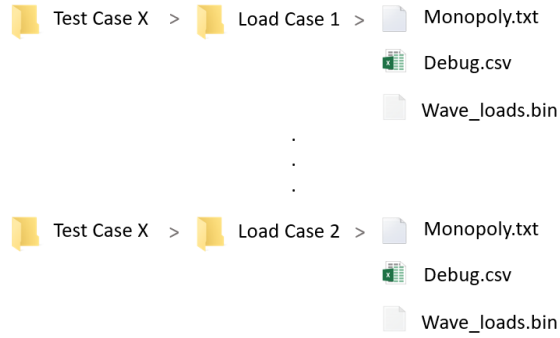
Figure 41: Indicative folder structure for all test cases with input files

5.2   Structural response analysis

For the structural response calculation, MonoPoly, extensively detailed in Section 2.4, is used. Specifically, the Athena and Titan applications within MonoPoly are utilised. Once more, the choice to employ MonoPoly for this task is rooted in its capability to evaluate various coefficient methods and their implications on fatigue within the designated timeframe for this thesis.

In addition to the information provided in Section 2.4, Athena employs a Finite Element Method (FEM) to analyze internal forces. Typically, a beam element model with Gauss integration is used to construct a finite element mesh or model for the stiffness and damping matrices. The hydrodynamic model developed in this thesis utilizes the same mesh to calculate the external force vector. This force vector is then combined in a direct time integration approach to solve the equation of motion, as indicated in Equation 27, using numerical methods. This solution provides critical information such as natural frequencies, dynamic excitation, and responses around specific fundamental moments of the structure.

$$(M + A)\ddot{x} + D\dot{x} + Kx = F \tag{27}$$

Where:

M	is the mass matrix
A	is the added mass matrix
D	is the damping matrix
K	is the stiffness matrix
F	is the external force vector
x	is the displacement of structural component
$\dot{x}$	is the velocity of structural component
$\ddot{x}$	is the acceleration of structural component

Utilizing Athena and Titan was facilitated through the creation of a Matlab script capable of executing external programs. While this functionality could also be implemented through the command prompt of a PC, the decision was made to develop a looping code in Matlab for running both programs across various test cases and associated sea states. This approach was chosen for its simplicity. Additionally, debugging is more feasible with the insights provided in this thesis compared to troubleshooting without the expertise available via the command prompt.

Both Athena and Titan were operated in debug mode, leading to the production of surplus data. Nonetheless, this method enabled easier access for debugging and checking activities, which was crucial to ensuring the reliability of the results.

5.3 Output structural response

Since the debug mode was enabled for both Athena and Titan several output files were generated for all test cases and corresponding sea states. Neglecting the ones that are used for debugging and reliability checks, the main output files are titan.json files, one for each sea state.

These JSON files contain the element end force data and pseudo damage for all can-end numbers evenly distributed around the cylindrical shape of the monopile in 24 locations. This pseudo damage can be interpreted by Equation 28, where m is the Whöler exponent, M_i is the intensity at bin i and n_i is the number of cycles of intensity M_i that have occurred in one sea state.

$$Dpseudo = \sum_i [M_i^m \times n_i] \qquad (28)$$

5.4 Post-processing

To showcase the results of a fatigue assessment two parameters are identified. First is the damage, as per Subsection 2.3.5. The second is the Damage Equivalent Moment (DEM). In this thesis, it was opted to assess the different test cases based on the DEM. The reason for this is that the DEM is a parameter that is found in numerous published papers (Blasques and Natarajan, 2013) and therefore indicates wide recognition from within this sector. Besides, the DEM does not necessitate the choice of an S-N curve, which could spark unwanted discussions that do not matter in terms of the assessment of the different coefficient methods.

The fatigue analysis procedure is typically based on stresses, however, within the DEM approach it is based on the bending moment at mudline, which also originates from stress. Hence, where one would usually read stress, here it is mentioned as the moment. The DEM is thus based on the fatigue damage equivalent bending moment (Lee et al., 2005). The fatigue damage D_i resulting from one load cycle of intensity M_i is given by $D_i = 1/N_i$ where N_i is the number of cycles to failure for a bending moment of intensity M_i. The accumulated damage from a varying number of cycles with different stress intensities is given by $D = \sum_{i=1}^{n_c} D_i = \sum_{i=1}^{n_c} n_i/N_i$. In this expression, n_c is the total number of cycles, and n_i is the number of cycles for which N_i is the limit value at the corresponding bending moment level. The fatigue damage equivalent bending moment is given by Equation 29 (Blasques and Natarajan, 2013).

$$DEM = \left(\frac{\sum_{i=1}^{n_b} n_i M_i^m}{N} \right)^{\frac{1}{m}} \qquad (29)$$

Where n_b is the number of bins used for the cycle counting, n_i and M_i are the number of cycles and moment intensity at bin i, respectively, m is the slope of the S-N curve and is material dependent, and N is a predefined number of cycles.

For irregular load signals, a cycle counting technique is usually employed to determine the amplitudes and means of the underlying load cycles. The rainflow cycle counting technique, as per Subsection 2.3.4 is one example of such a technique and is also used by Titan.

Since the pseudo damage from Titan matches the term in Equation 29 the pseudo damage coming from Titan can quite easily be implemented in the DEM. The only thing left to do is to sum the pseudo damage for all sea states and then use Equation 29 to calculate the DEM. The design of a monopile is rationally symmetrical hence why the maximum of the 24 locations can be taken to calculate the DEM.

After taking these steps for all test cases the DEM can be presented along the depth, which is done in Section 5.5.

5.5   Results and discussion

In Figure 42 and Figure 43 the DEM is presented for all test cases and Whöler exponents. Since the maxima for the different test cases are very similar, Figure 44 was created. This plot has normalized both the maximum and mean values for all test cases with test case 1. This allows for a clear overview of the different test cases' maximum and mean values. Additionally in Table 11 the absolute values belonging to Figure 44 are presented.

What can be seen from these results is that from test case 1 which uses linear wave theory and the Morison equation, all maxima lie within an approximately 7 percent range. For all mean values, this range reduces to 3 percent. Notably these ranges are not really affected by the Whöler exponent, for which similar plots are presented in Appendix B in Figure 70 and Figure 71.
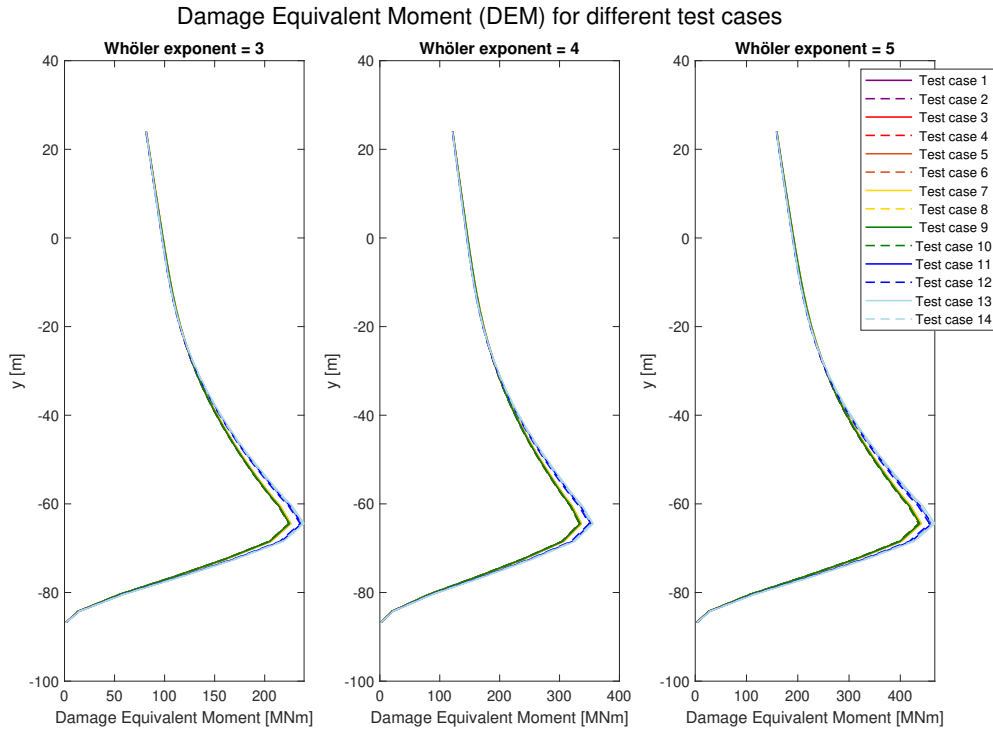
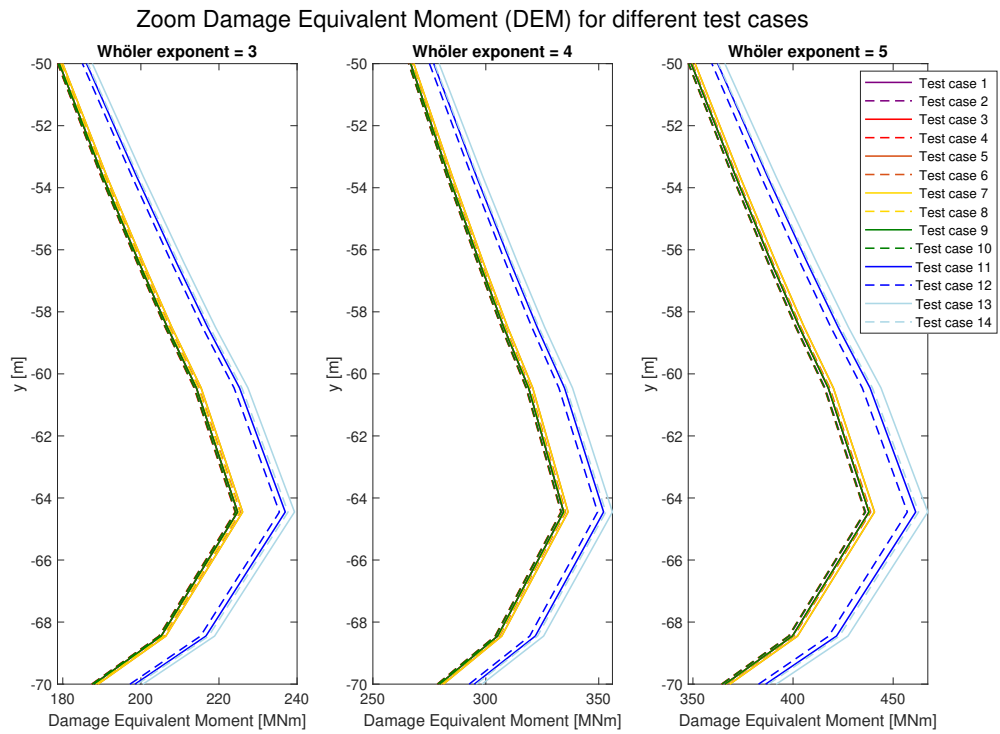Figure 42: Damage Equivalent Moment (DEM) along the depth for different Wöler exponents

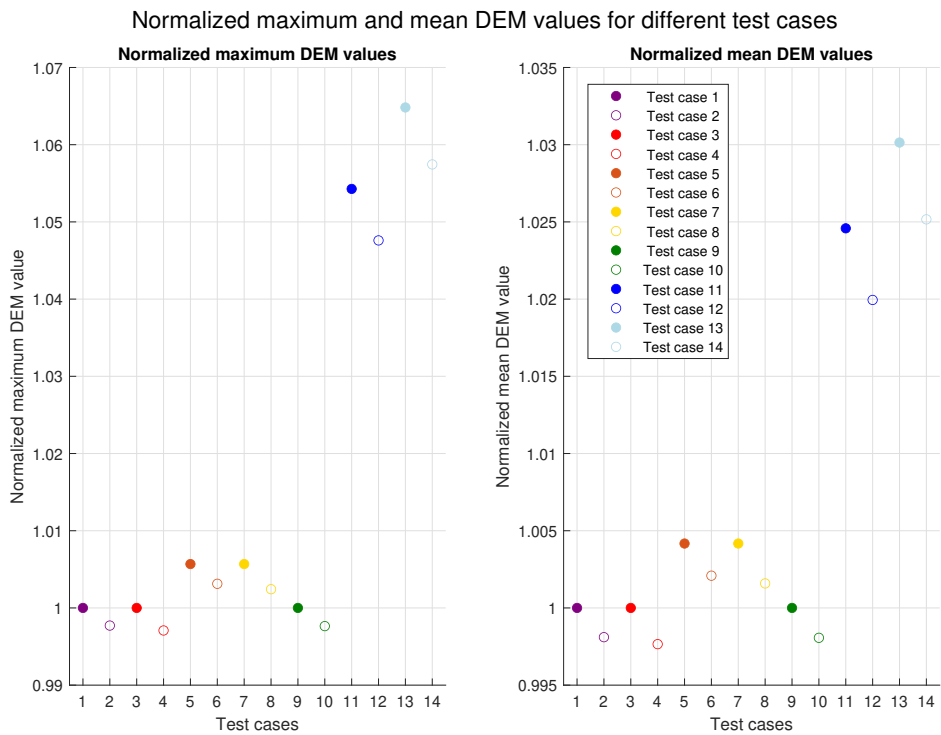Figure 43: Zoom Damage Equivalent Moment (DEM) along the depth for different Wöler exponents

Figure 44: Mean and maximum Damage Equivalent Moment (DEM) for all test cases with $m = 3$ normalized with test case 1

Test case	Max DEM			Mean DEM		
	m = 3	m = 4	m = 5	m = 3	m = 4	m = 5
1	224.77	334.47	437.93	124.84	186.04	243.38
2	224.26	333.47	436.24	124.60	185.61	242.71
3	224.77	334.47	437.93	124.84	186.04	243.38
4	224.12	333.20	435.80	124.54	185.51	242.56
5	226.05	336.41	440.67	125.36	186.82	244.45
6	225.48	335.29	438.78	125.10	186.35	243.71
7	226.05	336.41	440.67	125.36	186.82	244.45
8	225.32	334.99	438.27	125.03	186.24	243.54
9	224.77	334.47	437.93	124.84	186.04	243.38
10	224.25	333.38	435.99	124.59	185.58	242.62
11	236.97	352.15	461.26	127.90	190.28	248.85
12	235.47	349.48	457.08	127.33	189.28	247.34
13	239.34	356.06	467.30	128.60	191.40	250.53
14	237.69	353.14	462.70	127.98	190.33	248.90

Table 11: Maximum and mean values for all test cases

Since all different test cases have been done, it is interesting to see the effect of the different toggle settings that are induced by the different test cases. But first, let us look into the differences between the constant and time-varying coefficient method. From Figure 43 it is already apparent that all dashed lines, referring to the time-varying method lie left from the full lines. This indicates that the constant coefficient method is conservative relative to the time-varying one. This is also confirmed by Table 12 which shows the difference between the constant and time-varying method for all test case pairs since all values are smaller than zero. For clarity, the differences indicated in Table 12 are calculated via Equation 30, which is an example for test case 1 - 2.

$$\Delta\text{max DEM} = 100 \times (\text{maxDEM}_2 - \text{maxDEM}_1)/\text{maxDEM}_1$$
$$\Delta\text{mean DEM} = 100 \times (\text{meanDEM}_2 - \text{meanDEM}_1)/\text{meanDEM}_1$$

(30)

Test case	Δ max DEM [%]			Δ mean DEM [%]		
	m = 3	m = 4	m = 5	m = 3	m = 4	m = 5
1 - 2	-0.23	-0.30	-0.39	-0.19	-0.23	-0.27
3 - 4	-0.29	-0.38	-0.49	-0.23	-0.28	-0.34
5 - 6	-0.25	-0.33	-0.43	-0.21	-0.25	-0.30
7 - 8	-0.32	-0.42	-0.54	-0.26	-0.31	-0.37
9 - 10	-0.24	-0.33	-0.44	-0.19	-0.25	-0.31
11 - 12	-0.63	-0.76	-0.91	-0.45	-0.53	-0.61
13 - 14	-0.69	-0.82	-0.98	-0.48	-0.56	-0.65

Table 12: Difference in maximum and mean DEM values for constant and time-varying method

Even though all values in Table 12 are negative there still exists a range. The range of max values is approximately 0.8 percent and for mean values, it is 0.5 percent. Besides the fact that the difference increases with the increase of m, also a clear increase in differences is seen between the first 10 cases and the last 4. Indicating a sensitivity with respect to the toggle settings in these different test cases.

In Table 13 the difference between the different toggle settings is indicated via a similar approach. Going through these toggles one by one, starting with the load model toggle it can be seen that this toggle does affect the results. For the test cases with linear wave theory, the max values increase by approximately 0.55 percent and the mean values increase by 0.40 percent going from the Morison load model to the Rainey load model. For the test case with second-order wave theory,

this range seems to increase to approximately 1 percent for the maximum values and 0.55 for the mean values. This could indicate a connection between the wave theory toggle and the load model toggle.

Toggle sensitivity	Test case	Δ max DEM [%]			Δ mean DEM [%]		
		m = 3	m = 4	m = 5	m = 3	m = 4	m = 5
Load model	2 - 6	0.54	0.55	0.58	0.40	0.40	0.41
	4 - 8	0.54	0.54	0.57	0.39	0.39	0.40
	12 - 14	0.94	1.05	1.23	0.51	0.55	0.63
Wave theory	2 - 12	5.00	4.80	4.78	2.19	1.98	1.91
	6 - 14	5.41	5.32	5.45	2.30	2.14	2.13
Wave cycle type	2 - 4	-0.06	-0.08	-0.10	-0.05	-0.05	-0.06
	6 - 8	-0.07	-0.09	-0.11	-0.05	-0.06	-0.07
Zero-crossing period	2 - 10	-0.01	-0.03	-0.06	0.00	-0.02	-0.04

Table 13: Difference in maximum and mean DEM values for different toggle settings

Continuing to the wave theory toggle it shows that the average change from linear wave theory to second-order wave theory increases the maximum by approximately 5 percent and the mean values by approximately 2 percent. It is noted however that for the test cases with the Morison load model, these values are slightly below average and for the Rainey load model these are slightly above average. This together with the fact that test cases 2 - 6 and 4 - 8 show different ranges compared to 12 - 14 for the load model toggle indicate that there might be a connection between these two toggles.

Diving deeper into this observation it becomes apparent that the sea state with $H_s = 8$ [m], $T_p = 11.2$ [s], and $\gamma = 3.31$ contributes the most to the max total DEM for all test cases. Hence why we will zoom into this sea state, also referred to as load case. In Table 14 the characteristics of this load case are shown for all test cases relating to these two toggles. In the maximum DEM of these test cases, we see the same relation as in Figure 44. Since the different load cases do not contribute linearly to the total DEM values from Figure 42, as can be seen in Equation 29. The magnitude of the maximum DEM indicated in Table 14 is not relevant relative to the ones shown in Figure 42. But if these values are normalized we get a similar relation. Therefore it should be possible to focus on this load case in order to explain the connection between these two toggles instead of analyzing all of the load cases.

The first thing that draws attention is the difference in significant wave height between the first-order and second-order wave theory test cases. This however follows the typical characteristics of the second-order wave theory that relative to the linear one shows higher peaks and lower throughs in the surface elevation. Consequently, a higher significant wave height whilst keeping the peak period the same will cause higher extreme horizontal velocities. This explains why the mean K_c number for test cases 12 and 14 is higher. Higher K_c numbers will cause higher C_d and lower C_m values which is also seen in the data. Additionally, the higher order wave theory causes steeper waves which also causes higher extreme horizontal velocities and therefore a bigger range in K_c numbers compared to first order wave theory. Furthermore, it should be noted that the wave characteristics, H_s and T_p, are not affected by the different load models, which is needed for a fair comparison. And regarding the extremely high maximum values for C_d, these are associated with very low velocities.

Now something that cannot be explained from the data is why the maximum DEM is higher for the test cases that use the Rainey load model compared to the Morison load model. It is expected that the reason for this lies in the fact that the Rainey load model introduces more nonlinear terms than the Morison load model. To investigate this further a spectral analysis of the surface elevation, forces, and moments was done. The results of this are shown in Figure 45. The results seem very similar, which does not directly confirm or deny the hypothesis. The difference in maximum DEM is very small, so maybe the spectral analysis is not the right scale to make a comparison.
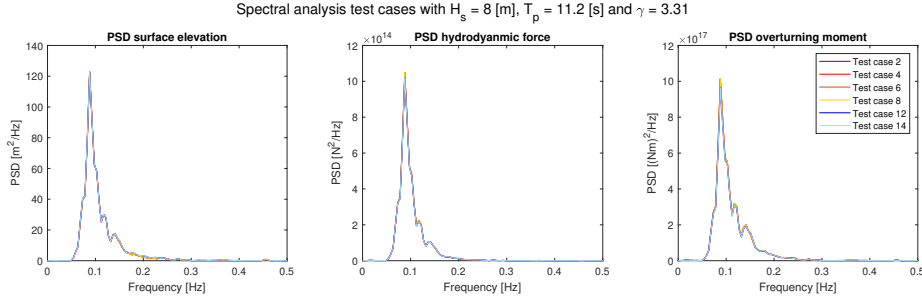
Figure 45: Spectral analysis test cases with $H_s = 8$ [m], $T_p = 11.2$ [s] and $\gamma = 3.31$

The other comparison that was done was between the total force and overturning moment between the Rainey and Morison test cases. Also, the differences here are small and no direct conclusion can be made. The only clear difference is that the difference between the Rainey load model and the Morison model has a negative mean value. Meaning that the loads coming from the Rainey load model are slightly higher. Looking at the different load models, this can only be explained by the two additional terms that transform the Morison load model into the Rainey load model. For the test cases with second-order wave theory, this negative mean value is bigger, therefore explaining the difference in why Rainey affects the maximum DEM for second-order wave theory more. Coming back to the statement made in Subsection 4.4.2, the nonlinear loads thus affect the input loads for the structural response calculation. This size of impact is dependent on the wave theory used, therefore referring to the order of wave theory.

Test case	Max DEM [MNm]	H_s [m]	T_P [s]	C_d range [-]			C_m range [-]			K_c range [-]		
				min	max	mean	min	max	mean	min	max	mean
2	130.26	8.00	11.26	0.42	1.64	0.55	1.85	2.00	1.98	0.11	6.40	2.61
4	130.24	8.00	11.26	0.42	1.46	0.58	1.85	2.00	1.97	0.24	6.40	2.95
6	130.97	8.00	11.26	0.42	1.64	0.55	1.85	2.00	1.98	0.11	6.40	2.61
8	130.95	8.00	11.26	0.42	1.46	0.58	1.85	2.00	1.97	0.24	6.40	2.95
12	138.55	8.13	11.26	0.42	1.90	0.63	1.67	2.00	1.94	0.02	10.51	3.40
14	141.11	8.13	11.26	0.42	1.90	0.63	1.67	2.00	1.94	0.02	10.51	3.40

Table 14: Characteristics of sea state with $H_s = 8$ [m], $T_p = 11.2$ [s] and $\gamma = 3.31$ for different test cases [8]

Now for the wave cycle type toggle it shows that the half wave cycle-based test cases reduce the max values by approximately 0.08 percent and the mean values by 0.05 percent. This makes sense in a way that for the half-wave cycle, the extreme horizontal velocity is never bigger than the one for the full-wave cycle. In the extreme case that the max horizontal velocity is the same as the min horizontal velocity then both types would give the same result. But in most cases, this is not the case, therefore for either the trough or the crest the result is the same as for the full wave cycle, and for the other, it is less. It is therefore conservative to proceed future work with the full wave cycle analysis. Additionally one could argue that the K_c number is related to a full cycle, so calculating it for half a cycle does not meet the K_c definition and therefore loses its reliability.

Lastly, for the zero-crossing period toggle it shows that the differences are very small for both max and mean values. Confirming the hypothesis from Section 3.3. Since all values are smaller or equal to zero it is conservative to proceed future work with the zero-up-crossing period.

In Section 3.7 it was already mentioned that the constant coefficient method used in this thesis is not the exact same as the one recommended by ISO. As a small side study, some load cases were also run with the coefficient method exactly following the recommended practice by ISO. The load cases that were selected for this are load cases 4, 7, 11 till 15, and 32. The reason for opting for these load cases lies in the high probability of occurrence and wave height range. Especially the

---

[8]Note: The K_c number range changes over depth, since the force contribution at the free surface water level is the largest, especially for the overturning moment the range is indicated at the free surface water level.

wave height range is important here since it was already found that the time-varying coefficient method would affect higher sea states more due to the larger K_c fluctuations (Deursen, 2023). The results are shown in a similar fashion to the previous test cases in Figure 46 and Table 15. Note that the probabilities for the load cases were kept the same relative to the other test cases, however since the number of load cases is smaller the absolute values for maximum and mean DEM cannot be compared with the 14 test cases discussed earlier. Additionally, figures like Figure 42 and Figure 43 were created for this side study which can be found in Section B in Figure 72 and Figure 73.
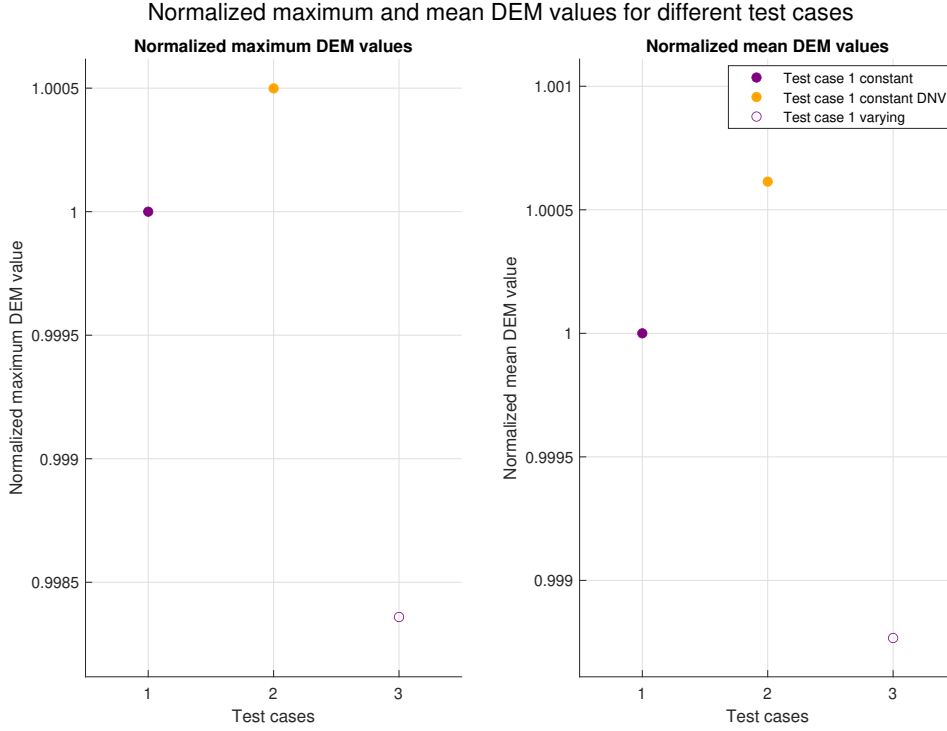
Figure 46: Mean and maximum Damage Equivalent Moment (DEM) for side study with $m = 3$ normalized with test case 1 constant

Test case	Max DEM			Mean DEM		
	m = 3	m = 4	m = 5	m = 3	m = 4	m = 5
1 constant	168.07	270.94	368.84	95.82	155.02	212.63
1 constant ISO	168.15	271.10	369.09	95.88	155.13	212.75
1 varying	167.79	270.39	367.99	95.7	154.81	212.31

Table 15: Maximum and mean values for all test cases as part of side study

What is apparent from the results is that the constant coefficient method by ISO is even more conservative than the one used in this thesis. So the more advanced version, which is also used by industry already seems to go in the direction of the time-varying coefficient method.

In summary, the time-varying coefficient method decreases the maximum DEM values by 0.2 to 0.7 percent depending on the different toggle settings. The mean DEM values decrease by a range of 0.2 to 0.5 percent. This is however relative to a more advanced constant coefficient method compared to the one recommended by ISO. If the time-varying coefficient method were to be compared with that one, the decrease in DEM values would be even bigger, relatively speaking.

For thin-walled cylinders, where $t \ll R$, the section modulus, W, can be simplified to $W = \pi R^2 t$. Since the stress can be defined by $\sigma = M/W$, where M represents the overturning moment, it can

be stated that with a 0.5 percent reduction in the mean DEM, the thickness of the monopile can be reduced by 0.5 percent to maintain the stress at the same level. A 0.5 percent reduction in wall thickness for an average wind farm, for example, 80 foundations weighing 2500 [mT] each, could save several million euros.

6 Conclusion & recommendations

6.1 Conclusion

The investigation presented in this thesis was focused on broadening the range for which bottom-founded offshore wind, specifically monopiles, are economically viable. The main focus was on developing a new calculation method that calculates the wave loading more accurately with respect to the hydrodynamic coefficients. The central objective of this thesis was to:

Determine whether the establishment of time-varying coefficients within the first and second-order irregular wave theory increases the accuracy of the wave loads, and investigate what the influence is of this newly established calculation technique on the fatigue life of an XXL monopile.

To reach this objective, several research questions were formulated, as well as a coherent and structured research approach. The research included the development of the time-varying coefficient method by implementing a Keulegan-Carpenter number and Reynolds number dependency for both the inertia and drag coefficient. Using the model, which included the newly developed methodology and the methodology used by the industry, the resulting forces could be validated via an experiment and therefore fulfill the first part of the objective.

The validation included the attempt to reproduce the experimental data by M. Thys, F. H. Dadmarzi, and E. Bachynski. A selection of regular and irregular waves was made to ensure a detailed check. The regular wave results matched the experimental data fairly accurately, especially for the waves with a steepness of 1/40. Even though this wave had the lowest steepness of all wave experiments, it was clear that second-order wave theory matched the best for all outputs, the surface elevation, the total hydrodynamic force, and the overturning moment. For the steeper waves, with steepness going up to 1/20, second-order wave theory was clearly insufficient in terms of capturing all characteristics and therefore the reproduction was less accurate.

The more difficult attempt to reproduce irregular waves from the experiments brought some difficulties since the report of the experiment did not include enough detail about the random phases and wave components. By bypassing this issue via an FFT of the surface elevation the model was able to reproduce the surface elevation of the experiment. This was however limited to first-order wave theory due to the linearization of the free surface elevation which is induced by the FFT. In this context, linearization means that decomposing the surface elevation using FFT masks the nonlinear interaction effects present in the surface elevation. Even though the first-order wave theory model was able to reproduce the surface elevation accurately, both the forces and moments were not reproduced accurately. Spectral analysis showed that nonlinearities in the forces and moments were present which were not present in the surface elevation. Due to time and objective limitations, further analysis of these nonlinearities was stopped. Only a sensitivity study was set out for the structural response calculation to see the influence of nonlinearities in the forces on the fatigue assessment.

Due to the fact that the surface elevation could not be matched accurately by the second-order wave theory because of the linearization of the experimental surface elevation, as described earlier, the total hydrodynamic force and overturning moment matched the experimental data worse than the first-order wave theory. A solution to solve this issue, which was an iterative method to minimize the error, was identified but not further elaborated on. The reason for this was that it would not have affected the fatigue assessment due to the fact that the fatigue assessment depends on theoretical spectra instead of full-scale experiments.

The second part of the objective was fulfilled by using the model to generate wave forces inside a fatigue assessment. Not only the difference between the two different methodologies could be checked but also the influence of this newly established calculation technique by inclusion of different toggle settings. The toggle settings, allow for different methodology configurations.

The results showed a decrease in maximum and mean DEM for all test cases. There was however no exact difference between the different methodologies whilst using different method configurations, and therefore indicating some sensitivity. Overall the results showed that the time-varying

coefficient method decreases the maximum DEM values by 0.2 to 0.7 percent depending on the different toggle settings. The mean DEM values decrease by a range of 0.2 to 0.5 percent.

Not all toggle settings showed a large sensitivity, for example, the difference between a zero-up-crossing period and a zero-down-crossing period was proven to be negligible. Also, the difference between the half-wave cycle and the full-wave cycle appeared to be small. However, in both cases, a conservative approach could be established, which is using the zero-up-crossing period and the full-wave cycle configuration.

Both the toggles for the wave theory and the load model did not affect the methodology configuration. However, by implementing the methodology for the different wave theories and or different load models the influence of the newly established methodology seems to affect the second-order wave theory model together with the Rainey load model the greatest whereas the first-order wave theory model with the Morison load model is affected the least. The reason for this is the larger range of K_c numbers that occur whilst using the second-order wave theory.

The constant coefficient method used in this thesis and by industry can be viewed as an advanced version of the constant coefficient method recommended by ISO. A side study showed that the decrease in DEM values would be even greater when comparing this newly established method with the one recommended by ISO. Therefore, it suggests that the constant coefficient method used by industry is moving toward the direction of the time-varying coefficient method.

Finally, for thin-walled cylinders like monopiles, where $t \ll R$, the relationship between the moment and thickness is essentially linear. Therefore, with a 0.5 percent reduction in mean diameter equivalent mean (DEM), the thickness of the monopile can be reduced by 0.5 percent to maintain stress levels. This reduction in material thickness has the potential to save several million euros for wind farms.

6.2 Recommendations

Since the trend of the results is that the newly established method reduces the DEM, checking its accuracy in greater detail is the primary task for future work. If its accuracy can be validated to a better extent for irregular waves it could possibly increase the cost-effectiveness of monopiles. Leading to an increase in the range for which bottom-founded OWTs are economically viable.

Checking its accuracy in greater detail requires an in-depth validation procedure where irregular wave experiments are reproduced to the same accuracy as regular waves are reproduced in this thesis. Establishing this would serve as a good follow-up to assess the influence of this newly established method on a non-simplified fatigue assessment

Since this methodology can as easily be implemented for deep water sites as for shallow water sites. For future work, exploring the influence of water depth on this newly established method would be of interest. This refers to the fact that the natural frequency of the monopile is largely dependent on the water depth. Together with the nonlinear wave kinematics that take place in intermediate and shallow water depths. Which both matters a lot for the structural response initiated by wave loading.

Furthermore, it is interesting to see the impact of the assumptions made within this thesis by developing a newer model in the future that does not assume a rigid structure, that goes beyond second-order wave theory and has a nonzero current velocity option. This will especially be relevant if not only FLS conditions are checked with the time-varying coefficient method but also ULS conditions. For ULS conditions, nonlinearities play a much bigger role compared to the FLS conditions, and therefore the currently made assumptions might largely affect the results.

Bibliography

Bachynski, E, Trygve Kristiansen and Maxime Thys (2017). 'Experimental and numerical investigations of monopile ringing in irregular finite-depth water waves'. In: *Applied Ocean Research* 68, pp. 154–170. DOI: 10.1016/j.apor.2017.08.011. URL: http://dx.doi.org/10.1016/j.apor.2017.08.011.

Baekkedal, Eivind (2014). *Alternative methods of realizing the sea spectrum for time-domain simulations of marine structures in irregular seas.* Tech. rep.

Blasques, J P A A and A Natarajan (2013). *Mean load effects on the fatigue life of offshore wind turbine monopile foundations.* Tech. rep., pp. 818–829.

Bredmose et al. (June 2013). 'Dynamic Excitation of Monopiles by Steep and Breaking Waves: Experimental and Numerical Study'. In: *Volume 8: Ocean Renewable Energy.* American Society of Mechanical Engineers. ISBN: 978-0-7918-5542-3. DOI: 10.1115/OMAE2013-10948.

De Ridder, Erik-Jan et al. (2011). *The dynamic response of an offshore wind turbine with realistic flexibility to breaking wave impact.* Tech. rep. URL: www.flyingfocus.nl.

De Vos, Leen, Peter Frigaard and Julien De Rouck (Jan. 2007). 'Wave run-up on cylindrical and cone shaped foundations for offshore wind turbines'. In: *Coastal Engineering* 54.1, pp. 17–29. ISSN: 03783839. DOI: 10.1016/j.coastaleng.2006.08.004.

Deursen, Thomas van (2023). *Project thesis - Preliminary study on fatigue assessment of large-scale bottom-fixed wind turbines in waves.* Tech. rep. Unpublished.

DNV (2021a). *DNV-ST-0126 Support structures for wind turbines.* Tech. rep.

— (2021b). *Recommended practice DNV-RP-C203 - Fatigue design of offshore steel structures.* Tech. rep.

— (2021c). *Recommended practice DNV-RP-C205 - Environmental conditions and environmental loads.* Tech. rep.

Dummer, J (1988). *Instantaneous Morison Equation Force Coefficients Computation.* Tech. rep. Naval Civil Engineering Laboratory.

Empire Engineering (2023). *The Empire Engineering Guide to Offshore Wind Foundations -Challenges and opportunities in designing and developing offshore wind foundations both now and in the future. SECOND EDITION.* Tech. rep.

Fage, A and J H Warsap (1929). *The effects of turbulence and surface roughness on the drag of circular cylinders.* Tech. rep.

Faltinsen, O. M. (1990). *Sea Loads on Ships and Offshore Structures.* Cambridge Ocean Technology Series. Cambridge University Press. ISBN: 9780521372855. URL: https://books.google.no/books?id=MTVgQgAACAAJ.

Faltinsen, O. M., J. Newman and T. Vinje (Apr. 1995). 'Nonlinear wave loads on a slender vertical cylinder'. In: *Journal of Fluid Mechanics* 289, pp. 179–198. ISSN: 0022-1120. DOI: 10.1017/S0022112095001297. URL: https://www.cambridge.org/core/product/identifier/S0022112095001297/type/journal_article.

Federal Highway Administration (2020). *HEC-25 - Highways in the Coastal Environment - 3rd Edition.* Tech. rep.

Forristall, George (1985). *Irregular wave kinematics from a kinematic boundary condition fit (KBCF) The Netherlands.* Tech. rep.

Fuhrman, David R., Mathias Klahn and Yanyan Zhai (Sept. 2023). 'A new probability density function for the surface elevation in irregular seas'. In: *Journal of Fluid Mechanics* 970. ISSN: 14697645. DOI: 10.1017/jfm.2023.669.

Galvin, Cyril J. (June 1968). 'Breaker type classification on three laboratory beaches'. In: *Journal of Geophysical Research* 73.12, pp. 3651–3659. ISSN: 01480227. DOI: 10.1029/JB073i012p03651.

Goda, Y (2010). *Random Seas and Design of Maritime Structures.* Advanced series on ocean engineering. World Scientific. ISBN: 9789814282390. URL: https://books.google.nl/books?id=v_unn4FtFXsC.

Hallowell, S., A. T. Myers and S. R. Arwade (Feb. 2016). 'Variability of breaking wave characteristics and impact loads on offshore wind turbines supported by monopiles'. In: *Wind Energy* 19.2, pp. 301–312. ISSN: 1095-4244. DOI: 10.1002/we.1833.

IEC (2019a). *IEC-61400-1: Wind energy generation systems Part 1: Design requirements.* Tech. rep.

IEC (2019b). *IEC-61400-3: Design requirements for fixed offshore wind turbines*. Tech. rep. URL: www.ds.dk.

International Energy Agency (2021). *Net Zero by 2050 - A Roadmap for the Global Energy Sector*. Tech. rep. URL: https://www.iea.org/reports/net-zero-by-2050.

ISO (2019). *19900: Petroleum and natural gas industries-General requirements for offshore structures*. Tech. rep.

— (2020). *19902:Petroleum and natural gas industries-Fixed steel offshore structures*. Tech. rep.

Jeong, Ho-Jin, Weoncheol Koo and Sung-Jae Kim (Aug. 2020). 'Numerical Study on Wave Run-up of a Circular Cylinder with Various Diffraction Parameters and Body Drafts'. In: *Journal of Ocean Engineering and Technology* 34.4, pp. 245–252. ISSN: 1225-0767. DOI: 10.26748/ksoe. 2020.026.

Kauzlarich, J J (1989). 'The Palmgren-Miner rule derived'. In: *Tribology Series*. Ed. by D Dowson et al. Vol. 14. Elsevier, pp. 175–179. ISBN: 0167-8922. DOI: https://doi.org/10.1016/S0167-8922(08)70192-5. URL: https://www.sciencedirect.com/science/article/pii/S0167892208701925.

Keulegan, Garabis Hvannes and Lloyd Carpenter (1958). *Forces on Cylinders and Plates in an Oscillating Fluid 1*. Tech. rep. 5.

Kristiansen, T. and O. M. Faltinsen (Dec. 2017). 'Higher harmonic wave loads on a vertical cylinder in finite water depth'. In: *Journal of Fluid Mechanics* 833, pp. 773–805. ISSN: 0022-1120. DOI: 10.1017/jfm.2017.702. URL: https://www.cambridge.org/core/product/identifier/S0022112017007029/type/journal_article.

Kühn, Martin (2001). *Dynamics and design optimisation of offshore wind energy conversion systems*. Tech. rep. URL: https://www.researchgate.net/publication/34768668.

Lee, Yung-Li et al. (2005). *Fatigue Testing and Analysis - Theory and Practice*. Elsevier.

LeMéhauté, B (1976). *An Introduction to Hydrodynamics and Water Waves*. Springer study edition. Springer-Verlag. ISBN: 9783540072324. URL: https://books.google.no/books?id=Rn8pAQAAMAAJ.

MacCamy, R. C. and R. A. Fuchs (1954). *Wave forces on piles: a diffraction theory*. Tech. rep. Technical Memorandum No. 69, Beach Erosion Board Corps of Engineers.

Madsen, Per A. and David R. Fuhrman (May 2012). 'Third-order theory for multi-directional irregular waves'. In: *Journal of Fluid Mechanics* 698, pp. 304–334. ISSN: 0022-1120. DOI: 10.1017/jfm.2012.87.

Malik, M (2015). *Hydrodynamic Modeling of Forces on Vertical Cylinders, Project Thesis*. Tech. rep. NTNU.

— (2016). *Hydrodynamic Modelling Effects on Fatigue Calculations for Monopile Offshore Wind Turbines*. Tech. rep.

Marthinsen, Tom and Steven R Winterstein (1992). 'ON THE SKEWNESS OF RANDOM SURFACE WAVES'. In: *Proceedings of the 2nd International Offshore and Polar Engineering Conference* 3. URL: https://api.semanticscholar.org/CorpusID:127588391.

McNown, J S and Garabis Hvannes Keulegan (Jan. 1959). 'Vortex Formation and Resistance in Periodic Motion'. In: *Journal of the Engineering Mechanics Division* 85.1, pp. 1–6. DOI: 10.1061/JMCEA3.0000078. URL: https://doi.org/10.1061/JMCEA3.0000078.

Morison, J R et al. (1950). *The force exerted by surface waves on piles*. Tech. rep. URL: http://onepetro.org/JPT/article-pdf/2/05/149/2238818/spe-950149-g.pdf/1.

Noonan, Miriam (2021). *The benefits of hybrid bottom-fixed and floating wind sites*. Tech. rep.

Nybø, Astrid et al. (Sept. 2020). 'Evaluation of different wind fields for the investigation of the dynamic response of offshore wind turbines'. In: *Wind Energy* 23.9, pp. 1810–1830. ISSN: 1095-4244. DOI: 10.1002/we.2518.

Orsted (2019). *Making green energy affordable How the offshore wind energy industry matured-and what we can learn from it*. Tech. rep.

Rainey, R. C. T. (July 1989). 'A new equation for calculating wave loads on offshore structures'. In: *Journal of Fluid Mechanics* 204.-1, p. 295. ISSN: 0022-1120. DOI: 10.1017/S002211208900176X. URL: http://www.journals.cambridge.org/abstract_S002211208900176X.

— (1990). 'Energy arguments under a "wavy lid" - A new approach to capsizing and other highly nonlinear problems'. In: URL: https://api.semanticscholar.org/CorpusID:114089012.

— (1995). *Slender-Body Expressions for the Wave Load on Offshore Structures*. Tech. rep., pp. 391–416. URL: https://about.jstor.org/terms.

Reid, R. O. (1956). *Analysis of wave forces experiments at Caplen, Texas: (Sun Oil Company Platform), final report*. Reference ;56-2F.FU. College Station, Tex.: Texas A & M University, Dept.

of Oceanography, 1 v. (various pagings). URL: //catalog.hathitrust.org/Record/103078166%20http://hdl.handle.net/2027/ufl.31262080846347.

Rienecker, M. M. and J. D. Fenton (Mar. 1981). 'A Fourier approximation method for steady water waves'. In: *Journal of Fluid Mechanics* 104, pp. 119–137. ISSN: 0022-1120. DOI: 10.1017/S0022112081002851. URL: https://www.cambridge.org/core/product/identifier/S0022112081002851/type/journal_article.

Seidel, Marc (2014). 'Wave Induced Fatigue Loads on Monopiles'. In: Osnabrück: International Wind Engineering Conference. URL: www.senvion.com.

SLPE (n.d.). *Sea and Land Project Engineering*. URL: https://www.slpe.com/.

Söker, H. (Jan. 2013). 'Loads on wind turbine blades'. In: *Advances in Wind Turbine Blade Design and Materials*, pp. 29–58. DOI: 10.1533/9780857097286.1.29.

Stansberg, Carl Trygve and Ove Tobias Gudmestad (1996). *Non-linear random wave kinematics models verified against measurements in steep waves*. English. United States: American Society of Mechanical Engineers, New York, NY (United States). URL: https://www.osti.gov/biblio/449646.

Stansberg, Carl Trygve, Ove Tobias Gudmestad and Sverre K. Haver (May 2008). 'Kinematics under extreme waves'. In: *Journal of Offshore Mechanics and Arctic Engineering*. Vol. 130. 2. DOI: 10.1115/1.2904585.

Stewart, Gordon and Michael Muskulus (2016). 'A Review and Comparison of Floating Offshore Wind Turbine Model Experiments'. In: *Energy Procedia*. Vol. 94. Elsevier Ltd, pp. 227–231. DOI: 10.1016/j.egypro.2016.09.228.

Stoker, J J (1957). *Water Waves: The Mathematical Theory with Applications*. Mathematical Theory with Applications. Interscience Publishers. ISBN: 9780470828632. URL: https://books.google.no/books?id=1G-5uAEACAAJ.

Suja-Thauvin, L, E Bachynski et al. (July 2020). 'Critical assessment of hydrodynamic load models for a monopile structure in finite water depth'. In: *Marine Structures* 72, p. 102743. ISSN: 0951-8339. DOI: 10.1016/J.MARSTRUC.2020.102743.

Suja-Thauvin, L, Jørgen R Krokstad, E Bachynski et al. (Dec. 2017). 'Experimental results of a multimode monopile offshore wind turbine support structure subjected to steep and breaking irregular waves'. In: *Ocean Engineering* 146, pp. 339–351. ISSN: 0029-8018. DOI: 10.1016/J.OCEANENG.2017.09.024.

Suja-Thauvin, L, Jørgen R Krokstad and Joakim Fürst Frimann-Dahl (2016). 'Maximum Loads on a One Degree of Freedom Model-scale Offshore Wind Turbine'. In: *Energy Procedia*. Vol. 94. Elsevier Ltd, pp. 329–338. DOI: 10.1016/j.egypro.2016.09.191.

Thys, M, E Bachynski and F. H. Dadmarzi (2019a). *Model Test Report: Wave kinematics and loads*. Tech. rep. Trondheim: SINTEF Ocean.

— (2019b). *WAS-XL Model Test Report: Wave loads and response*. Tech. rep.

Veldkamp, H. F. and J. van der Tempel (Jan. 2005). 'Influence of wave modelling on the prediction of fatigue for offshore wind turbines'. In: *Wind Energy* 8.1, pp. 49–65. ISSN: 1095-4244. DOI: 10.1002/we.138.

Wang, Bin et al. (Sept. 2022). 'Numerical Investigation of Wave Run-Up and Load on Fixed Truncated Cylinder Subjected to Regular Waves Using OpenFOAM'. In: *Water (Switzerland)* 14.18. ISSN: 20734441. DOI: 10.3390/w14182830.

Wheeler, J D (1970). 'Method for Calculating Forces Produced by Irregular'. In: *Journal of Petroleum technology* 22, pp. 359–367. URL: http://onepetro.org/jpt/article-pdf/22/03/359/2228185/spe-2712-pa.pdf.

Wind Europe (2021). *Scaling up Floating Offshore Wind towards competitivenes*. Tech. rep.

Appendix

A   Validation results

Note that all figures have been presented in high-resolution format, enabling zooming in while minimizing quality reduction.

Additionally, the reason why the Rainey model is not included for the regular waves with a period of 6.5 [s] is that it does not meet the long wave approximation made within Rainey's theory.
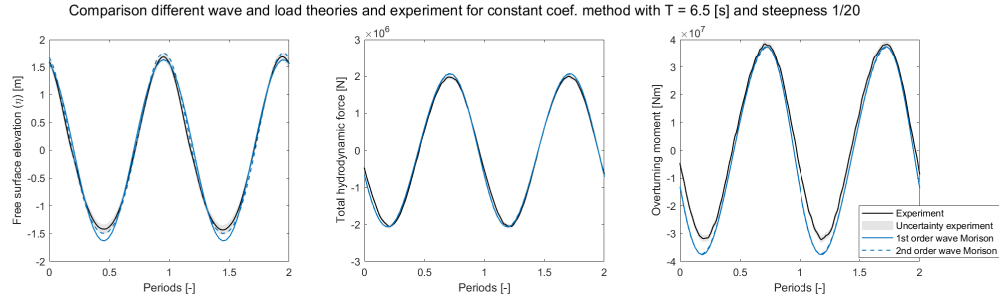

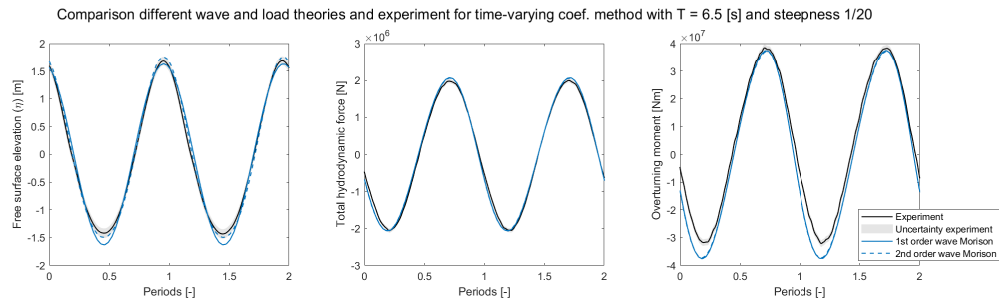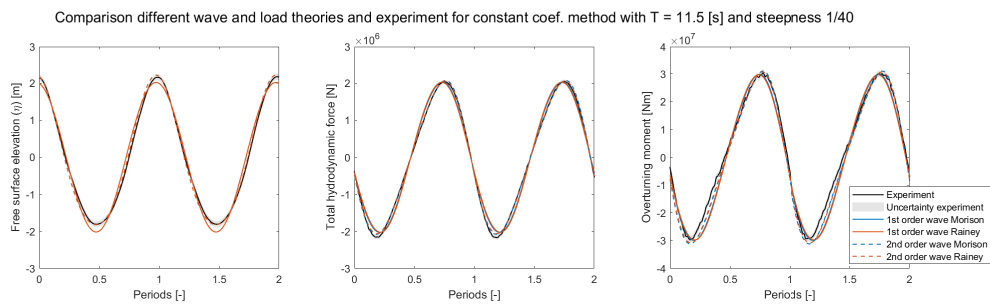Figure 47: Experimental data and constant coefficient model data for $T = 6.5$ [s] and steepness $= 1/20$

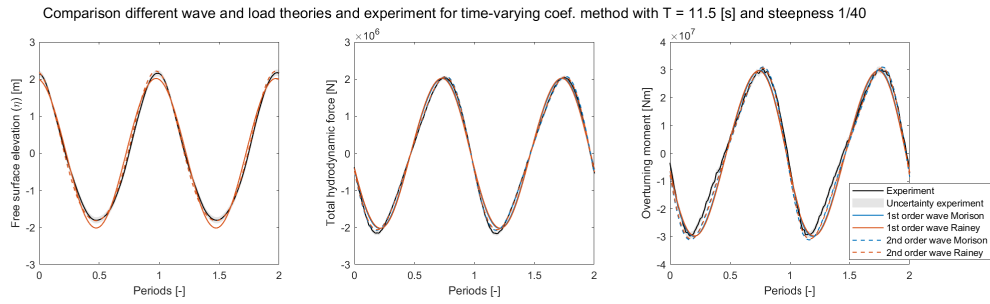

Figure 48: Experimental data and time-varying coefficient model data for $T = 6.5$ [s] and steepness $= 1/20$
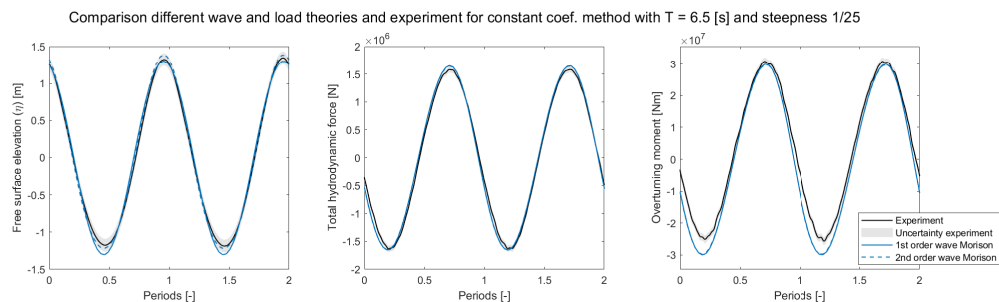
Figure 49: Experimental data and constant coefficient model data for $T = 6.5$ [s] and steepness $= 1/25$
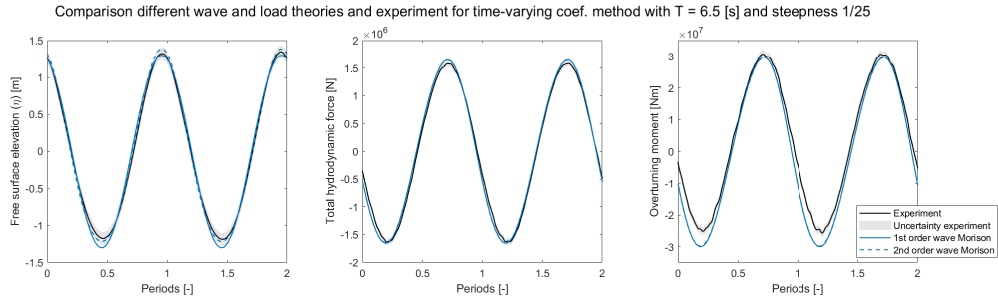
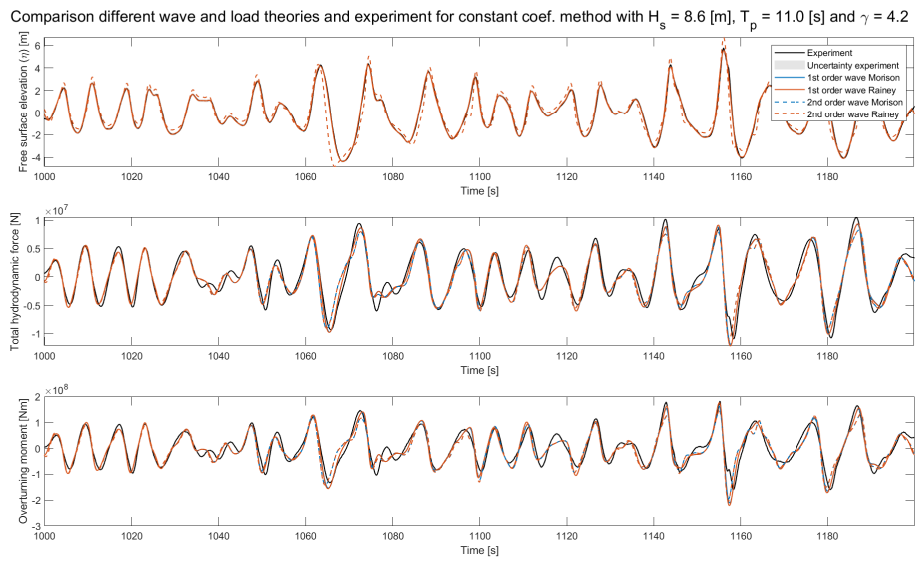Figure 50: Experimental data and time-varying coefficient model data for $T = 6.5$ [s] and steepness $= 1/25$
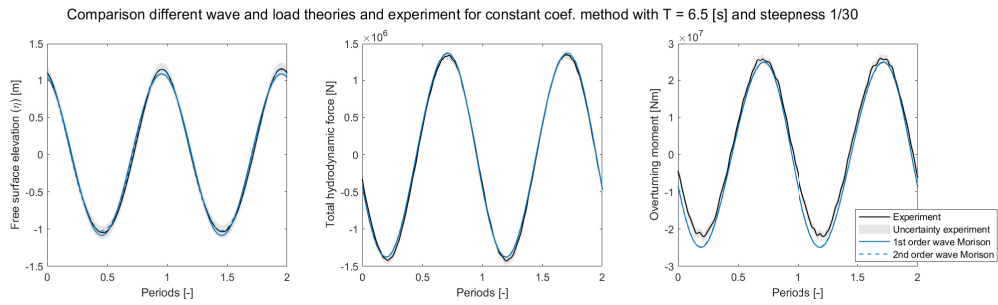
Figure 51: Experimental data and constant coefficient model data for $T = 6.5$ [s] and steepness $= 1/30$
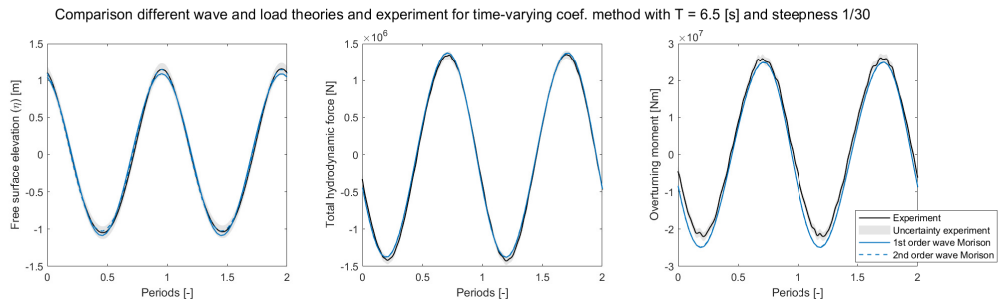
Figure 52: Experimental data and time-varying coefficient model data for $T = 6.5$ [s] and steepness $= 1/30$
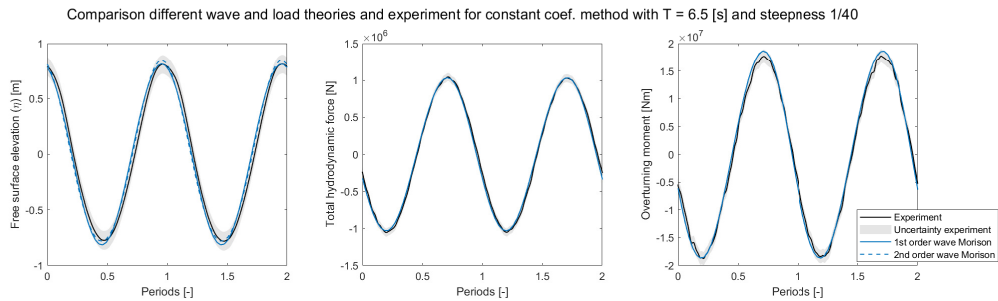
Figure 53: Experimental data and constant coefficient model data for $T = 6.5$ [s] and steepness $= 1/40$
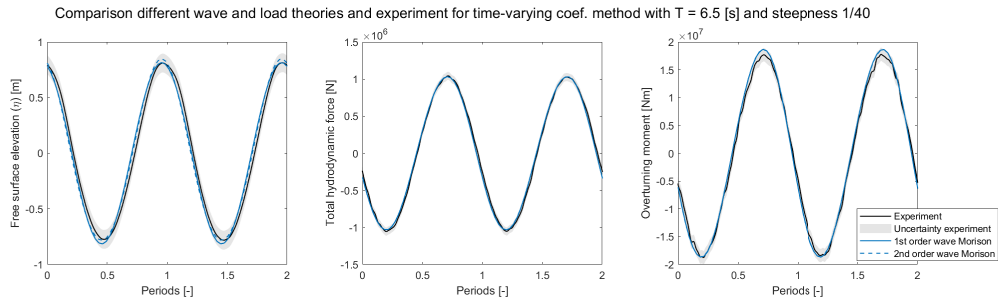
Figure 54: Experimental data and time-varying coefficient model data for $T = 6.5$ [s] and steepness $= 1/40$
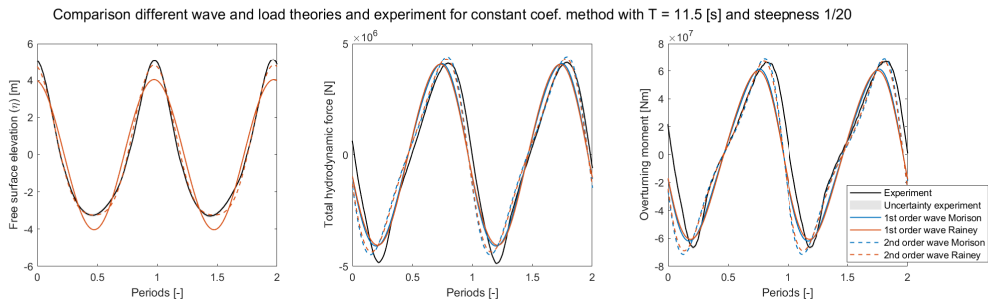
Figure 55: Experimental data and constant coefficient model data for $T = 11.5$ [s] and steepness $= 1/20$
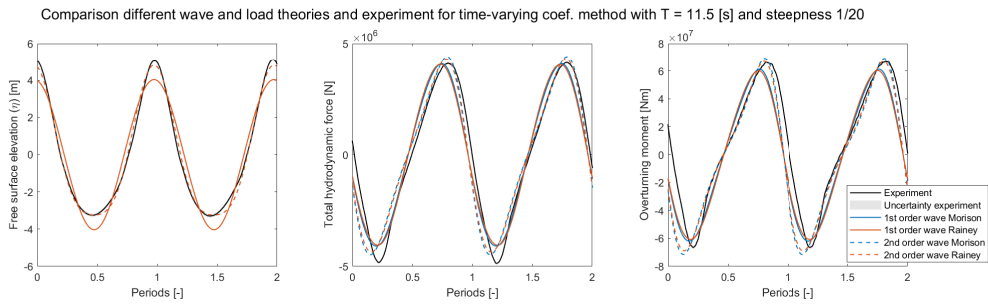
Figure 56: Experimental data and time-varying coefficient model data for $T = 11.5$ [s] and steepness $= 1/20$
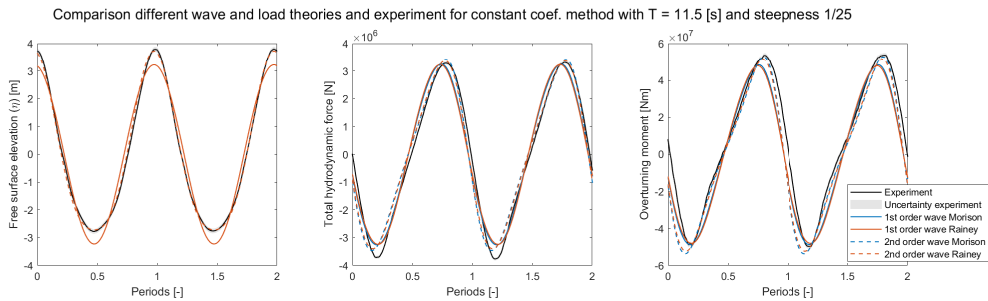
Figure 57: Experimental data and constant coefficient model data for $T = 11.5$ [s] and steepness $= 1/25$
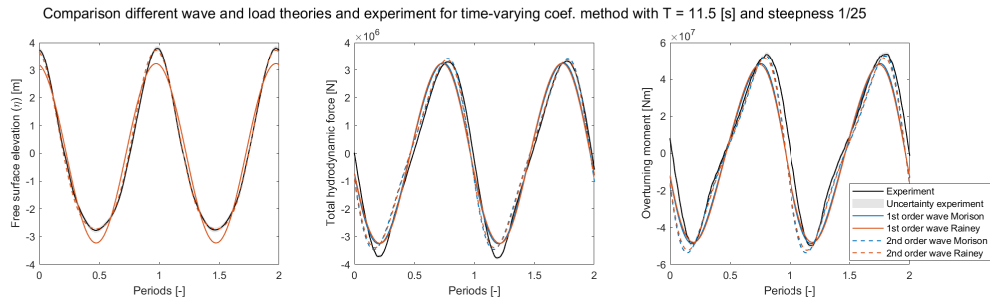
Figure 58: Experimental data and time-varying coefficient model data for $T = 11.5$ [s] and steepness $= 1/25$
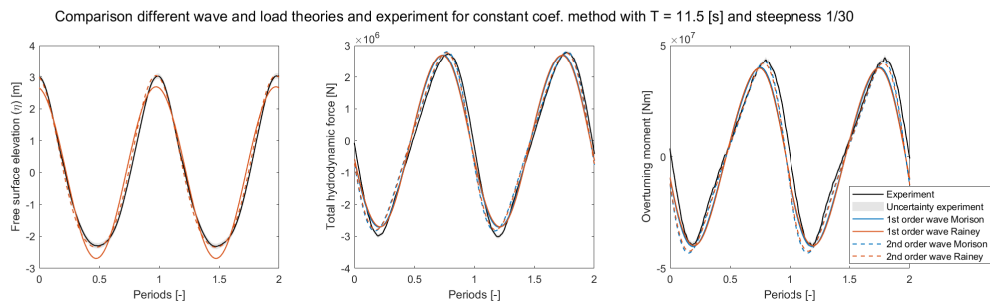
Figure 59: Experimental data and constant coefficient model data for $T = 11.5$ [s] and steepness $= 1/30$
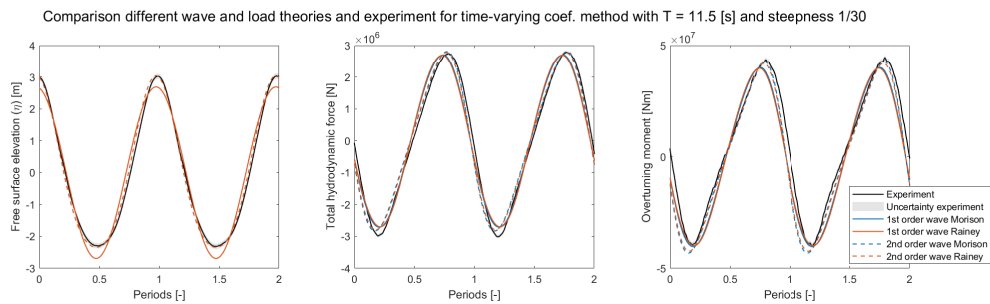
Figure 60: Experimental data and time-varying coefficient model data for $T = 11.5$ [s] and steepness $= 1/30$

Figure 61: Experimental data and constant coefficient model data for $T = 11.5$ [s] and steepness $= 1/40$

Figure 62: Experimental data and time-varying coefficient model data for $T = 11.5$ [s] and steepness $= 1/40$

Figure 63: Experimental data and constant coefficient model data for $H_s = 8.6$ [m], $T_p = 11.0$ [s] and $\gamma = 4.2$
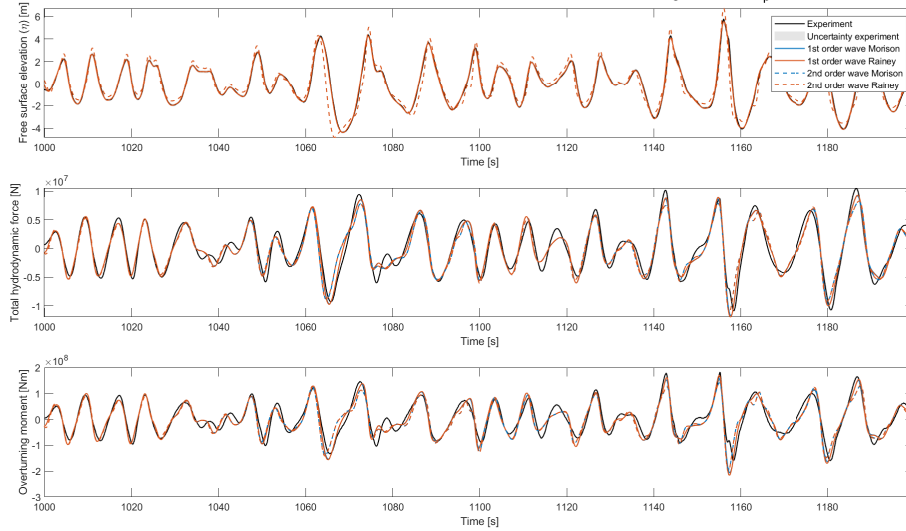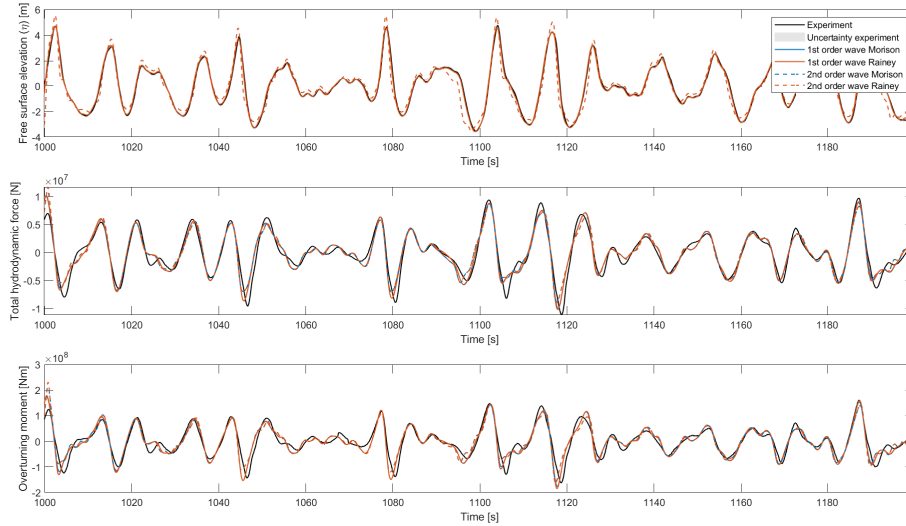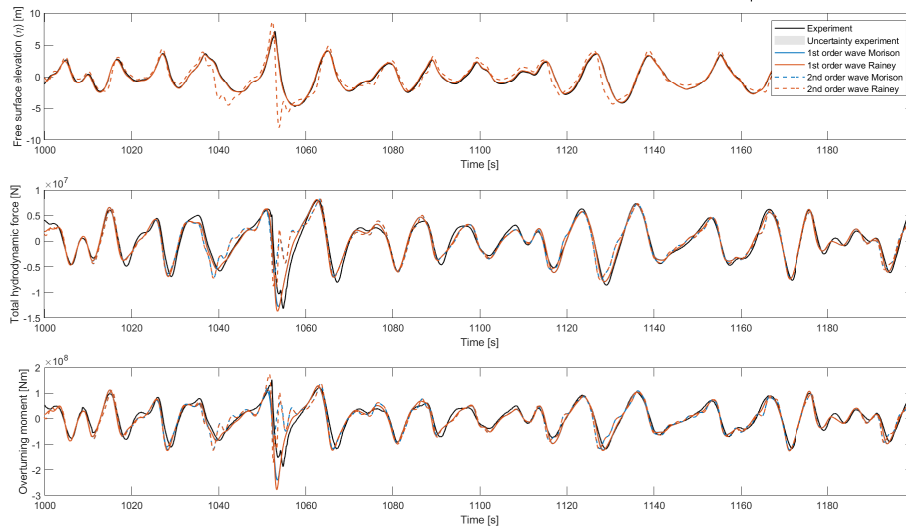
Figure 64: Experimental data and time-varying coefficient model data for $H_s = 8.6$ [m], $T_p = 11.0$ [s] and $\gamma = 4.2$
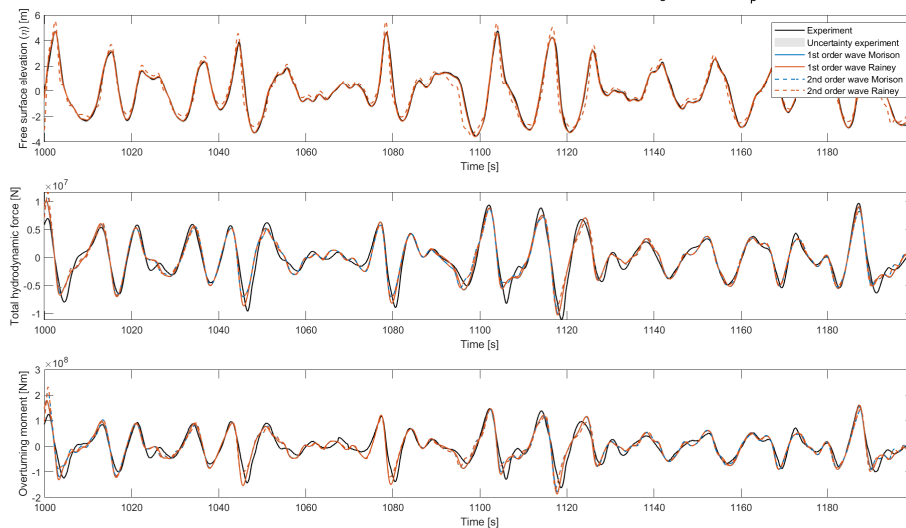
Figure 65: Experimental data and constant coefficient model data for $H_s = 9.0$ [m], $T_p = 12.5$ [s] and $\gamma = 2.6$

Figure 66: Experimental data and time-varying coefficient model data for $H_s = 9.0$ [m], $T_p = 12.5$ [s] and $\gamma = 2.6$

Figure 67: Experimental data and constant coefficient model data for $H_s = 6.8$ [m], $T_p = 13.2$ [s] and $\gamma = 1.0$
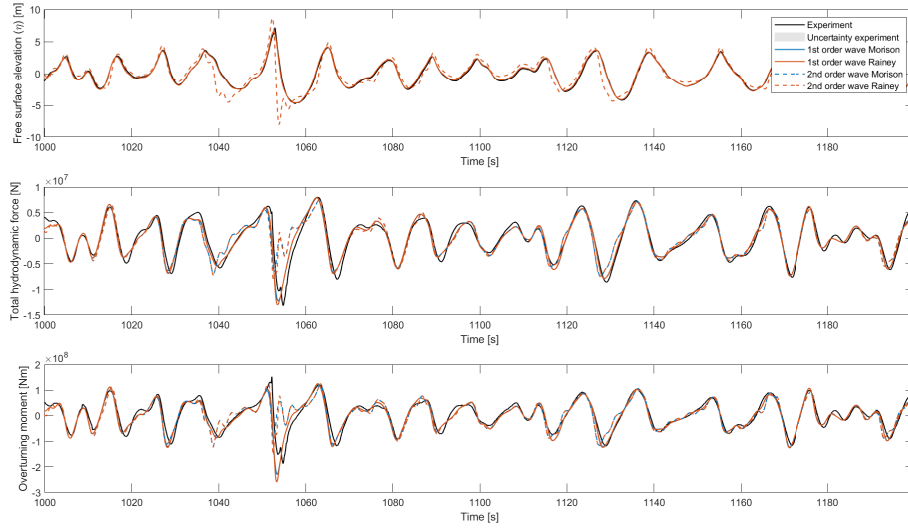
Figure 68: Experimental data and time-varying coefficient model data for $H_s = 6.8$ [m], $T_p = 13.2$ [s] and $\gamma = 1.0$
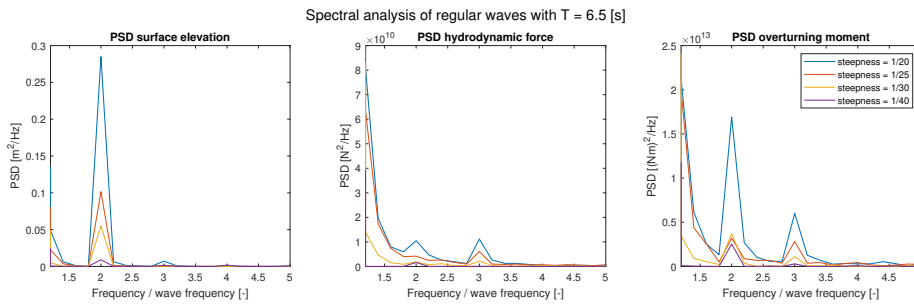

Figure 69: Spectral analysis experimental waves with $T = 6.5$ [s]

B Additional figures and tables for structural response calculation

Note that all figures have been presented in high-resolution format, enabling zooming in while minimizing quality reduction.

Load case	Test no.	H_s	T_p	γ
1	0004	1	6.1	1.00
2	0007	1	11.2	1.00
3	0010	1	16.3	1.00
4	0016	2	6.1	2.20
5	0019	2	11.2	1.00
6	0022	2	16.3	1.00
7	0028	3	6.1	5.00
8	0031	3	11.2	1.00
9	0034	3	16.3	1.00
10	0040	4	6.1	5.00
11	0043	4	11.2	1.00
12	0055	5	11.2	1.00
13	0067	6	11.2	1.64
14	0079	7	11.2	2.42
15	0091	8	11.2	3.31
16	0005	1	7.8	1.00
17	0008	1	12.9	1.00
18	0011	1	18	1.00
19	0017	2	7.8	1.00
20	0020	2	12.9	1.00
21	0023	2	18	1.00
22	0029	3	7.8	1.77
23	0032	3	12.9	1.00
24	0035	3	18	1.00
25	0041	4	7.8	3.54
26	0044	4	12.9	1.00
27	0053	5	7.8	5.00
28	0056	5	12.9	1.00
29	0068	6	12.9	1.00
30	0080	7	12.9	1.15
31	0092	8	12.9	1.66
32	0003	1	4.4	1.99
33	0006	1	9.5	1.00
34	0009	1	14.6	1.00
35	0012	1	19.7	1.00
36	0015	2	4.4	5.00
37	0018	2	9.5	1.00
38	0021	2	14.6	1.00
39	0024	2	19.7	1.00
40	0030	3	9.5	1.00
41	0033	3	14.6	1.00
42	0042	4	9.5	1.33
43	0045	4	14.6	1.00
44	0054	5	9.5	2.37
45	0057	5	14.6	1.00
46	0066	6	9.5	3.63
47	0069	6	14.6	1.00

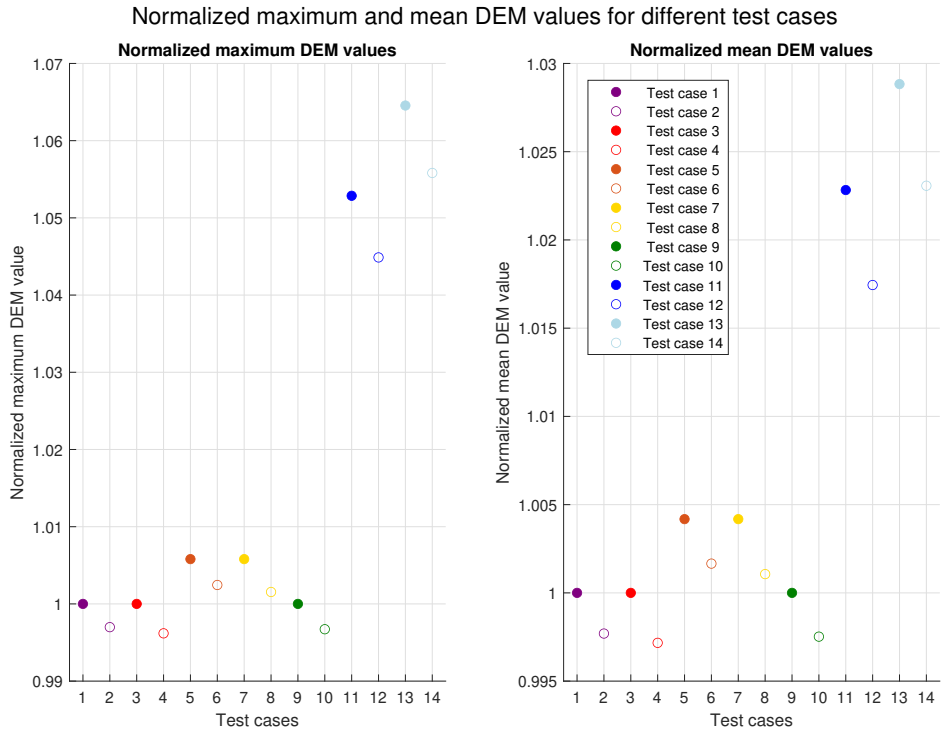Table 16: Description of all load cases used for fatigue assessment

Figure 70: Mean and maximum Damage Equivalent Moment (DEM) for all test cases with $m = 4$ normalized with test case 1
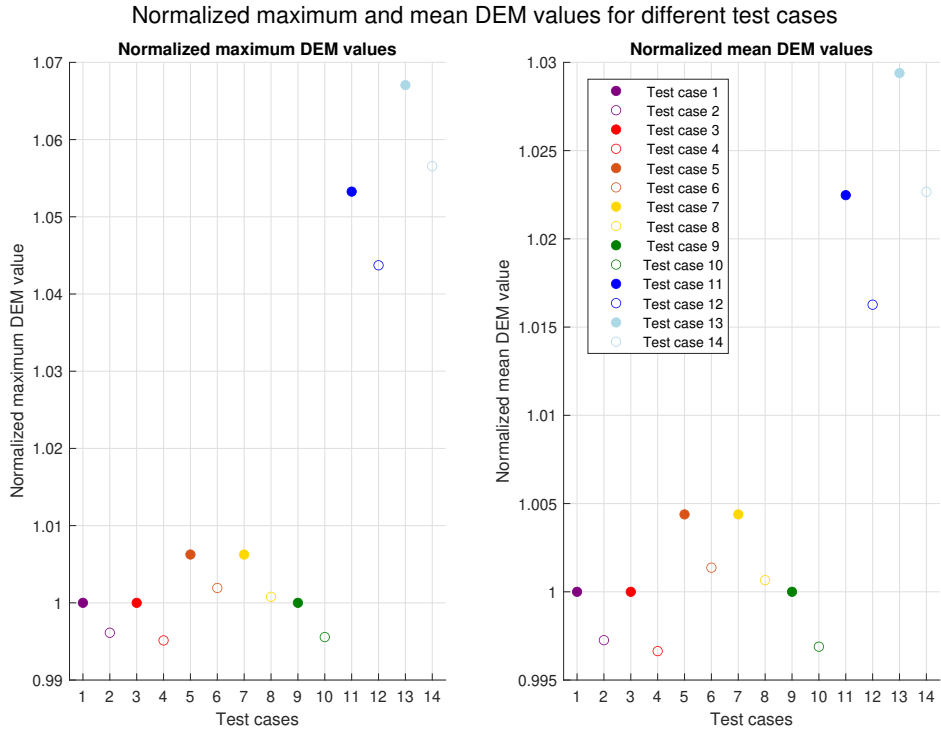

Figure 71: Mean and maximum Damage Equivalent Moment (DEM) for all test cases with $m = 5$ normalized with test case 1
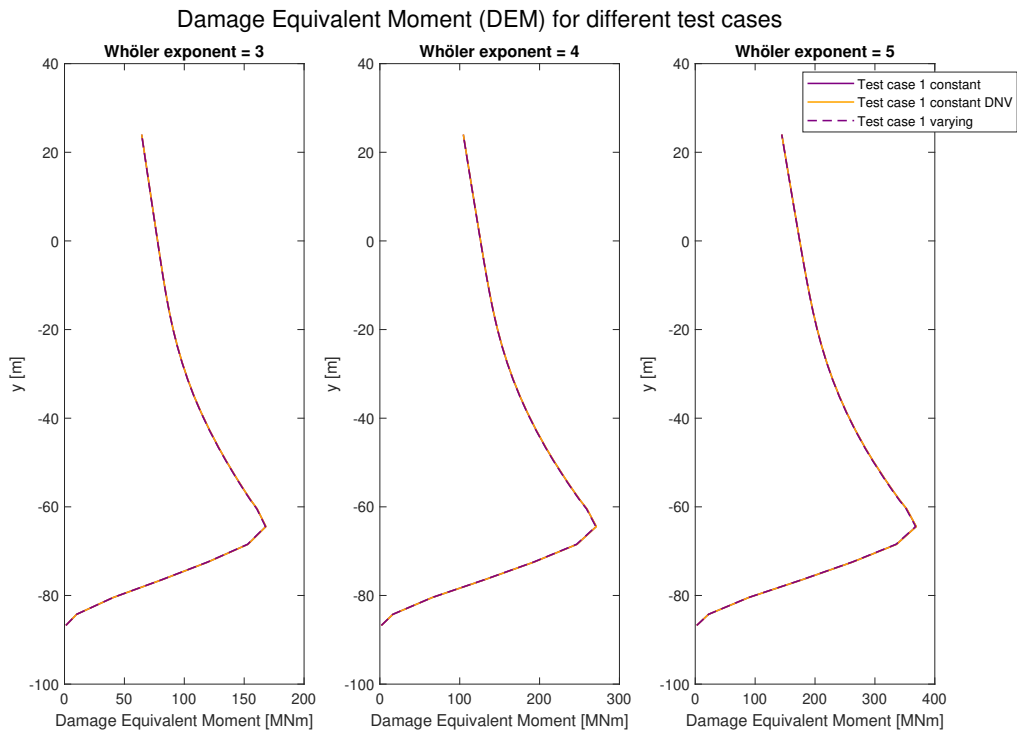
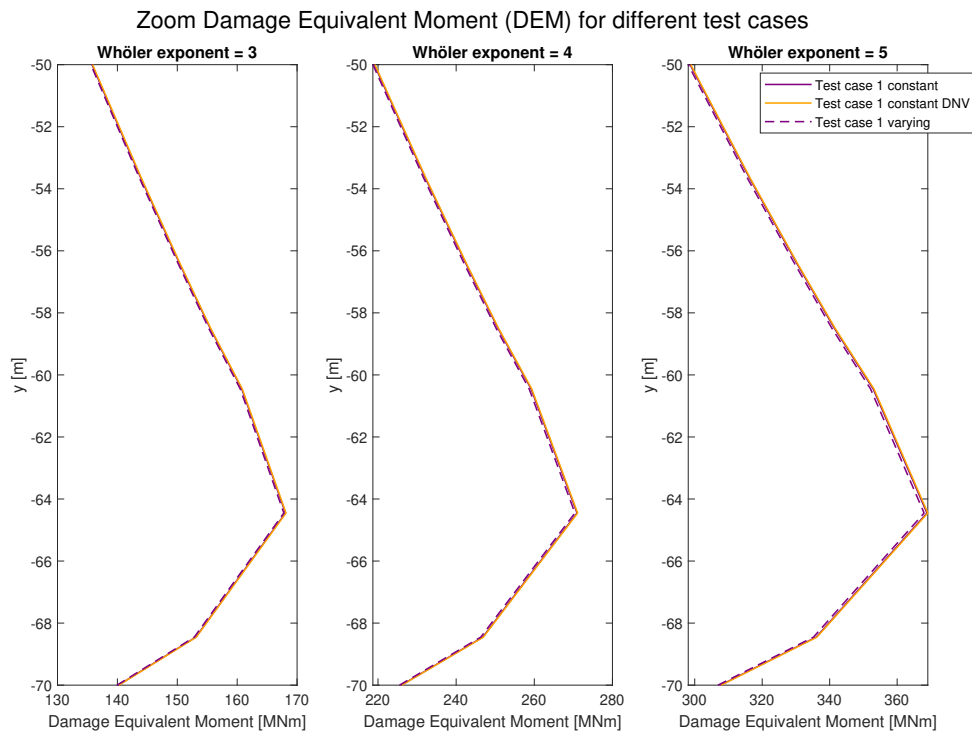Figure 72: Damage Equivalent Moment (DEM) along the depth for side study

Figure 73: Zoom Damage Equivalent Moment (DEM) along the depth for side study